

Title	Experimental and Theoretical Study on Density Oscillator
Author(s)	加納, 剛史
Citation	大阪大学, 2008, 博士論文
Version Type	VoR
URL	https://hdl.handle.net/11094/1916
rights	
Note	

Osaka University Knowledge Archive : OUKA

<https://ir.library.osaka-u.ac.jp/>

Osaka University

Ph.D. thesis

Experimental and Theoretical Study on Density Oscillator

(密度振動子の実験・理論的研究)

Takeshi Kano

Graduate School of Frontier Biosciences,
Osaka University

March 2008

論文内容の要旨

[題 名]

Experimental and Theoretical Study on Density Oscillator.

(密度振動子の実験・理論的研究)

自然界には、心筋細胞の収縮リズムや月経サイクルなど、自発的にリズムを刻む系が多く存在する。このような系は自励振動子と呼ばれ、系外からのエネルギーの供給によって系固有の特性を持った自発的な振動が維持されるという特徴を有する。このような自励振動子の中でも特に、遅い緩和過程と急激な移り変わりの過程の繰り返しによって振舞いが特徴づけられる振動子は、緩和振動子と呼ばれる。緩和振動子は、生体などさまざまな系において見られるだけでなく、電気回路などテクノロジーの分野への応用も広くなされており、その本質的かつ普遍的なメカニズムを理解することは、生物・医学・工学などの広い分野において極めて重要な意義を持つと考えられる。

過去に報告されている研究において、緩和振動の振舞いは現象論的に記述されてきたものの、振動に最も本質的であると考えられる急激な移り変わりの過程がどのようにして起こるかについては詳細に議論されておらず、従って緩和振動が起こるメカニズムは真の意味では明らかにされてこなかった。振動のメカニズムの解明のためには、急激な移り変わりの過程に注目し、ミクロな視点から振動の振舞いを明らかにすることが必要であると思われる。

密度振動子は、緩和振動のメカニズムを探るための優れた実験系である。密度振動子とは、底に管を取り付けた小さな容器を大きな容器に取り付け、小さな容器を重い流体で、大きな容器を軽い流体でそれぞれ満たすと、重い流体の大きな容器への流出と軽い流体の小さな容器への流入が周期的に繰り返される振動子である。その振舞いは、上向き・下向きの流れそれぞれについては過去の報告においてよく理解されてきたものの、流れの転換のメカニズムについては明らかにされてこなかった。本研究では、密度振動子の流れの転換過程を実験・理論の両面から探ることで、緩和振動の急激な移り変わりの過程に潜む普遍的なメカニズムを明らかにすることを目的とした。

実験では、水面の高さを測定すると同時に、管の内部を実体顕微鏡で観察した。その結果、流れの転換は、次のようにして起こることが明らかになった。例えば、下向きから上向きへの流れの転換過程の場合、まず軽い流体がわずかに侵入する。侵入した流体は非常にゆっくりとした速度で成長を続けるが、その侵入距離がある閾値に達すると急激に成長し始め、軽い流体が管の上端に達すると完全に流れが転換する。即ち、流れの転換過程は、流体の侵入とその急激な成長によって特徴づけられる。さらに、この侵入のタイミング及びその成長速度は流体の粘性率に大きく依存することが明らかになった。

このような実験結果を説明するために、流れの転換過程を取り込んだ密度振動のモデルを構築した。モデルは、侵入した流体の先端部の単位体積要素に粘性応力 (F_1)、静水圧勾配及び重力 (F_2)、そして管を通過した流体の加速による効果 (F_3) という3つの力がかかると考え、運動方程式を構築した。 F_1 、 F_2 、 F_3 はそれぞれ、侵入した流体を引き戻す働き (inhibiting factor)、侵入した流体を進ませる働き (promoting factor)、流体の管の中への侵入を誘起する働き (triggering factor) を持っている。このモデルをもとにシミュレーションを行ったところ、上記実験結果を概ね再現することができた。そして、その結果から、流体の侵入は F_3 によって引き起こされ、その急激な成長は F_2 の効果が F_1 の効果に打ち勝つことによって引き起こされる、ということが明らかになった。

このように、密度振動子の振舞いは、流れの転換過程における3つの要因 (inhibiting factor, promoting factor, triggering factor) を考えることによって、概ね理解することができる。この知見から、緩和振動子の急激な移り変わりの本質的なメカニズムは次のようであると考えることができる。まず、triggering factor によって、急激な移り変わりの前兆現象がゆっくりと進行する。そして promoting factor が inhibiting factor に打ち勝った時に急激な移り変わりが引き起こされると考えられる。

本研究によって明らかになったこの緩和振動のメカニズムは、複数の緩和振動子が相互作用する系（結合振動子系）の振舞いの解明や緩和振動の制御法の開発など、さまざまな応用研究に今後生かされると期待される。

Contents

1	Introduction	3
1.1	Self-oscillatory systems	3
1.2	Relaxation oscillation	6
1.3	Density oscillator	9
1.4	Unsolved problem	11
1.5	Aim of the research	12
2	Theoretical background	14
2.1	Analysis of up- and down-flow	14
2.2	Phenomenological model of density oscillator	19
2.3	Analysis of flow stability	20
3	Experiment	23
3.1	Experimental setup	23
3.1.1	Overview	23
3.1.2	Containers and a pipe	23
3.1.3	Fluids	24
3.1.4	Temperature control	24
3.1.5	Laser displacement meter	27
3.1.6	Stereomicroscope	28
3.2	Experimental procedure	30
4	Results and analyses	31
4.1	General trend	31
4.1.1	Height of a fluid surface	31
4.1.2	Flow-reversal process inside a pipe	34
4.2	Viscosity dependence	35
5	Modeling and simulation	44
5.1	Essential forces for flow reversal	44

5.1.1	Viscous drag force	44
5.1.2	Hydrostatic pressure gradient	48
5.1.3	Effect of acceleration of fluid outside a pipe	50
5.2	Description of flow-reversal process	51
5.2.1	Down- to up-flow	51
5.2.2	Up- to down-flow	52
5.2.3	Non-dimensionalized model	54
5.3	Simulations	57
6	Other factors related to oscillation	68
6.1	Pipe length	68
6.2	Pipe diameter	75
6.3	Density of fluid	82
6.4	Fluid materials	85
6.5	Summary	85
7	Discussion	87
7.1	Mechanism of density oscillation	87
7.1.1	Properties of forces	88
7.1.2	Future problems concerning the model	90
7.1.3	Extension to general cases	93
7.2	Mechanism of relaxation oscillation	94
7.3	Future prospect	97
	Appendix	100
A	Hagen-Poiseuille flow	101
B	Complementary explanation for phenomenological model	103
C	Model of coupled density oscillators	105

Chapter 1

Introduction

1.1 Self-oscillatory systems

Systems exhibiting regular rhythms spontaneously are abound in nature [1–14]. These systems are called self-oscillatory systems [1, 2, 15, 16], and have been extensively studied in various fields. One of the well known example is a heart which beats regularly even without will. This regular rhythm is known to be originated from the periodic activities of pacemaker cells in sinoatrial nodes [3]. Another example is menstrual cycle that occurs in the females of several mammals including human beings [4]. Physiologically, they are known to be caused by the rhythmic changes of secretions of hormones. On the other hand, a plasmodial slime mold, which is an amoeboid multinucleated unicellular organism, exhibits various oscillatory phenomena, such as oscillations in adenosine triphosphate and Ca^{2+} concentrations, thickness of the plasmodium, and protoplasmic streaming [5]. These are supposed to be generated by complicated mechanochemical reactions among chemicals, actin, and intracellular organelles, and so on. The self-oscillatory

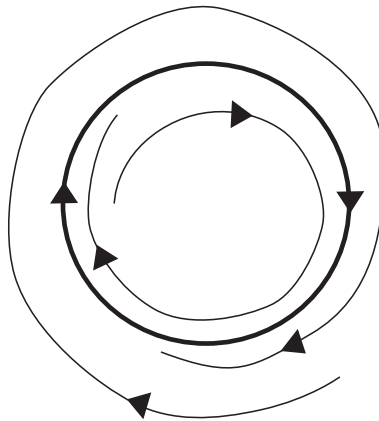


Figure 1.1: Scheme of limit cycle.

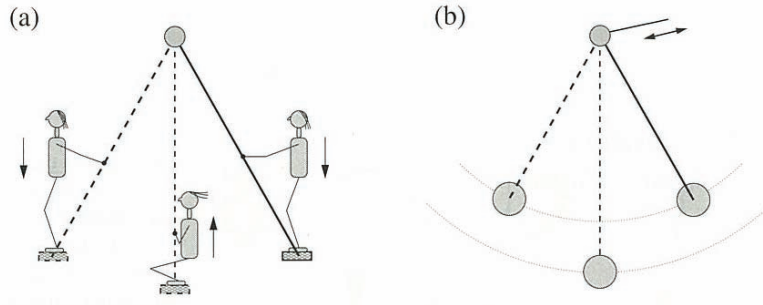


Figure 1.2: (a) A person on a swing exhibits self-oscillation. (b) Mechanical swing whose length changes according to a prescribed function of time, exhibits forced oscillation. Reproduced from Ref. [2] with permission.

systems are also found in non-living systems. For example, in Belousov-Zhavitinski reaction (BZ reaction), spontaneous rhythmic change of color of reactants is observed, which is caused by complicated processes of chemical reactions [6, 7]. Another example is the periodic cycle of El niño and La Niña phenomena, which is called El niño and southern oscillation (ENSO). It is thought to be caused by a periodic change of the air pressure and ocean current in the Pacific Ocean [8].

From physical and mathematical viewpoints, quite a few studies have been devoted to capture common characteristics of these self-oscillatory systems [1, 2, 15, 16]. In these studies, the self-oscillatory systems are considered as dynamical systems whose behaviors are predetermined by a set of rules (algorithm), and the oscillatory phenomena are described by simple differential equations with several degrees of freedom.

Such an approach began more than a century ago. Near the end of nineteenth century, Lord Rayleigh, who is famous for fluid dynamics and optics, devoted his studies also to oscillatory phenomena in acoustic systems [17]. In his famous treatise ‘The theory of sound’, he noted that vibrations of several acoustic systems are maintained in connection with constant energy source, and described their behaviors by a simple nonlinear equation. Although the significance of his discovery was not realized immediately, it was developed by the studies of van der Pol in 1920s [18–22]. He studied intensively on electric generators, and found that their behaviors were described by an equation similar to that Rayleigh derived. On the other hand, another development of mathematical study was achieved by Poincaré at the end of nineteenth century [15, 23]. He found that a dynamical system described by a couple of differential equations could exhibit a closed orbit in the phase plane, towards which neighboring paths were attracted (Fig. 1.1). He called this orbit as ‘(stable) limit cycle’.

About twenty years later than the discovery of van der Pol, a great contribution to

the oscillation theory was made by Andronov [15]. He noticed the inter-relation between Poincaré's limit cycles [23] and the periodic oscillations of the electronic generators studied by van der Pol [18–22]. As is the case in the van der Pol's electric generators, some autonomous systems were known to exhibit undamped oscillations with taking energy from nonperiodic sources.¹ He called this type of oscillation 'self-oscillation', and showed that the orbit of the self-oscillation was attracted to a stable limit cycle in the phase plane, which indicated that the dynamical behavior of the self-oscillatory system did not depend on the initial condition but on the property of the system itself. Later, the definition of the self-oscillation was slightly extended by Landa [1]. In the extended definition, self-oscillatory systems need not be autonomous. When an oscillation is maintained with taking energy from a source but the frequency spectrum of the oscillation is independent (or weakly dependent) of that of the energy source, it is generally called 'self-oscillation'.

Importantly, self-oscillation is discriminated from so called 'forced oscillation', in which the oscillation is maintained by a periodic external force and the period of the oscillator is in accordance with it. For clarity, let us consider the following example. Figure 1-2(a) shows the oscillation of swing [1, 2]. The oscillation of the swing is maintained if a person sits down when the swing approaches the left- and rightmost positions, and stands up when it passes the bottom of the swing. In this case, the source of energy here is muscular power of the person, because the movement of the center of gravity supplies energy to the swing. On the other hand, Fig. 1.2(b) shows the mechanical swing whose length is periodically changed by a mechanical force. In this case, the rhythm of the swing becomes in accordance with that of the mechanical force. Although these two systems seem to be similar, there is a crucial difference between them. In the former case, the movement of the person occurs in accordance with the position of the swing, i.e., autonomous, and the period is determined by the property of the swing itself. On the other hand, in the latter case, the change of the length is in accordance with some given periodic rhythm, i.e., non-autonomous, and the period is determined by that of the external force. Thus, we can conclude that the former is self-oscillation and the latter is forced oscillation.

Synchronization is one of the most important properties of self-oscillatory systems [2, 25]. Synchronization is a phenomenon that several oscillators adjust their own frequencies and behave cooperatively when the oscillators are coupled to each other or subjected to a periodical external field. Indeed, synchronization is a well known phenomenon in nature. For example, thousands of male fireflies living in southeast Asia emit light pulses synchronously in order to attract females [26]. In a concert hall, rhythmic applause of audience becomes sometimes synchronized [2]. Snowy tree crickets are able to synchronize

¹'autonomous system' means that the system is not driven by a force which explicitly depends on time.

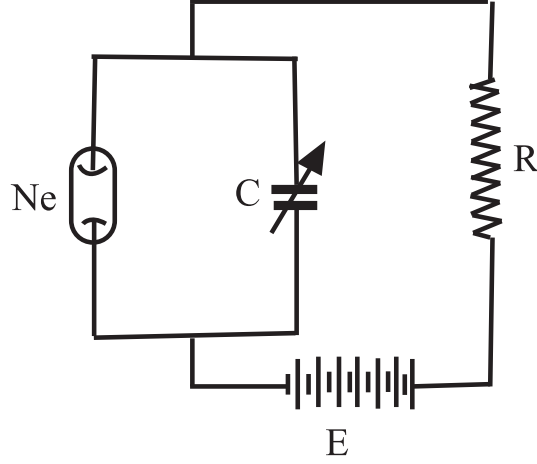


Figure 1.3: Electrical circuit that exhibits relaxation oscillation. It consists of a neon lamp Ne, a condenser C, a resistance R, and a battery E.

their chirps by responding to the preceding chirps of their neighbors [2]. Quite a few scientists have devoted their studies to such synchronization phenomena. Especially, the emergence of the cooperative behavior of coupled oscillators has been studied from analogy to the second order phase transition [25]. Recently, the coupled oscillator systems are not only studied to understand their principle but also engineered based on the obtained principle [27–30]. For example, the mechanism of coupled oscillators is used in the field of robotics [27].

1.2 Relaxation oscillation

Relaxation oscillation is a particular type of self-sustained oscillation, which was first proposed by van der Pol in 1926, before Andronov proposed a definition of self-oscillation [19]. He devoted his study to electronic generators [18–22], and described their behaviors by the following equation which is now famous for ‘van der Pol equation’:

$$\ddot{v} - \epsilon(1 - v^2)\dot{v} + v = 0. \quad (1.1)$$

While nearly sinusoidal solution is obtained when $\epsilon \ll 1$ is satisfied, he found that periodic solution is obtained even in the case of $\epsilon \gg 1$, where the system is highly nonlinear and dissipative. He pointed out that the latter condition is actually satisfied in the electrical system called ‘multivibrator’ that was introduced by Abraham and Bloch in 1919 [19].

Van der Pol noticed that the oscillatory behavior at $\epsilon \gg 1$ was found to be absolutely different from that at $\epsilon \ll 1$. Firstly, the waveform deviates considerably from a sinusoidal function and contains many higher harmonics. Indeed, in the case of $\epsilon \gg 1$, the

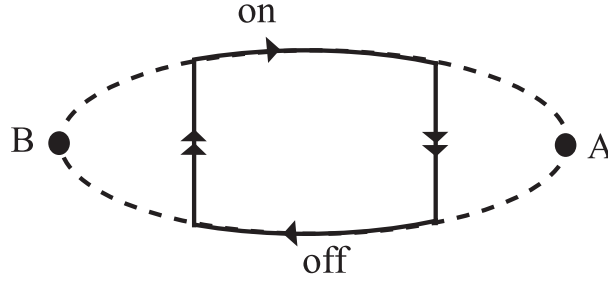


Figure 1.4: Scheme of relaxation oscillation. When a switch is ‘on’, the system approaches an equilibrium state A. However, before it reaches the equilibrium state, the switch is turned ‘off’, and the system approaches the other equilibrium state B. Before it reaches the equilibrium state, the switch is turned ‘on’ again in the similar manner.

value of v evolves in the following way: v increases slowly at first, and when v reaches a certain threshold, it jumps abruptly to a larger value. Then, v decreases slowly, and when v reaches another threshold, it jumps abruptly to a smaller value. In this way, the oscillation is characterized by the slow and fast processes. Secondly, the period of oscillation is characterized by a relaxation time of the system. Actually, from a simple analysis, the period of the multivibrator introduced by Abraham and Bloch is estimated to be the product of the capacitance and resistance, which corresponds to the relaxation time of the system. Van der Pol named the oscillation showing these characteristics as ‘relaxation oscillation’.

Later, he showed another example of electric circuit which exhibited relaxation oscillation (Fig. 1.3) [2, 20, 22]. It consists of a battery, a capacitor, a resistor, and a neon tube which conducts electric current only when the voltage reaches a certain critical level. First, the capacitor is being slowly charged. When the voltage reaches the threshold, the neon tube begins to conduct electric current. As a result, the capacitor quickly discharges with its voltage dropping and the neon tube becomes nonconductive again. Then, the process repeats again and again. Notice that also in this case, the period of the oscillation is characterized by the relaxation time of the charge of the capacitor, that is the product of the capacitance and resistance.

In general, relaxation oscillation is intuitively understood in the following way: Suppose that the dynamics of a system is determined by a certain ‘switch’ (Fig. 1.4). When the switch is ‘on’, the system approaches an equilibrium state. On the other hand, when the switch is ‘off’, the system approaches another one. Thus, if we turn on or off the switch, the state to which the system relaxes will change. Relaxation oscillator is considered as a system that the mechanism that controls the switch is inherent in the system itself. When the system relaxes to one of the equilibrium states to some extent, the switch is

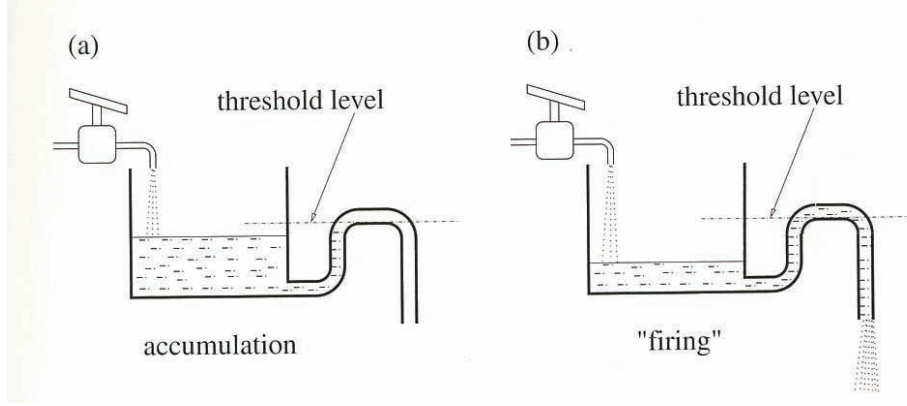


Figure 1.5: Mechanical model of a relaxation oscillator. (a) Water fills a vessel slowly until the surface of the water reaches the threshold level. (b) Water flows out through a trap so that its level in the vessel quickly goes down. Reproduced from Ref. [2] with permission.

turned automatically and the system relaxes to the other equilibrium state. Actually, the examples shown by van der Pol can be considered in this way. While the durations of ‘on’ and ‘off’ states are equivalent in the system described by Eq. (1.1), it is considered in the system of Fig. 1.3 that the duration of ‘on’ state (conductive at the neon tube) is extremely shorter than ‘off’ state (nonconductive at the neon tube).

Van der Pol predicted in his paper that the relaxation oscillation was a common phenomenon in nature [22]. For example, he considered that heart beat was a typical example of the relaxation oscillation, and reproduced its behavior by using the system of three coupled oscillators, each of which was composed of the electric circuit shown in Fig. 1.3 [22].

The relaxation oscillations are nowadays extremely well known and extensively studied in various fields [1–6, 8, 9, 11–14]. One of the examples is shown in Fig. 1.5 [2]. The main element of the system is a vessel being slowly filled with water. Then, when the water level reaches a threshold, the vessel empties quickly and a new cycle begins. Another example is found in endogenous circadian rhythms in plants performing crassulacean acid metabolism (CAM) [11]. In these plants, the transport of malate between the cytoplasm and vacuole is regulated by the property of the tonoplast of the vacuole. When the concentration of malate in the vacuole is low, the influx of malate occurs. At the critical concentration, the property of the tonoplast changes, and then the efflux of malate begins. At another critical concentration, the property of the tonoplast changes again, and thus the influx begins. In this way, oscillation will continue.

The relaxation oscillators are also applied to the technology. Particularly, those made by electric circuit [13] have been applied to produce square or sawtooth waves, the former of which is suitable for triggering synchronous logic circuits at precisely determined

intervals, while the latter is used for raster scan of televisions or monitors.

1.3 Density oscillator

Density oscillator is known as a typical example of relaxation oscillator [31–54]. It consists of an inner container with a thin pipe or a small orifice at the bottom, which is held within an outer container (Fig. 1.6). The inner container is filled with heavy fluid, while outer one is filled with light fluid. When the surfaces of both fluids are initially set at nearly the same height, the heavy fluid starts to flow downward through the pipe, owing to the gradient of hydrostatic pressure. At a critical height, the flow loses the stability and flow reversal occurs, which causes the light fluid to flow upward through the pipe. At another critical height, the flow loses the stability again, causing flow reversal and leading the heavy fluid to flow downward. In this way, the oscillation continues for more than several tens of cycles.

Density oscillator was first investigated in 1970 by Martin, a geophysist [31]. He found that a variety of straight tubes such as funnels and hypodermic syringes when filled with salt water and partially submerged in a beaker of fresh water exhibited oscillations of a finite amplitude. He named this phenomenon as ‘salt oscillation’. He not only performed the detail experiments using hypodermic syringes, but also analyzed each up- and down-flow according to Poiseuille’s law [55], and derived their dynamical behaviors theoretically at two limiting cases: viscous damping regime and non-linear damping regime. The experimental results were generally well explained by his analysis. However, he could not describe the oscillatory behavior because the mechanism of the flow reversal was not well understood.

The study of density oscillator was developed by Yoshikawa and his colleagues [32–34]. They founded the basis for the density oscillator as a relaxation oscillator, and formulated the oscillatory behavior by combining the equations for up- and down-flow derived by Martin. By using several approximations, they concluded that the oscillatory behavior was phenomenologically described by the same equation as that Rayleigh described in early days [17], now called ‘Rayleigh equation’. Recently, Okamura and Yoshikawa performed a simulation based on fundamental equations of fluid dynamics, and found that the oscillatory behavior was still described by Rayleigh equation even when Poiseuille’s law was not assumed [35]. Moreover, they found through the simulation that the potential energy of the fluid was the source of energy, which was dissipated by the effect of viscosity. This fact confirmed that the density oscillator had a typical characteristic of relaxation oscillator.

Synchronization of density oscillators has been also extensively studied [33, 36–39, 45].

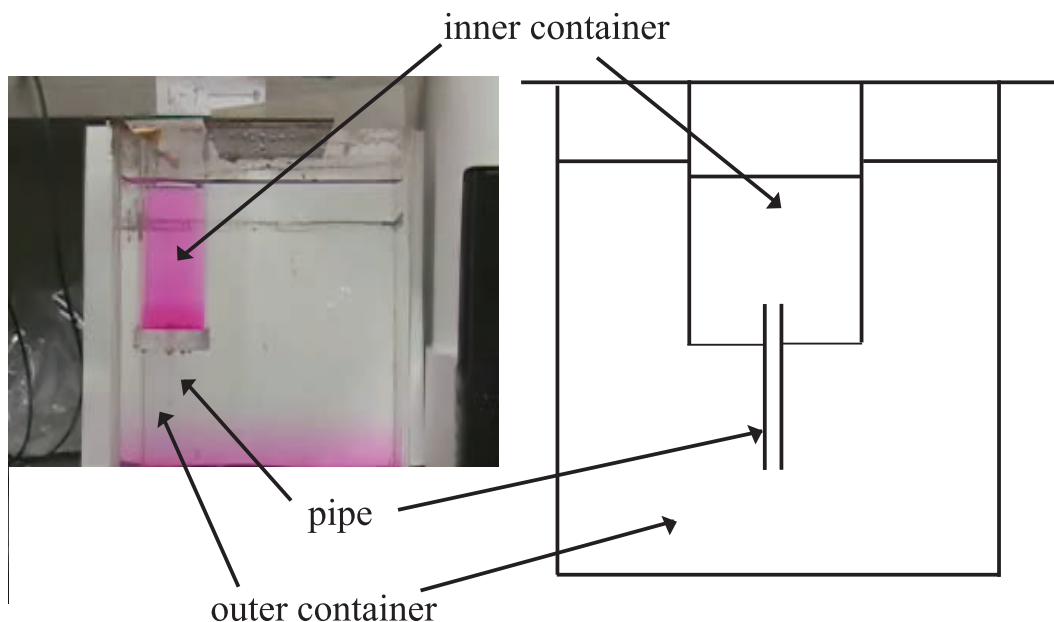


Figure 1.6: An example of density oscillator.

When several inner containers are held within one outer container, synchronization occurs due to mutual interaction of oscillators through the height of the fluid surface of the outer container (Fig. 1.7). Nakata *et al.* found that the ratio of the surface area of the outer container to that of the inner container characterized the coupling strength [36]. Miyakawa and Yamada reported a system consisting of two oscillators coupled with each other through the window of the partition wall, and found that in-phase synchronization occurred at certain parameter region, although only anti-phase synchronization occurred when the partition wall did not exist [38]. Yoshikawa and Fukunaga [33] investigated the coupling among three oscillators, and found that the oscillators were synchronized with their phases differed from each other equidistantly, which is now called ‘splay state’ [56, 57]. On the other hand, Miyakawa and Yamada [37] reported the coupling among more than three oscillators. They found that the oscillators were not fully synchronized for a large number of oscillators, while the splay or two-cluster state occurred when the number of the oscillators was not so large.

From an electrochemical viewpoint, the oscillation of electrical potential, which occurs when a couple of electrodes are placed in the light and heavy fluids, has been also extensively studied from an analogy to electrical phenomena associated with oscillation of biological membranes [34, 44, 46, 47, 50, 52]. The cause of the oscillation of electrical potential has long been in controversy. Noyes considered that it was caused by the change in junction potential generated at the interface between two fluids [44]. Yoshikawa *et al.* considered that not only junction potential but also streaming potential, which

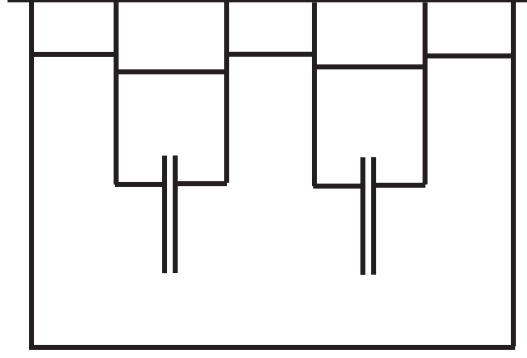


Figure 1.7: Scheme of coupled oscillators. Several inner containers are held within a large container.

generated when electrical double layer formed at the pipe and fluid was violated owing to the flow of the fluid, contributes to the oscillation [34]. Upadhyay *et al.* performed the detail experiments in order to confirm whether the junction potential or streaming potential was essential for the electrical oscillation, and concluded that the latter was essential [50]. Later, it was also suggested that the oscillation of streaming potential in density oscillator mimicked the sensing mechanism of taste [48]. On the other hand, Cervellati and Solda suggested that the oscillation of electrical potential could be applied to alternating voltage batteries [52]. Thus, research field of density oscillator has grown with various kinds of applicable possibility.

1.4 Unsolved problem

As described in Sec. 1.2, mathematical models of relaxation oscillations show the general behavior of the repetitive slow relaxation process and fast jumping process phenomenologically [18, 19, 21, 22]. However, when we look into more detailed mechanisms, we have noticed that such models do not correctly answer a fundamental question why relaxation oscillators oscillate. While harmonic oscillators oscillate due to their restoring forces, relaxation oscillators maintain their oscillations owing to the supply of energy from the sources at the jumping process, which corresponds to the process that the ‘switch’ is turned on or off [1, 15]. Thus, the following questions may naturally arise: “what mechanism causes the turn of the ‘switch’?” “How does the jumping process initiate?” Indeed, they must be the most essential questions for the mechanism of relaxation oscillation.

The density oscillator is an excellent system to investigate the essential mechanism of relaxation oscillation because of the simplicity of its experimental setup. In a density oscillator, the relaxation process corresponds to each up- and down-flow, while the

jumping process corresponds to the flow reversal. Hence, understanding how the flow-reversal process occurs is an absolutely important problem from the above context. As described in the previous section, the behavior of the density oscillator has been already described phenomenologically [32–34]. However, the essential cause of the flow reversal has not been fully discussed. Martin considered that the flow reversal occurred due to Rayleigh-Taylor instability [31], in which perturbation at a static interface between fluids grew, when a heavy fluid was located above a light fluid [58]. However, the dynamical process of the flow reversal cannot be understood in terms of Rayleigh-Taylor instability, because the spatiotemporal dynamics during flow reversal are extremely complex: In down- to up-flow, for instance, the flow reversal initiates from an intrusion of light fluid along the inner wall of the pipe. After some time, the intrusion begins to grow rapidly and climbs to the upper end of the pipe, and then the flow reverses completely (see Fig. 4.3) [31, 40, 41].

Steinbock *et al.* approached this problem from a hydrodynamic viewpoint [40]. They analyzed the stability of the down-flow inside the pipe, and derived the critical height for the instability of the flow. The critical height thus obtained was in good agreement with their experiment, when either the density of heavy fluid or the pipe length was varied. However, they did not take into account the effect of the flow after it passes through the pipe. In addition, the temporal evolution of the dynamical behavior during the flow-reversal process was not considered, since the steady-state approximation was employed in their analysis. Thus, the mechanism of the flow reversal is still not truly understood.

1.5 Aim of the research

In the present thesis, I aim to clarify the mechanism of the jumping process of relaxation oscillators by investigating the flow-reversal process in a density oscillator experimentally and theoretically. In the previous experimental studies on the density oscillator [31–54], the flow-reversal process has not been quantitatively evaluated because only the height of the heavy fluid surface or electric potential between the electrodes has been measured. In the present thesis, I will investigate the flow inside a pipe by using a stereomicroscope quantitatively, which is crucial for understanding the microscopic mechanism of the flow-reversal process.

From a hydrodynamic point of view, fluid dynamics in a system consisting of two viscous fluids has been an intriguing problem [59, 60]. Interestingly, the dynamics are known to be extremely sensitive to the viscosities of the fluids. One of the well-known examples is Saffman-Taylor instability, where an interface between two fluids tends to

become unstable when less viscous fluid is forced into more viscous fluid in a porous medium or a Hele-Shaw cell, while it remains stable in the opposite case [59]. Thus, it is strongly expected that even in a density oscillator, the dynamical behavior inside the connecting pipe will be largely affected by the viscosities of the fluids. Hence, I will investigate the essential mechanism of the flow reversal by focusing mainly on the viscosities of the fluids.

It is quite difficult to solve the flow-reversal process analytically. Actually, the analysis of flow that has passed through a pipe, has been one of difficult problems for hydrodynamicists. Hence, I aim to construct a simple model which not only describes the general aspect of oscillatory behaviors but also contains the essential mechanism of the flow-reversal process. Then, by considering the mechanism of the flow reversal based on the constructed model, I will discuss how the jumping process is initiated in relaxation oscillators.

The present thesis is organized as follows: In Chap. 2, we review the theoretical studies on density oscillator. Chap. 3 is devoted to experimental procedures and preliminary experiment on the flow-reversal process. In Chap. 4, the results obtained from quantitative measurements of the flow-reversal process with changing viscosity of fluids are shown. Chap. 5 is devoted to the modeling of the dynamics of density oscillation, taking essential mechanisms of the flow reversal into account. In Chap. 6, other factors which relate to the oscillatory behavior including the flow-reversal process, such as the geometry of a pipe, the density of the fluid, and the materials of the fluids are investigated. Finally, discussion and future prospects are described in Chap. 7.

Chapter 2

Theoretical background

In this chapter, I will review the theories proposed so far to explain the phenomenon of density oscillation.

2.1 Analysis of up- and down-flow

In this section, the analysis of each up- and down-flow studied by Martin [31] is described. Now consider the case where the pipe length d is much larger than the pipe radius a , and the flow inside a pipe is parallel to the axis of the pipe which is placed vertical to the ground. Cylindrical coordinate is used, where z axis is taken to coincide with the axis of the pipe and r denotes the radial coordinate. The origin of the z coordinate is set at the lower end of the pipe, and the upper direction is taken as positive. Then, z component of Navier-Stokes equation is given as follows:

$$\rho \frac{\partial u}{\partial t} = -\frac{\partial P(z)}{\partial z} - \rho g + \frac{\mu}{r} \frac{\partial}{\partial r} \left(r \frac{\partial u}{\partial r} \right), \quad (2.1)$$

where u is z component of the velocity of the flow, $P(z)$ is the hydrostatic pressure, and ρ and μ are the density and viscosity of the fluid, respectively. If a space inside a pipe is assumed to be completely occupied by the heavy or light fluid during the down- or up-flow, respectively, the following equation is obtained by integrating Eq. (2.1) over the space inside the pipe:

$$\rho_j \frac{\partial \bar{u}}{\partial t} = -\frac{P(d) - P(0)}{d} - \rho_j g + \frac{2\mu_j}{a} \frac{\partial u}{\partial r} \Big|_{r=a}, \quad (2.2)$$

where the suffix j is given as H or L, and ρ_H and ρ_L are the average densities of the fluids in the inner and outer containers, while μ_H and μ_L are their viscosities, respectively (see Fig. 2.1). Although ρ_H , ρ_L , μ_H and μ_L depend on the time due to inflow of the heavy fluid into the outer container and that of the light fluid into the inner container, only

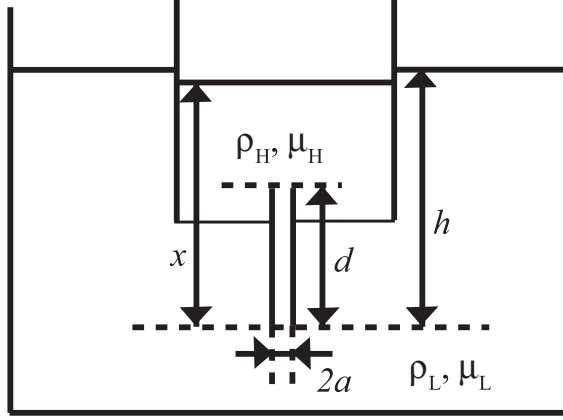


Figure 2.1: Definition of the parameters. a and d are the radius and length of a pipe, while x and h are the heights of the heavy and light fluid surfaces, respectively. ρ_H and ρ_L are the densities of the heavy and light fluids, while μ_H and μ_L are the viscosities of the heavy and light fluids, respectively.

ρ_H is assumed to be a function of time while the other three are constants, since the time dependence of the latter three are not essentially important. \bar{u} denotes the average velocity defined as

$$\bar{u} = \frac{2}{a^2} \int_0^a u(r, t) r dr. \quad (2.3)$$

Because the flow inside the pipe is almost regarded as Hagen-Poiseuille flow, which is known as the steady flow of a incompressible fluid through a straight pipe of circular cross section (see Appendix A), the following relation should hold (see Eq. (A.4)):

$$\left. \frac{\partial u}{\partial r} \right|_{r=a} = -\frac{4\bar{u}}{a}. \quad (2.4)$$

On the other hand, the hydrostatic pressure should satisfy

$$P(0) - P(d) = \rho_L g h - \rho_H(t) g (x - d) - \frac{3}{4} \rho_j \bar{u} |\bar{u}|, \quad (2.5)$$

where x and h are the heights of the heavy and light fluid surfaces, respectively. The first and second terms in the right hand side of Eq. (2.5) are the difference of hydrostatic pressure derived simply from the height of the fluid surface, while the third term denotes the loss of pressure at the passage of a pipe, which is called ‘head loss’. Here, x and h have the following relation,

$$h - h_{\text{de}}^{(i)} = -R(x - x_{\text{de}}^{(i)}), \quad (2.6)$$

where $R \equiv S/S_{\text{out}}$. Although it was assumed that the surface area of the outer container S_{out} was sufficiently larger than that of the inner container S in the theory derived by Martin [31], here his theory is extended to the case where this assumption is not necessary. Thus, in the limit of $R \rightarrow 0$, the above relation is equivalent to that in his theory. $x_{\text{de}}^{(i)}$ and $h_{\text{de}}^{(i)}$ are the heights of the heavy and light fluid surface at the hydrostatic

equilibrium where a pipe is filled with heavy fluid at i th cycle¹ (see Fig. 2.2). Here, the term ‘cycle’ is defined as a sequence of down- and up-flow. In addition, it is obvious from the condition of continuity as

$$\dot{x} = \frac{a^2\pi}{S}\bar{u}. \quad (2.7)$$

By substituting Eqs. (2.4)-(2.7) into Eq. (2.2), the following equations are obtained:

$$\frac{S}{a^2\pi}\ddot{x} + \frac{3S^2}{4da^4\pi^2}\dot{x}^2 + \frac{8\nu_L S}{a^4\pi}\dot{x} + \frac{g}{d}\left(\frac{\rho_H(t)}{\rho_L} + R\right)x = \frac{g}{d}\left(h_{\text{de}}^{(i)} + Rx_{\text{de}}^{(i)}\right) + \frac{\rho_H(t) - \rho_L}{\rho_L}g, \quad (2.8)$$

for up-flow and

$$\frac{S}{a^2\pi}\ddot{x} - \frac{3S^2}{4da^4\pi^2}\dot{x}^2 + \frac{8\nu_H(t)S}{a^4\pi}\dot{x} + \frac{\rho_L}{\rho_H(t)}\frac{g}{d}\left(\frac{\rho_H(t)}{\rho_L} + R\right)x = \frac{\rho_L}{\rho_H(t)}\frac{g}{d}\left(h_{\text{de}}^{(i)} + Rx_{\text{de}}^{(i)}\right), \quad (2.9)$$

for down-flow, where $\nu_H(t) \equiv \mu_H/\rho_H(t)$ and $\nu_L \equiv \mu_L/\rho_L$ are the kinematic viscosities of the heavy and light fluids, respectively.

Equations (2.8) and (2.9) can be further simplified through the following considerations. First, $\rho_H(t)$, which decreases as the number of cycles increases owing to inflow of the light fluid, is derived in the following way: Since $\rho_H(t)$ does not depend on the time during the down-flow, let $\rho_H(t)$ be defined as

$$\rho_H(t) = \rho_H^{(i)}, \quad (2.10)$$

for the i th down-flow. On the other hand, because the light fluid accumulates above the heavy fluid in the inner container during the up-flow, $\rho_H(t)$ should satisfy the following relation for the i th up-flow:

$$\rho_H(t)(x - d) = \rho_H^{(i)}(x_{\text{de}}^{(i)} - d) + \rho_L(x - x_{\text{de}}^{(i)}). \quad (2.11)$$

Second, from the balance of the hydrostatic pressure at the hydrostatic equilibrium where the pipe is filled with heavy fluid, the following relation should hold (see Fig. 2.2):

$$\rho_H^{(i)}x_{\text{de}}^{(i)} = \rho_L h_{\text{de}}^{(i)}. \quad (2.12)$$

Third, the non-dimensionalized variables \tilde{x} and \tilde{t} are introduced as follows:

$$\tilde{x} = \frac{x - x_{\text{de}}}{(\delta\rho^{(i)}/\rho_L)d}, \quad (2.13)$$

$$\tilde{t} = \frac{4\nu_L\beta}{a^2\sigma^{1/2}}t, \quad (2.14)$$

where $\beta^2 = ga^6\pi/(16S\nu_L^2d)$ and $\sigma = 3S\delta\rho^{(i)}/(2a^2\pi\rho_L)$ with $\delta\rho^{(i)} = \rho_H^{(i)} - \rho_L$.

Using Eqs. (2.10)-(2.14), Eqs. (2.8) and (2.9) are written in the non-dimensional form as follows:

$$\frac{d^2\tilde{x}^{(i)}}{d\tilde{t}^2} + \frac{2\sigma^{1/2}}{\beta}\left[\frac{d\tilde{x}^{(i)}}{d\tilde{t}} + \frac{\beta\sigma^{1/2}}{4}\left(\frac{d\tilde{x}^{(i)}}{d\tilde{t}}\right)^2\right] + \sigma[(1+R)\tilde{x} - 1] = 0, \quad (2.15)$$

¹In the present thesis, superscript (i) is omitted when it is not essentially important.

for up-flow and

$$\frac{d^2 \tilde{x}^{(i)}}{d\tilde{t}^2} + \frac{2\sigma^{1/2}}{\beta} \left[\frac{\nu_H^{(i)}}{\nu_L} \frac{d\tilde{x}^{(i)}}{d\tilde{t}} - \frac{\beta\sigma^{1/2}}{4} \left(\frac{d\tilde{x}^{(i)}}{d\tilde{t}} \right)^2 \right] + \sigma(1 + DR)\tilde{x} = 0, \quad (2.16)$$

for down-flow, where $D = \rho_L/\rho_H^{(i)}$ and $\nu_H^{(i)} = \mu_H/\rho_H^{(i)}$. Note that $\beta < 1$ and $\sigma > 3/2$ should be satisfied so that an oscillation occurs, which is found experimentally.

Thus, Eqs. (2.15) and (2.16) are the fundamental equations describing each up- and down-flow. As is expected, if we take the limit of $R \rightarrow 0$, these equations correspond to those derived by Martin (see Eqs. (18) and (17) in [31]). Here, it is found that Eqs. (2.15) and (2.16) finally asymptotes to $\tilde{x}^{(i)} = 1/(1 + R)$ and $\tilde{x}^{(i)} = 0$, which correspond to $x = x_{de}^{(i)} + \delta\rho^{(i)}d/[(1 + R)\rho_L]$ and $x = x_{de}^{(i)}$ in the dimensional form. Because these asymptotic values should correspond to the hydrostatic equilibrium where a pipe is filled with the light and heavy fluid at the i th cycle (Fig. 2.2), respectively, let $x_{ue}^{(i)}$ be defined as $x_{ue}^{(i)} \equiv x_{de}^{(i)} + \delta\rho^{(i)}d/[(1 + R)\rho_L]$.

Although Eqs. (2.15) and (2.16) are not solved analytically in general cases, they can be solved in the two limiting cases, 1) the case where the inertia and non-linear terms are neglected (viscous damping regime), and 2) the case where the viscous damping terms are neglected (nonlinear damping regime).

Viscous damping regime

When $\beta\sigma^{1/2} \ll 1$ is satisfied, it is expected that the contributions of the inertia and nonlinear terms in Eqs. (2.15) and (2.16) are extremely smaller than that of the viscous term. Thus, the inertia and nonlinear terms are thought to be neglected. Then, Eqs. (2.15) and (2.16) become

$$\frac{2\sigma^{1/2}}{\beta} \frac{d\tilde{x}^{(i)}}{d\tilde{t}} = -\sigma[(1 + R)\tilde{x} - 1], \quad (2.17)$$

$$\frac{2\sigma^{1/2}}{\beta} \frac{\nu_H^{(i)}}{\nu_L} \frac{d\tilde{x}^{(i)}}{d\tilde{t}} = -\sigma(1 + DR)\tilde{x}. \quad (2.18)$$

Equations (2.17) and (2.18) are easily solved, and the solutions are given in the dimensional forms as follows:

$$x = -C_u e^{-t/\tau_u} + x_{ue}^{(i)}, \quad (2.19)$$

for up-flow and

$$x = C_d e^{-t/\tau_d} + x_{de}^{(i)}, \quad (2.20)$$

for down-flow, where C_u and C_d are positive constants, and τ_u and τ_d are given as follows:

$$\tau_u = \frac{8Sd\mu_L}{(1 + R)ga^4\pi\rho_L}, \quad (2.21)$$

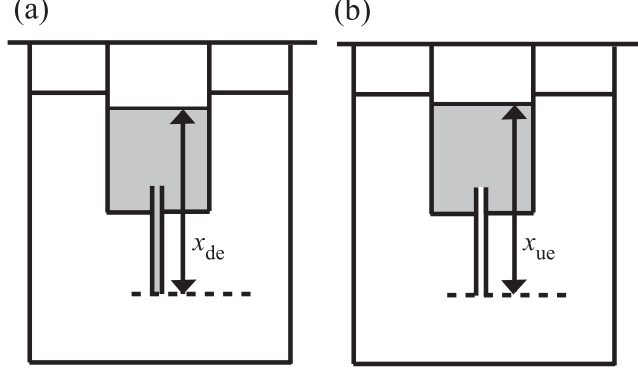


Figure 2.2: Two hydrostatic equilibria for a pipe filled with (a) heavy fluid and (b) light fluid. x_{de} and x_{ue} are defined as the heights of the heavy fluid surface at (a) and (b), respectively.

$$\tau_d = \frac{8Sd\mu_H}{(1 + DR)ga^4\pi\rho_H^{(i)}}. \quad (2.22)$$

Note that it is actually valid to neglect the inertia and nonlinear terms in Eqs. (2.15) and (2.16) in the case of $\beta\sigma^{1/2} \ll 1$ (which automatically satisfies $\beta \ll 1$ since $\sigma > 3/2$ should be satisfied), because it is found from Eqs. (2.17) and (2.18) that an order of each term in Eqs. (2.15) and (2.16) is estimated as $d^2\tilde{x}/d\tilde{t}^2 \sim (\beta^2\sigma/4)\tilde{x}$, $(2\sigma^{1/2}/\beta)(d\tilde{x}/d\tilde{t}) \sim \sigma\hat{x}$ and $(2\sigma^{1/2}/\beta)(\beta\sigma^{1/2}/4)(d\tilde{x}/d\tilde{t})^2 \sim (\beta^2\sigma^2/8)\tilde{x}$ under the assumptions of $D \sim 1$, $R \sim 1$ and $\nu_H/\nu_L \sim 1$, which confirms that the contribution of the viscous term is much larger than those of the inertia and nonlinear terms.

Nonlinear damping regime

In the case of $\beta\sigma^{1/2} \gg 1$, viscous terms, *i.e.*, the second terms in the left hand side of Eqs. (2.15) and (2.16), are thought to be neglected. Then, by defining $\Phi(\tilde{x}) = (d\tilde{x}/d\tilde{t})^2$, the following relations are derived:

$$\Phi'(\tilde{x}) + \sigma[\Phi(\tilde{x}) + 2(1 + R)\tilde{x} - 2] = 0, \quad (2.23)$$

for the up-flow, and

$$\Phi'(\tilde{x}) - \sigma[\Phi(\tilde{x}) - 2(1 + DR)\tilde{x}] = 0, \quad (2.24)$$

for the down-flow. Here, $\Phi'(\tilde{x})$ means the derivative of $\Phi(\tilde{x})$ with regard to \tilde{x} . Now consider the case of the down-flow, and suppose that $d\tilde{x}/d\tilde{t}=0$ and $\tilde{x} = 1$ at $\tilde{t} = 0$. Then, Eq. (2.24) is solved analytically as

$$\Phi(\tilde{x}) = \left(\frac{d\tilde{x}}{d\tilde{t}}\right)^2 = 2(1 + DR) \left(\frac{1}{\sigma} + \tilde{x}\right) - 2(1 + DR) \left(\frac{1}{\sigma} + 1\right) e^{-\sigma(1-\tilde{x})}. \quad (2.25)$$

Here, since $\beta < 1$ should be satisfied so that an oscillation occurs, $\sigma \gg 1$ should be satisfied. Thus, Eq. (2.25) is approximated as

$$\Phi(\tilde{x}) = \left(\frac{d\tilde{x}}{d\tilde{t}} \right)^2 \approx 2(1 + DR)\tilde{x}. \quad (2.26)$$

From Eq. (2.26), the duration of the down-flow in the dimensional form t_d is roughly estimated as

$$\begin{aligned} t_d &\sim \left(\frac{4\nu_L\beta}{a^2\sigma^{1/2}} \right)^{-1} \int_0^1 \frac{\partial\tilde{x}}{\sqrt{(d\tilde{x}/d\tilde{t})^2}} \\ &= \sqrt{3} \frac{S}{a^2\pi} \left(\frac{d\delta\rho^{(i)}}{g\rho_L(1 + DR)} \right)^{1/2}. \end{aligned} \quad (2.27)$$

The duration of the up-flow can be derived from Eq. (2.23) in the same way.

It is confirmed that it is actually valid to neglect the viscous term in Eq. (2.16) in the case of $\beta\sigma^{1/2} \gg 1$ from the following consideration: From Eq. (2.26), it is found that $(d\tilde{x}/d\tilde{t}) \sim 1$ if $D \sim 1$ and $R \sim 1$ are satisfied. Hence, the contribution of the nonlinear and viscous terms in Eq. (2.16) can be simply estimated from the coefficient of each term. Thus, in the present case, the contribution of the nonlinear term is much larger than that of the viscous term. In the same manner, it is also confirmed that the viscous term in Eq. (2.15) can be actually neglected.

2.2 Phenomenological model of density oscillator

In the previous section, the dynamical behaviors of up- and down-flow are theoretically described. However, the oscillatory behavior cannot be described by the theory, because the flow reversal, *i.e.*, switching between Eqs. (2.15) and (2.16), is not considered. In this section, a phenomenological model for the whole oscillatory behavior derived by Yoshikawa *et al.* [32–34] is described.

Now consider the case of $D \approx 1$ and $\nu_H = \nu_L \equiv \tilde{\nu}$, and assume that $\rho_H^{(i)}$ and $\tilde{x}^{(i)}$ do not depend on the number of cycles i . Then, both Eqs. (2.15) and (2.16) are combined into one equation as follows:

$$\frac{d^2\tilde{x}'}{d\tilde{t}^2} = -A_1 \left(\frac{d\tilde{x}'}{d\tilde{t}} \right) \left| \frac{d\tilde{x}'}{d\tilde{t}} \right| - A_2 \left(\frac{d\tilde{x}'}{d\tilde{t}} \right) - A_3(1 + R)\tilde{x}' + \frac{A_3}{2} \text{sgn} \left(\frac{d\tilde{x}'}{d\tilde{t}} \right), \quad (2.28)$$

where $\tilde{x}' = \tilde{x} - 1/[2(1 + R)]$, $A_1 = \sigma/2$, $A_2 = 2\sigma^{1/2}/\beta$, and $A_3 = \sigma$. Because $d\tilde{x}'/d\tilde{t}$, $(d\tilde{x}'/d\tilde{t})|d\tilde{x}'/d\tilde{t}|$, and $\text{sgn}(d\tilde{x}'/d\tilde{t})$ are odd function of $d\tilde{x}'/d\tilde{t}$, the right hand side of Eq. (2.28) is approximated to the third order of $d\tilde{x}'/d\tilde{t}$ to describe the oscillatory behavior in the following way:

$$\frac{d^2\tilde{x}'}{d\tilde{t}^2} = B_1 \left(\frac{d\tilde{x}'}{d\tilde{t}} \right) - B_2 \left(\frac{d\tilde{x}'}{d\tilde{t}} \right)^3 - A'_3\tilde{x}', \quad (2.29)$$

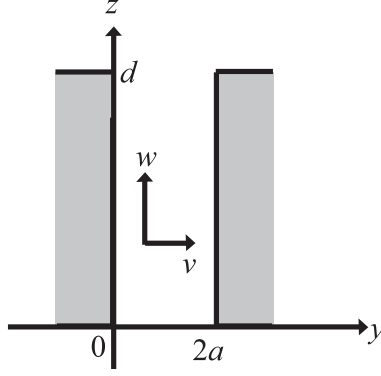


Figure 2.3: Two-dimensional geometry for a rectangular pipe. y and z components of the velocity of the flow are denoted as v and w , respectively.

where B_1 and B_2 are positive constants, and $A'_3 = A_3(1+R)$. Equation (2.29) is known as Rayleigh equation, which Rayleigh described for the vibrations in acoustic systems [17].

In this way, Eq. (2.29) has become one of the most common qualitative descriptions of density oscillation. Indeed, Eq. (2.29) well describes the behavior of relaxation oscillation, although the oscillatory behavior is not introduced in Eq. (2.28) (details are shown in Appendix B). Moreover, behaviors of coupled oscillators can be also described by adding a coupling term to Eq. (2.29) (see Appendix C). However, the present model has a crucial problem that the flow-reversal process is not correctly described owing to the approximation made to derive Eq. (2.29) from Eq. (2.28).

2.3 Analysis of flow stability

In the above theories, the flow-reversal process is not described explicitly either from a phenomenological or microscopic standpoint. On the contrary, Steinbock *et al.* focused on the flow-reversal process [40]. In the following, their stability analysis of the down-flow inside a pipe will be shown. Although it was assumed that the surface area of the outer container S_{out} was sufficiently larger than that of the inner container S in their analysis, here their theory is extended to the case where this assumption is not necessary.

Now consider a pipe with a two-dimensional rectangular cross section, and let y and z denote the horizontal and vertical coordinates, respectively (see Fig. 2.3). The pipe length d is assumed to be much larger than the diameter $2a$. One-fluid model is applied where the density of the fluid is described as $\rho = \rho_H - \delta\rho\Theta$, with Θ the function of space and time. The aim of the analysis is to find the condition that the down-flow loses stability when an intrusion of light fluid exists steadily at $y = z = 0$. Using the steady state approximation and Boussinesq approximation, Navier-Stokes equation is described

as

$$w\partial_z w + v\partial_y w = -g + \frac{\delta\rho g}{\rho_H}\Theta - \frac{1}{\rho_H}\partial_z P + \nu_H(\partial_z^2 w + \partial_y^2 w), \quad (2.30)$$

$$w\partial_z v + v\partial_y v = -\frac{1}{\rho_H}\partial_y P + \nu_H(\partial_z^2 v + \partial_y^2 v), \quad (2.31)$$

where P is the hydrostatic pressure, and v and w are the y and z components of the velocity of flow, respectively. ∂_z and ∂_y are abbreviations of $\partial/\partial z$ and $\partial/\partial y$, respectively. The condition of continuity is given as

$$\partial_z w + \partial_y v = 0. \quad (2.32)$$

On the other hand, diffusion equation is given as

$$w\partial_z \Theta + v\partial_y \Theta = D_f(\partial_z^2 \Theta + \partial_y^2 \Theta), \quad (2.33)$$

where D_f is a diffusion constant. Equations (2.31)-(2.33) are written in the non-dimensionalized forms as follows:

$$R_e \epsilon' (\bar{w}\partial_{\bar{z}}\bar{w} + \bar{v}\partial_{\bar{y}}\bar{w}) = \lambda\Theta - \kappa - \partial_{\bar{z}}\bar{P} + \epsilon'^2 \partial_{\bar{z}}^2 \bar{w} + \partial_{\bar{y}}^2 \bar{w}, \quad (2.34)$$

$$R_e \epsilon'^3 (\bar{w}\partial_{\bar{z}}\bar{v} + \bar{v}\partial_{\bar{y}}\bar{v}) = -\partial_{\bar{y}}\bar{P} + \epsilon'^4 \partial_{\bar{z}}^2 \bar{v} + \epsilon'^2 \partial_{\bar{y}}^2 \bar{v}, \quad (2.35)$$

$$\partial_{\bar{z}}\bar{u} + \partial_{\bar{y}}\bar{v} = 0, \quad (2.36)$$

$$\epsilon' (\bar{w}\partial_{\bar{z}}\Theta + \bar{v}\partial_{\bar{y}}\Theta) = -\frac{D_f}{Q}(\epsilon'^2 \partial_{\bar{z}}^2 \Theta + \partial_{\bar{y}}^2 \Theta). \quad (2.37)$$

where $\bar{z} = d/z$, $\bar{y} = y/2a$, $\bar{w} = 2wa/Q$, $\bar{v} = vd/Q$, $\bar{P} = 8Pa^3/(\rho_H d \nu_H Q)$, $R_e = Q/\nu_H$, $\kappa = 8a^3g/(\nu_H Q)$, $\lambda = 8ga^3\delta\rho/(\nu_H Q \rho_H)$, and $\epsilon' = 2a/d \ll 1$. Q is the flow rate through a pipe. Because the flow inside the pipe is nearly regarded as two-dimensional Poiseuille flow (see Appendix A) [55], Q is derived as

$$\begin{aligned} Q &= \int_0^{2a} w dy \\ &= -\frac{2a^3}{3\mu_H} \left(\frac{\rho_H g(x-d) - \rho_L g h}{d} + \rho_H g \right). \end{aligned} \quad (2.38)$$

Let a stream function $\Psi(\bar{y}, \bar{z})$ be defined so that $\bar{w} = \partial_{\bar{y}}\Psi(\bar{y}, \bar{z})$ and $\bar{v} = -\partial_{\bar{z}}\Psi(\bar{y}, \bar{z})$ are satisfied. Note that Eq. (2.36) is automatically fulfilled by defining the stream function. The boundary conditions are given with using Ψ as $\partial_{\bar{y}}\Psi = 0$ (no slip) and $-\partial_{\bar{z}}\Psi = 0$ (no penetration of the vertical walls) at $\bar{y} = 0$ and 1. If $\Psi = 0$ at $\bar{y} = 0$ is assumed, $\Psi|_{\bar{y}=1} = \int_0^1 d\bar{y}\bar{w} = \int_0^{2a} dyw/Q = 1$ should be satisfied. In addition, since the heavy fluid flows downward while an intrusion of the light fluid exists steadily at $y = z = 0$, the boundary condition of Θ is given as $\Theta = 1$ at $\bar{z} = \bar{y} = 0$ and $\Theta = 0$ at $\bar{y} = 1$. Using these conditions, Eqs. (2.34), (2.35), and (2.37) are solved at the zeroth order of ϵ' as follows:

$$\Theta_0(\bar{y}, \bar{z}) = \theta_0(\bar{z})(1 - \bar{y}), \quad (2.39)$$

$$\Psi_0(\bar{y}, \bar{z}) = 3\bar{y}^2 - 2\bar{y}^3 + \frac{\lambda}{24}\theta_0(\bar{z})(1 - \bar{y}^2)\bar{y}^2, \quad (2.40)$$

where $\theta_0(0) = 1$ should be satisfied.

Then, the condition that the down-flow loses its stability is given by $\partial_{\bar{y}}\bar{w}|_{\bar{y}=\bar{z}=0} = \partial_y^2\Psi|_{\bar{y}=\bar{z}=0} > 0$. This condition is derived from Eq. (2.40) as $\lambda > -72$. Then, using Eqs. (2.6) and (2.38), this condition is found to be equivalent to

$$x - x_{\text{de}}^{(i)} < \frac{1}{6} \frac{\delta\rho^{(i)}d}{\rho_{\text{H}}^{(i)} + \rho_{\text{L}}R}. \quad (2.41)$$

Notice that when we take the limit of $R \rightarrow 0$, Eq. (2.41) corresponds to the equation derived by Steinbock *et al.* (see Eq. (12) in [40]).

Complementary explanation

Let us consider the physical meaning of the result by the analysis of Steinbock *et al.*, Eq. (2.41). From Eq. (2.12), $\rho_{\text{H}}^{(i)}x_{\text{de}}^{(i)} = \rho_{\text{L}}h_{\text{de}}^{(i)}$ should be satisfied. In the same way, $\rho_{\text{H}}^{(i)}(x_{\text{ue}}^{(i-1)} - d) = \rho_{\text{L}}(h_{\text{ue}}^{(i-1)} - d)$ with $h_{\text{ue}}^{(i)} \equiv h_{\text{de}}^{(i)} - R(x_{\text{ue}}^{(i)} - x_{\text{de}}^{(i)})$ should be satisfied for the hydrostatic equilibrium where a pipe is filled with light fluid (see Fig. 2.2). From these, we find that the difference between the heights of the fluid surfaces at the two hydrostatic equilibrium $\delta x^{(i)}$ is given as

$$\delta x^{(i)} = x_{\text{ue}}^{(i-1)} - x_{\text{de}}^{(i)} = \frac{\delta\rho^{(i)}d}{\rho_{\text{H}}^{(i)} + \rho_{\text{L}}R}. \quad (2.42)$$

Thus, Eq. (2.41) is rewritten with an extremely simple form as

$$x - x_{\text{de}}^{(i)} = \frac{1}{6}\delta x^{(i)}. \quad (2.43)$$

Equation (2.43) suggests that the critical height for the flow instability is expressed only by difference between the heights of the fluid surfaces at the two hydrostatic equilibria. However, I will show in the following chapters that the critical height depends significantly on experimental parameters such as the viscosities of the fluids. Thus, the modification of this theoretical model is inevitable.

Chapter 3

Experiment

3.1 Experimental setup

3.1.1 Overview

The experimental setup is shown in Fig. 3.1. The density oscillator employed here consisted of an inner and an outer container, where the lower part of the outer container was immersed in a constant-temperature chamber and fixed with a magnet. A glass pipe was attached at the bottom of the inner container. The inner container was filled with heavy fluid, while the outer container with light fluid. The outer container was covered with an aluminum plate to prevent the fluid from evaporating. A laser displacement meter (Hokuyo, PDA-03KT) was fixed at the inner container, and connected to a digital multimeter. A stereomicroscope equipped with an Olympus DP70 digital camera was set outside the constant-temperature chamber in order to observe the lower part of the glass pipe, which was illuminated by a halogen lamp set at the other side of the chamber.

3.1.2 Containers and a pipe

Both inner and outer containers were made of acryl resin (Fig. 3.2). The bottom of the latter was attached to a stainless steel plate, so that it was fixed by the magnet attached at the bottom of the constant-temperature chamber. The surface areas of the inner and outer containers were $7.70 \times 10^{-4} \text{ m}^2$ and $5.34 \times 10^{-2} \text{ m}^2$, while their heights were 0.15 m and 0.32 m, respectively.

A glass pipe (PYREX) was attached vertically at the bottom of the inner container. The inner diameter and length of the pipe were 0.73 mm and 70 mm, respectively. As shown in Fig. 3.3, the cross section of the glass pipe was smooth, and the inner diameters at the upper and lower ends of the pipe were almost identical.

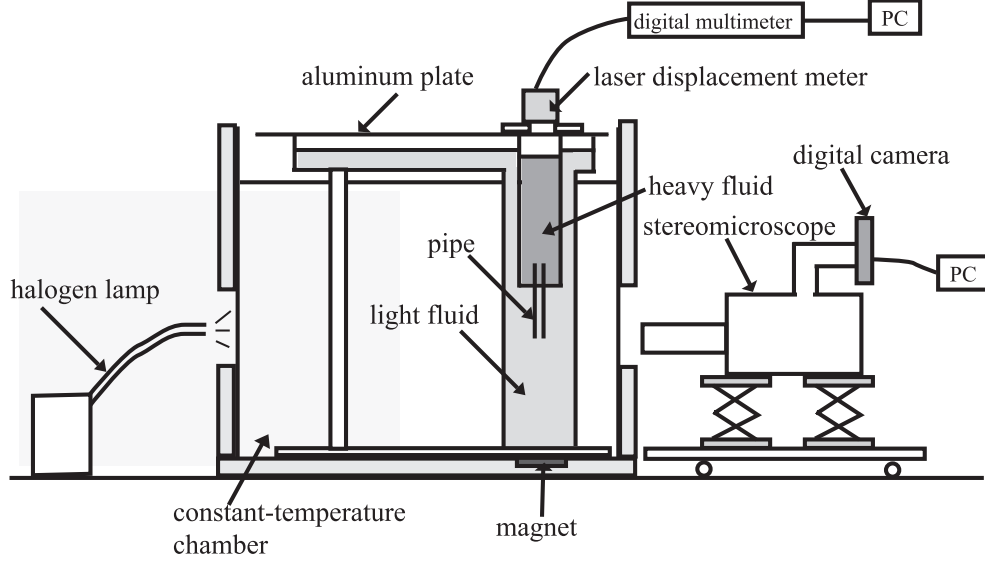


Figure 3.1: Overview of the experimental setup.

3.1.3 Fluids

Although salt water and pure water have been often used as the heavy and light fluids in the previous studies, they are not plausible for the present experiments, because it is needed to change the viscosities of fluids over a wide range. Thus, mixtures of water, 1-propanol, and glycerin were used for both the heavy and light fluids, where water mixed into the fluids was boiled before use in order to remove air bubbles. The viscosities of the fluids could be varied by changing their composition with their densities maintained, as shown in Fig. 3.4. The densities of the heavy and light fluids were set at $(1.057 \pm 0.003) \times 10^3 \text{ kg} \cdot \text{m}^{-3}$ and $(0.996 \pm 0.003) \times 10^3 \text{ kg} \cdot \text{m}^{-3}$, respectively, and hence the difference in densities between the fluids was $(0.061 \pm 0.004) \times 10^3 \text{ kg} \cdot \text{m}^{-3}$. From these conditions, it is found that $\beta\sigma^{1/2}/4 = 3.34 \times 10^{-2}$, and thus the experiments were performed in the viscous damping regime¹.

3.1.4 Temperature control

Since the temperature of the fluid relates to the viscosity of the fluid, the temperature of the fluids was regulated at $25.0 \pm 0.5^\circ\text{C}$ by immersing the lower part of the outer container in a constant-temperature chamber. Although the upper part of the outer container was not immersed in it, the temperature of the fluid near the pipe was well controlled.

¹Although $\beta\sigma^{1/2} \ll 1$ had to be satisfied so that the viscous damping regime was employed in the theory previously reported [31], it is obvious that it can be employed as far as $\beta\sigma^{1/2}/4 \ll 1$ is satisfied, because in this case the non-linear terms are negligibly small compared with the viscous terms in Eqs. (2.15) and (2.16).

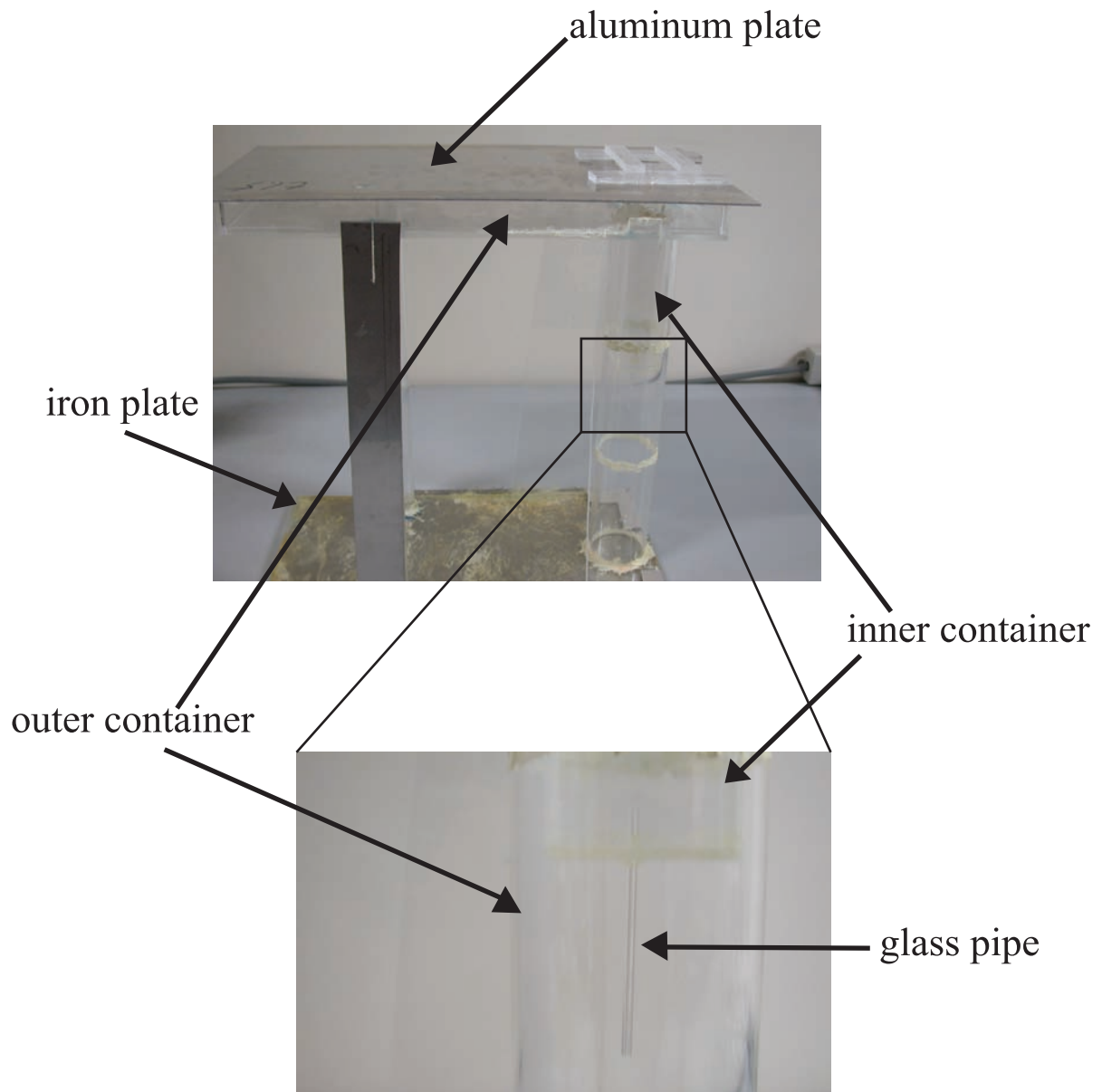


Figure 3.2: Inner and outer containers. Overview is shown in the upper picture. Magnified view of the bottom of the inner container is shown in the lower picture. A glass pipe is attached vertically at the bottom of the inner container.

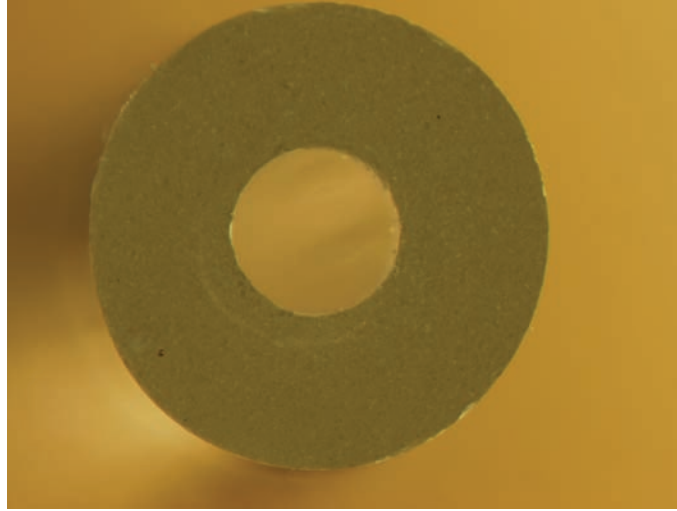


Figure 3.3: Cross section of a glass pipe observed by a stereomicroscope. The cross section is smooth and the distortion is not found. The internal diameter of the pipe is 0.73 mm.

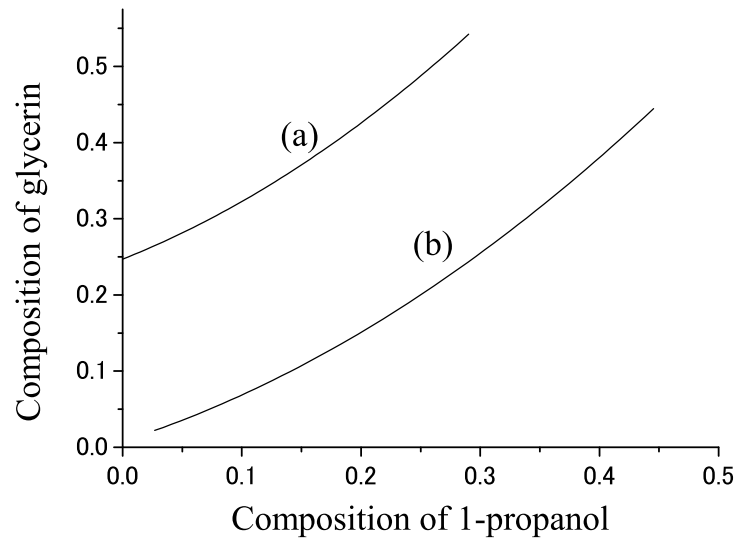


Figure 3.4: The composition curve of 1-propanol, glycerin and water to give a constant density of (a) $1.057 \times 10^3 \text{ kg} \cdot \text{m}^{-3}$ and (b) $0.996 \times 10^3 \text{ kg} \cdot \text{m}^{-3}$. The horizontal and vertical axes denote the ratio of the weight of 1-propanol and glycerin to that of the summation of the three materials, respectively.

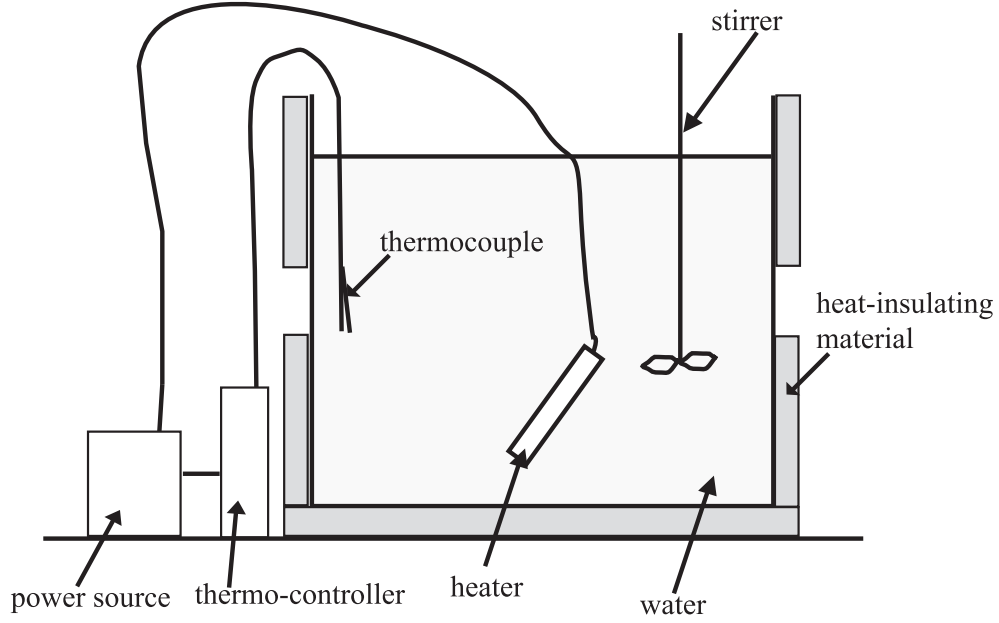


Figure 3.5: Scheme of the constant-temperature chamber. The temperature was controlled by a thermostat heater, in which the switch of the heater was regulated by sensing the temperature measured by a thermocouple. Water in the chamber was always stirred, and the chamber was covered with an heat-insulating material except for the pathway of the halogen lamp.

The scheme of the constant-temperature chamber was shown in Fig. 3.5. The temperature was controlled by a thermostat heater, in which the switch of the heater was regulated by sensing the temperature measured by a thermocouple. Water in the chamber was always stirred in order to avoid the inhomogeneity of the temperature. Moreover, the chamber was covered with a heat-insulating material except the pathway of the halogen lamp.

3.1.5 Laser displacement meter

The height of the heavy fluid surface was measured by a laser displacement meter (Hokuyo, PDA-03KT), in which the displacement of an object is measured by detecting the light reflected from an object by a position sensitive detector (PSD). Because PSD did not detect the light reflected from the fluid surface, a white acrylic plate was floated on the heavy fluid. The spatial resolution of the laser displacement meter was $1\ \mu\text{m}$.

In order to know the relation between the actual displacement and the output of the digital multimeter to which data was transmitted from the laser displacement meter, the following procedure was employed. A container was filled with water, and the height of the water level was measured by the laser displacement meter. Then the change of the output of the digital multimeter, which was in the unit of volt (V), was measured when

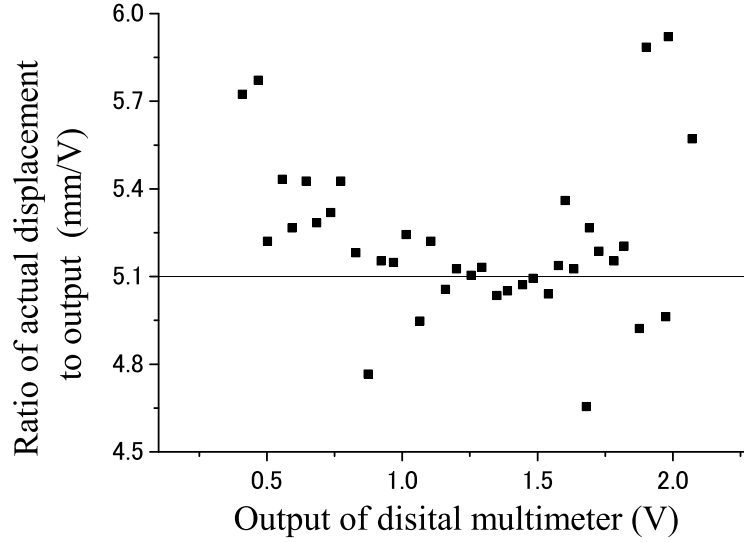


Figure 3.6: Relation between the actual displacement of the fluid surface and the output of the digital multimeter. A container was filled with water, and the height of the water level was measured by the laser displacement meter. The change of the output of the digital multimeter, which was in the unit of volt (V), was measured when the water level was changed by 0.48 mm using a micropipet. The horizontal axis denotes the output, while the vertical axis denotes the ratio of the actual displacement to the change of the output. When the output lies within a range of 0.70-1.70 V, the ratio is found to be approximately 5.10 mm/V.

the water level was changed by 0.48 mm using a micropipet. Figure 3.6 shows the ratio of the actual displacement to the change of the output. At the output of 0.70-1.70 V, the relation is found to be approximately 5.10 mm/V. Thus, all of the experiments were performed so that the output was within the range of 0.70-1.70 V, and the displacement in the unit of mm was calculated by multiplying 5.10 to the output in the unit of V.

3.1.6 Stereomicroscope

The lower part of the pipe was observed through a stereomicroscope. The interface of the two fluids was clearly observed owing to the difference in their refractive indices. The stereomicroscope was movable by setting it on a couple of laboratory jacks which were placed on a plate equipped with several beads whose diameters were about 12 mm, and the plate was fixed with magnet bases (see Fig. 3.7). A halogen lamp was used as an illuminating source and set at the other side of the constant-temperature chamber. The location of the halogen lamp and the stereomicroscope were adjusted so that the image of the pipe was not blurred.

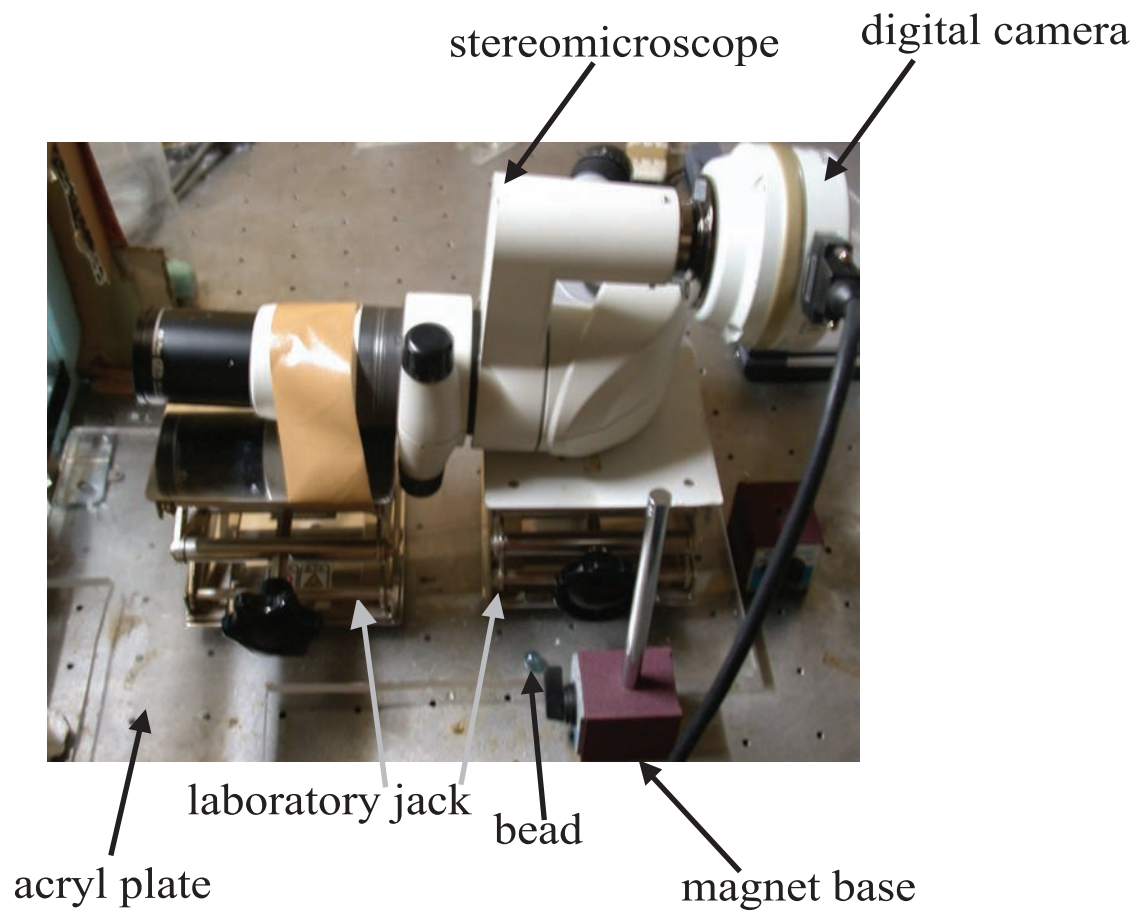


Figure 3.7: A stereomicroscope equipped with an Olympus DP70 digital camera. The stereomicroscope was movable by setting it on a couple of laboratory jacks which were placed on an acryl plate with several beads. The acryl plate was fixed with magnet bases.

3.2 Experimental procedure

Firstly, the fluids were prepared for the experiment. Appropriate amounts of water, 1-propanol, and glycerin were mixed and well stirred. Then, the heavy fluid was put into a flask and was immersed in the constant-temperature chamber for more than thirty minutes so that the temperature of the fluid becomes $25.0 \pm 0.5^\circ\text{C}$. The light fluid was poured into the outer container, and was also immersed in the constant-temperature chamber. Meanwhile, a small amount of the prepared fluids were used to measure the densities and viscosities, which were measured by using a volumetric flask and an Ostwald viscometer, respectively.

Next, the heavy fluid was poured into the inner container, which was set in the outer container. In this step, great care was taken so that air bubbles did not generate. The heights of the heavy and light fluid surfaces were first set to be nearly equal, so that the oscillation began with down-flow. Although the fluid in the outer container was somewhat disturbed when we set the inner container, such disturbance diminished until the first flow reversal occurred. After the setting of the inner container, the white acrylic plate in which water-repellency treatment was performed was floated on the heavy fluid and the laser displacement meter was fixed to the inner container with gummed tape. Here, the inner container was almost completely covered with the gummed tape, so that the evaporation of the heavy fluid did not occur. Then, the height of the heavy fluid surface was recorded at an interval of more than 500 ms, and for more than 6 cycles. An Olympus DP70 digital camera was equipped with the stereomicroscope, and the pictures were taken at an interval of more than 1 s, where the interval was determined by the period of oscillation.

Chapter 4

Results and analyses

4.1 General trend

4.1.1 Height of a fluid surface

First, let us see the general trend of the temporal evolution of the height of the heavy fluid surface measured by the laser displacement meter. Figure 4.1 shows the case where the viscosities of the heavy and light fluids are not extremely large compared with pure water. In the present experimental condition, the pipe diameter and length are 0.73 and 70 mm, and the densities of the heavy and the light fluid are $1.057 \times 10^3 \text{ kg} \cdot \text{m}^{-3}$ and $0.997 \times 10^3 \text{ kg} \cdot \text{m}^{-3}$, respectively. It is found that the fluid surface moves up and down regularly, and the average height shows a slow but continuous increase. This is because the accumulation of the light fluid into the inner container causes a periodic decrease in the density of the heavy fluid. Thus, as the number of cycles increases, the outputs of the laser displacement meter get out of its measurement range, *i.e.*, 0.7-1.7 V (Fig. 4.1(a)).

Figure 4.2 shows the durations of up- and down-flow and the amplitude of oscillation plotted against the number of cycles. It is clearly seen that both durations and amplitude are kept almost constant for the first about 10 cycles. However, as the number of cycles increases, the amplitude decreases gradually, whereas the durations do not vary significantly. This is probably not only because the outputs of the laser displacement meter get out of its measurement range, but also because the average difference in densities decreases as the number of cycles increases. Although the oscillatory behavior more than 28 cycles is not quantitatively measured, it is considered that the amplitude continues to decrease. Then, the oscillation finally stops.

Next, let us turn our attention to each up- and down-flow. As is expected from Eqs. (2.19) and (2.20), the temporal evolution for each flow between two adjacent flow reversals can be expressed by an exponential function, although it slightly deviates from the

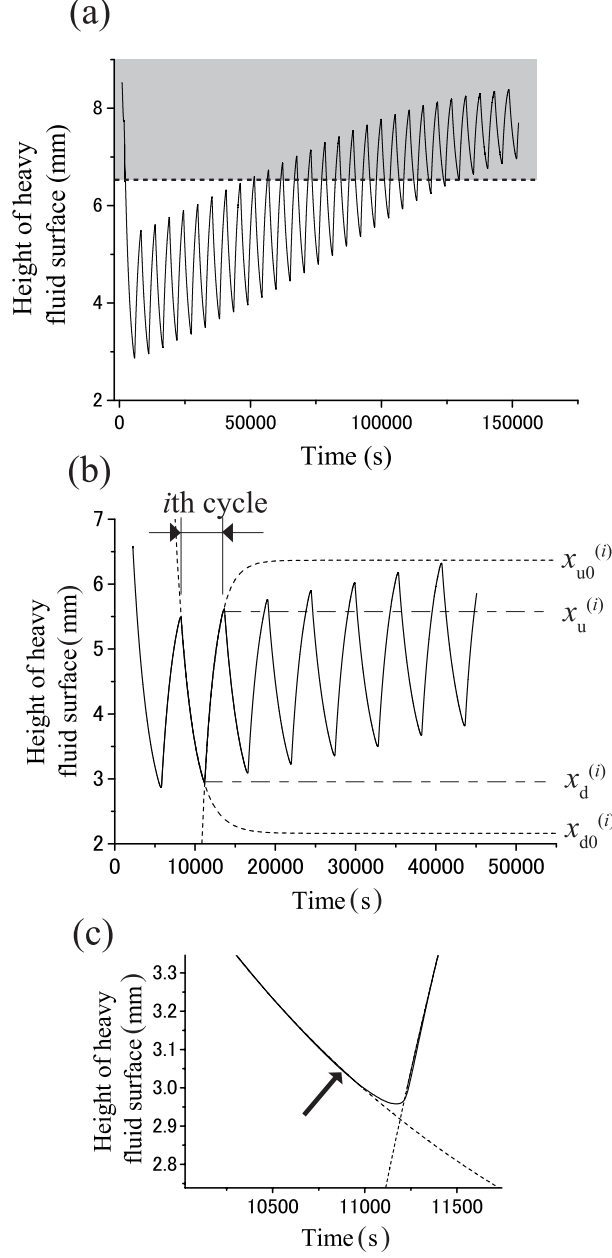


Figure 4.1: Temporal evolution of the height of the heavy fluid surface. $\mu_H = 2.64 \times 10^{-3} \text{ Pa} \cdot \text{s}$, and $\mu_L = 1.98 \times 10^{-3} \text{ Pa} \cdot \text{s}$, $\rho_L = 0.997 \times 10^3 \text{ kg} \cdot \text{m}^{-3}$, and $\delta\rho = 0.062 \times 10^3 \text{ kg} \cdot \text{m}^{-3}$. The pipe diameter and length are 0.73 and 70 mm, respectively. (a) Long time behavior of oscillation. The fluid surface moves up and down regularly, and the average height shows a slow but continuous increase. In the gray region, the outputs of the laser displacement meter are out of its measurement range, and hence the obtained data is inaccurate. (b) Magnified view of (a). Each branch for up- and down-flow is well fitted by an exponential curve (dashed line). The definition of the parameters for the i th cycle is also shown. The dashed-and-dotted lines denote the heights at which the flow reverses from the i th up- to the $(i+1)$ th down- and from the i th down- to the i th up-flow. In the present graph, $i = 2$. (c) magnified view of (b) at the flow reversal from down- to up-flow. An arrow denotes the height of the heavy fluid surface when the intrusion length becomes 1 mm.

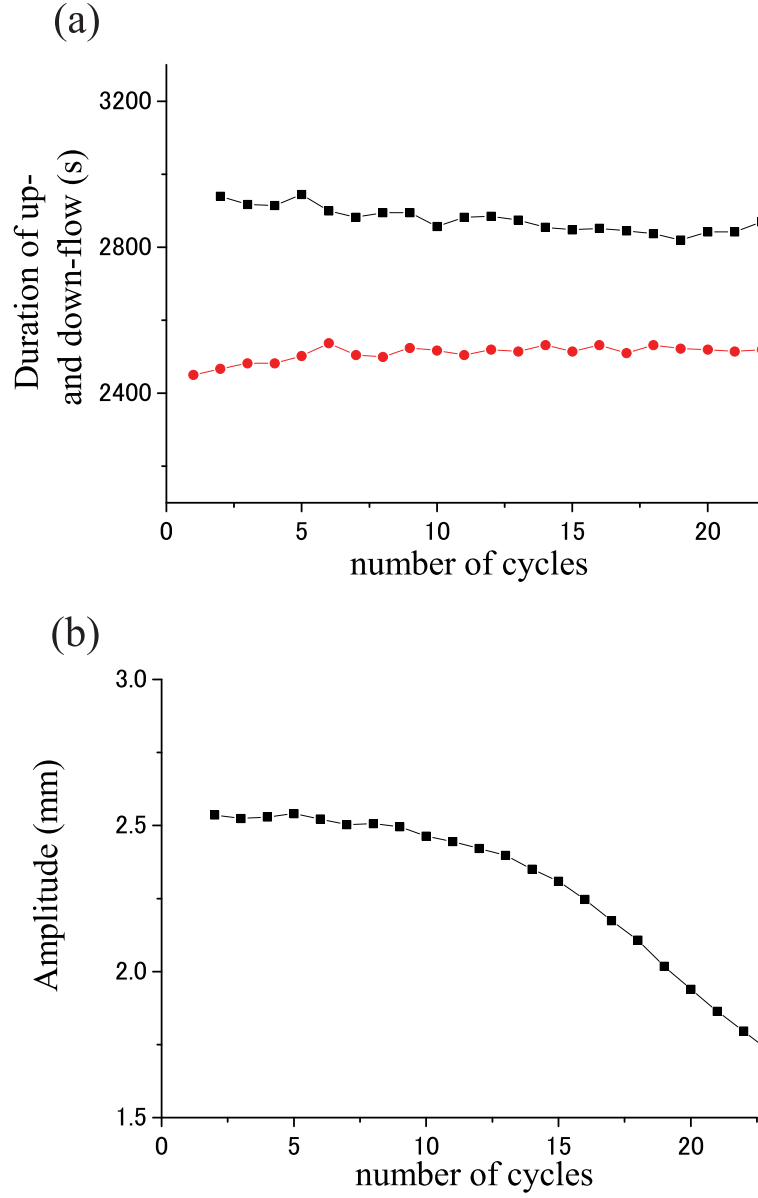


Figure 4.2: The durations of up- and down-flow and the amplitude of oscillation versus number of cycles. (a) The duration of up-flow (red circle) and down-flow (black square). (b) The amplitude. $\mu_H = 2.64 \times 10^{-3} \text{ Pa} \cdot \text{s}$, and $\mu_L = 1.98 \times 10^{-3} \text{ Pa} \cdot \text{s}$, $\rho_L = 0.997 \times 10^3 \text{ kg} \cdot \text{m}^{-3}$, and $\delta\rho = 0.062 \times 10^3 \text{ kg} \cdot \text{m}^{-3}$. The pipe diameter and length are 0.73 and 70 mm, respectively.

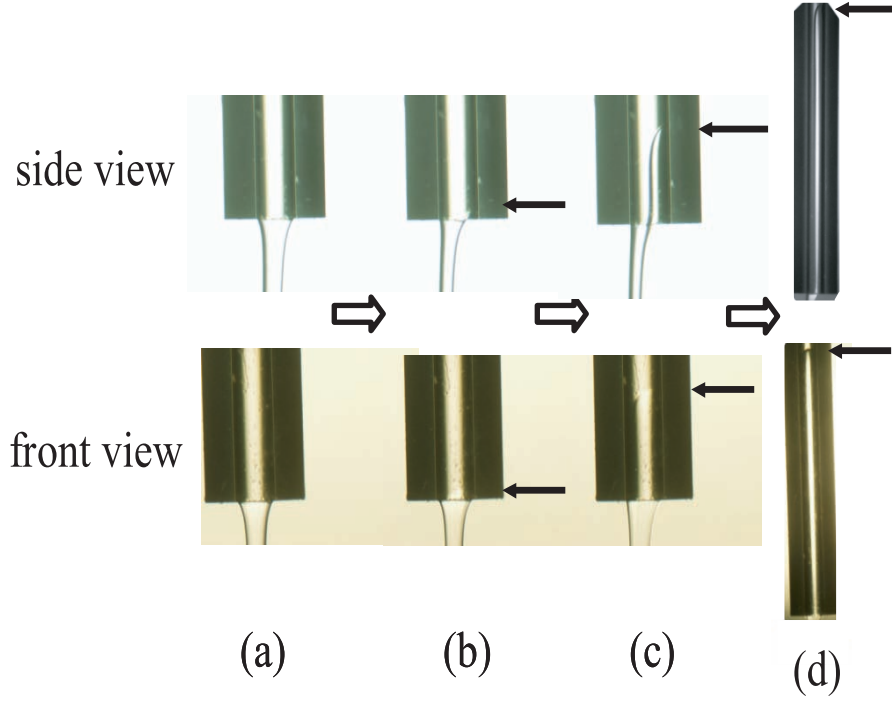


Figure 4.3: Microscopic images of the intrusion in the time course of down-flow ((a)→(b)→(c)→(d)). Upper and lower images show the side and front views, respectively. An intrusion of light fluid is clearly seen (arrows). Glucose solution and water are used as the heavy and light fluids, respectively, with $\rho_L = 0.997 \times 10^3 \text{ kg} \cdot \text{m}^{-3}$, $\delta\rho = 0.067 \times 10^3 \text{ kg} \cdot \text{m}^{-3}$, $\mu_H = 1.42 \times 10^{-3} \text{ Pa} \cdot \text{s}$ and $\mu_L = 0.89 \times 10^{-3} \text{ Pa} \cdot \text{s}$. Although the experimental condition employed in this figure is slightly different from that employed in the present chapter, the difference is not crucial, as the behavior observed is almost identical.

exponential function before the flow reversal (Fig. 4.1(c)). The time constants of the exponential functions fitted to the up- and down-flows are found to be $1.99 \times 10^3 \text{ s}$ and $1.58 \times 10^3 \text{ s}$ in the average of the 2nd to 5th cycles, which are in good agreement with the values obtained from Eqs. (2.19) and (2.20), $1.97 \times 10^3 \text{ s}$ and $1.57 \times 10^3 \text{ s}$, respectively. Moreover, the difference between the asymptotic values of the two adjacent exponential functions is found to be 4.10 mm in the average of the 2nd to 5th cycles, which is in good agreement with the difference between the two hydrostatic equilibria, 4.03 mm, that is calculated from Eq. (2.42). Thus, since the exponential curves are characterized by the time constants and their asymptotic values, it is found that each up- and down-flow is well described by Eqs. (2.19) and (2.20).

4.1.2 Flow-reversal process inside a pipe

Although each up- and down-flow exhibits an exponential response as described above, the flow reverses before the fluid surface reaches the asymptotic value of the exponential

function (Fig. 4.1). To investigate the mechanism of the flow reversal in detail, its process is observed by a stereomicroscope. Figure 4.3 shows an example at the flow reversal from the down- to up-flow. At first, the heavy fluid flows downward, as shown in Fig. 4.3(a) (In the following, we call this process as “process A”). After a while, an intrusion of the light fluid into a pipe is observed and grows upwards along the pipe wall rather slowly (Fig. 4.3(b)) (“process B”). When the intrusion length measured from the bottom of the pipe grows to some extent, it suddenly starts to grow rapidly (Figs. 4.3(c) and (d)) (“process C”). Although we cannot evaluate the intrusion length quantitatively when it becomes larger than 8mm because of the limitation of the visual field of the stereomicroscope, the intrusion becomes accelerated as it approaches the upper end of the pipe, and finally the flow reverses when it reaches the upper end of the pipe. It is noted that the deviation from an exponential function in the height of the fluid surface occurs at the process C (see Fig. 4.1(c)). The flow reversal from up- to down-flow occurs in the same way as that from down- to up-flow.

4.2 Viscosity dependence

When the viscosity of the fluid is varied, the oscillatory behavior changes drastically. Figure 4.4 shows examples of the temporal evolutions in the case of extremely high viscosity applied to the heavy or light fluid. As is expected, the time constant of the exponential curve varies according to the viscosity of the fluid, although the difference between the asymptotic values for the exponential curves, Δ , is still almost consistent with δx , as shown in Fig. 4.5. Figure 4.6 shows the time constants of the exponential curves fitted for the up- and down-flow. The experimental results are also in fairly good agreement with the theoretical values τ_u and τ_d obtained from Eqs. (2.19) and (2.20), although there is a slight systematic deviation at high viscosities, which is thought to be caused by the reduction in the viscosity of the high viscosity fluid due to the inflow of the low viscosity fluid. Thus, even when the viscosity of the light or heavy fluid is varied, each branch for the up- and down-flow is well described by Eqs. (2.19) and (2.20).

However, when we compare Fig. 4.4 with Fig. 4.1, we notice that a drastic change occurs at the timing of the flow reversal. When the viscosity of the heavy fluid μ_H is extremely large, the flow reversal from down- to up-flow occurs even when the height of the heavy fluid surface is still high, while that from up- to down-flow does not occur until the fluid surface becomes close to the hydrostatic equilibrium (Fig. 4.4(a)). On the contrary, when the viscosity of the light fluid μ_L is extremely large, the flow reversal from up- to down-flow occurs even when the fluid surface is still low, while that from down- to up-flow does not occur until the fluid surface becomes close to the hydrostatic

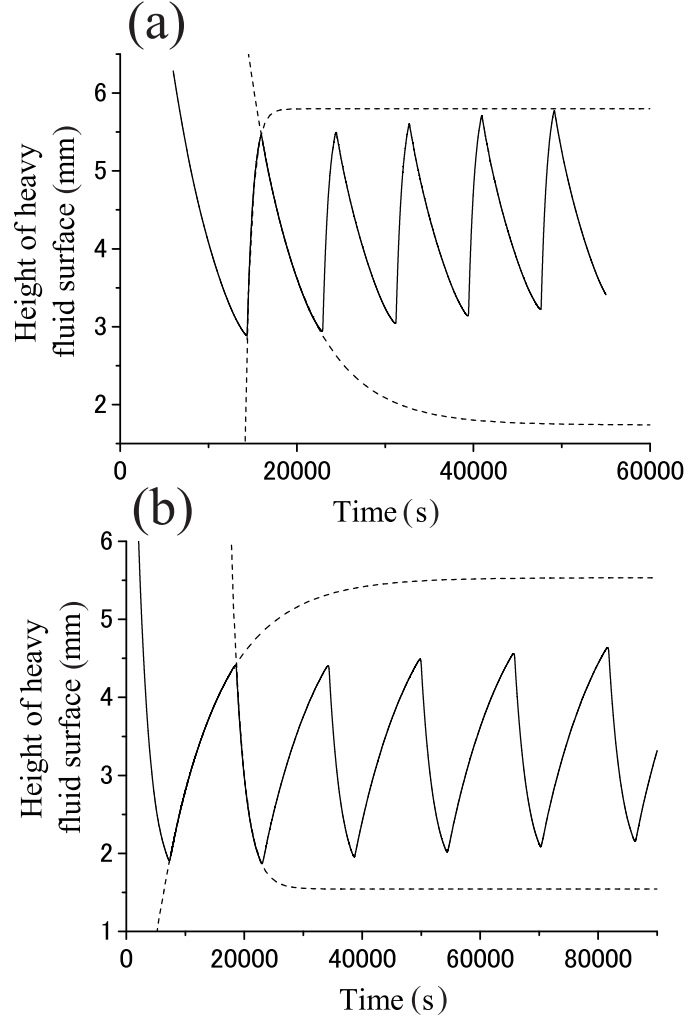


Figure 4.4: Temporal evolution of the height of the heavy fluid surface, in the case of (a) $\mu_H = 8.59 \times 10^{-3} \text{ Pa} \cdot \text{s}$, and $\mu_L = 0.89 \times 10^{-3} \text{ Pa} \cdot \text{s}$, $\rho_L = 0.997 \times 10^3 \text{ kg} \cdot \text{m}^{-3}$, $\delta\rho = 0.060 \times 10^3 \text{ kg} \cdot \text{m}^{-3}$, and (b) $\mu_H = 2.66 \times 10^{-3} \text{ Pa} \cdot \text{s}$, and $\mu_L = 14.18 \times 10^{-3} \text{ Pa} \cdot \text{s}$, $\rho_L = 0.996 \times 10^3 \text{ kg} \cdot \text{m}^{-3}$, $\delta\rho = 0.062 \times 10^3 \text{ kg} \cdot \text{m}^{-3}$. Each branch for up- and down-flow is well fitted by an exponential curve (dashed line).

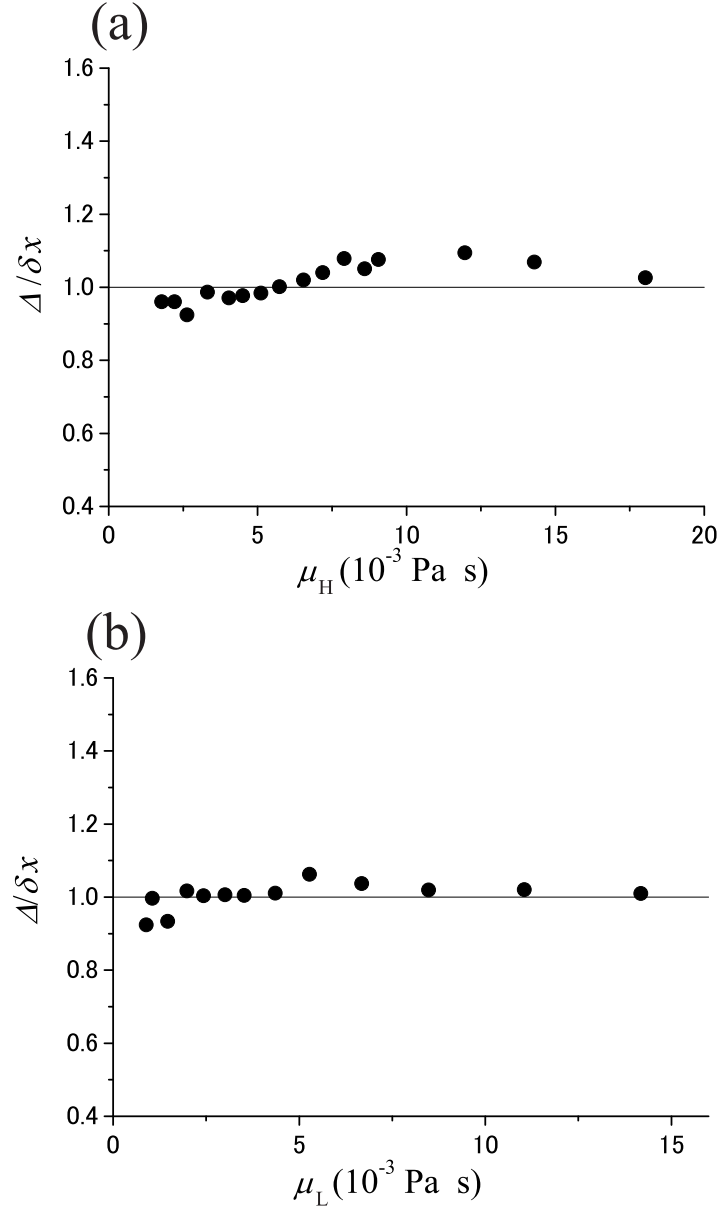


Figure 4.5: Ratio of the difference between the asymptotic values for the exponential curves Δ to the difference between the two hydrostatic equilibrium δx . Each data is averaged over 4 cycles from the 2nd to 5th. (a) μ_H is varied while μ_L is fixed at 0.89×10^{-3} Pa \cdot s. (b) μ_L is varied while μ_H is fixed at $(2.63 \pm 0.03) \times 10^{-3}$ Pa \cdot s. Even when the viscosities of fluids are varied, Δ almost agrees with δx .

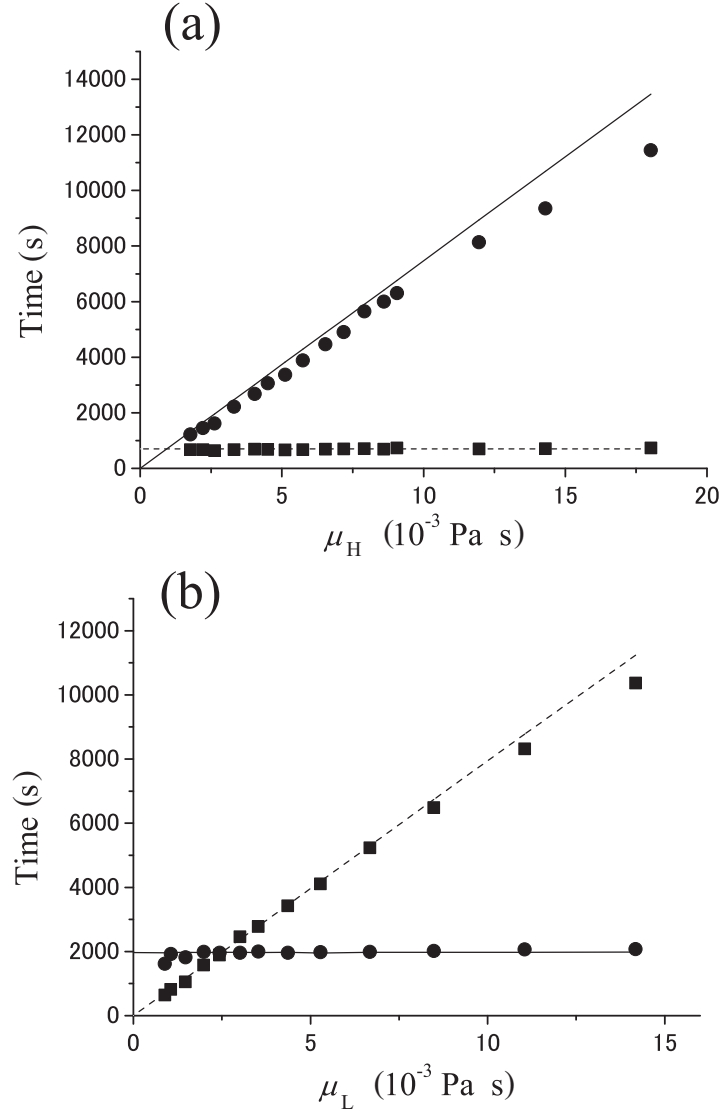


Figure 4.6: Time constants of the exponential curves fitted for each down- and up-flow (filled circle and square, respectively). Each data is averaged over 4 cycles from the 2nd to 5th. (a) μ_H is varied while μ_L is fixed at 0.89×10^{-3} Pa \cdot s. (b) μ_L is varied while μ_H is fixed at $(2.63 \pm 0.03) \times 10^{-3}$ Pa \cdot s. The solid and dashed lines indicate the theoretical values for τ_d and τ_u , respectively.

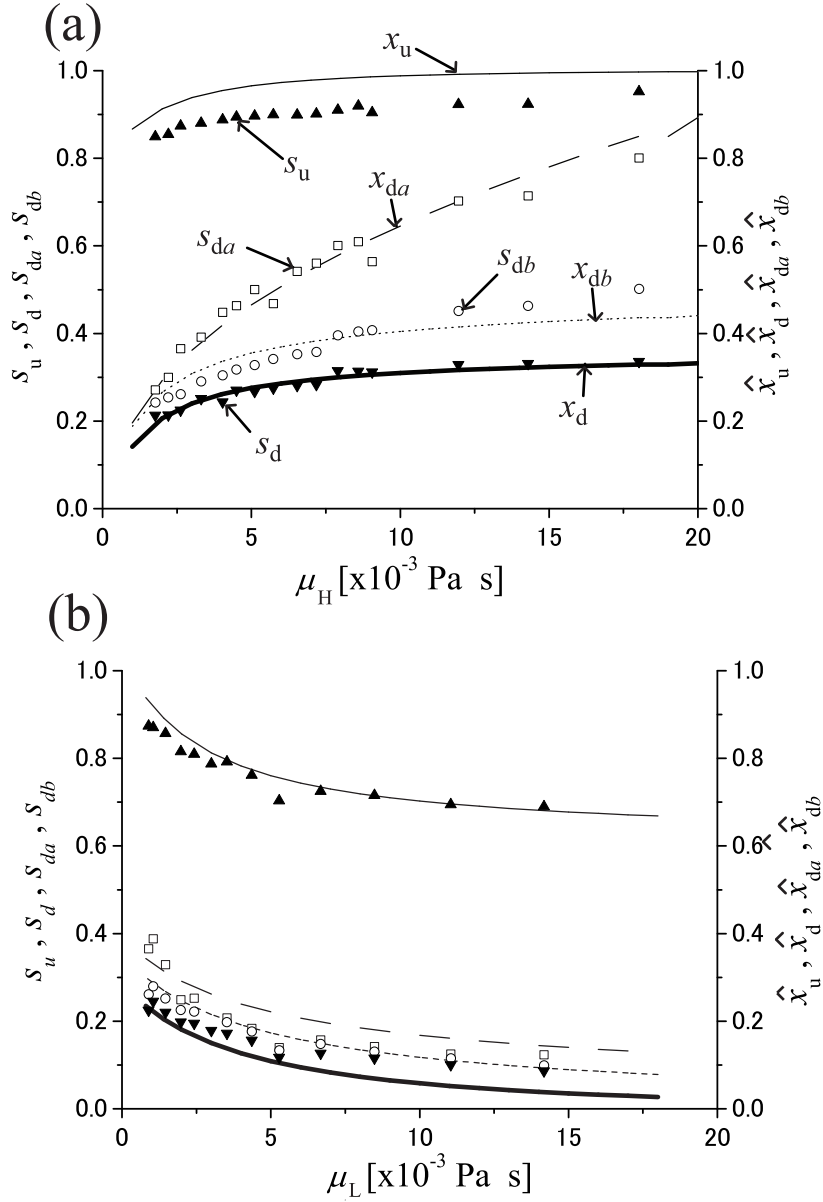


Figure 4.7: Viscosity dependence of s_u (filled up triangle), s_d (filled down triangle), s_{da} (open square), and s_{db} (open circle). The data are averaged over 4 cycles from the 2nd to the 5th. Simulated results \hat{x}_u (solid line), \hat{x}_d (bold line), \hat{x}_{da} (dashed line), and \hat{x}_{db} (dotted line) are also shown. (a) μ_H is varied while μ_L is fixed at 0.89×10^{-3} Pa s. (b) μ_L is varied while μ_H is fixed at $(2.63 \pm 0.03) \times 10^{-3}$ Pa s. The parameters of the simulation are as follows: $a = 0.365$ mm, $d = 70$ mm, $\rho_H = 1.057 \times 10^3$ kg m $^{-3}$, $\rho_L = 0.996 \times 10^3$ kg m $^{-3}$, $S = 7.70 \times 10^{-4}$ m 2 , $R = 1.44 \times 10^{-4}$, $b_1 = 10.7$, $b_2 = 160$, $k = 0.40$ kg m $^{-1}$ s $^{-3}$, $C_1=7.11$, $C_2=5.31$, $C_3=0.32$, $\alpha'=1.82$, and $\gamma'=0.30$.

equilibrium. In order to evaluate such viscosity-dependent behaviors quantitatively, the following two parameters, s_d and s_u , are defined as

$$s_d = \left\langle \frac{x_d^{(i)} - x_{d0}^{(i)}}{x_{u0}^{(i-1)} - x_{d0}^{(i)}} \right\rangle \quad (4.1)$$

$$s_u = \left\langle \frac{x_u^{(i-1)} - x_{d0}^{(i)}}{x_{u0}^{(i-1)} - x_{d0}^{(i)}} \right\rangle, \quad (4.2)$$

where $x_d^{(i)}$ and $x_u^{(i)}$ are the heights of the heavy fluid surface at the moments when the flow reverses from the i th down- to the i th up-flow and from the i th up- to the $(i+1)$ th down-flow, respectively. $x_{d0}^{(i)}$ and $x_{u0}^{(i)}$ are the asymptotic values for the exponential curves fitted to the i th down- and up-flow, respectively (see Fig. 4.1(b)). In the present analysis, we have averaged the data over four cycles from the 2nd to 5th in a series of experiments. In fact, s_d and s_u are expected to be suitable parameters for qualifying the timing of the flow reversal over the entire process leading to the asymptotic equilibrium, because $x_{d0}^{(i)}$ and $x_{u0}^{(i-1)}$ are thought to be almost consistent with the hydrostatic equilibrium where the pipe is filled with heavy and light fluid, $x_{de}^{(i)}$ and $x_{ue}^{(i-1)}$, respectively, with a density difference of $\delta\rho^{(i)}$. Figure 4.7 shows the viscosity dependence of s_d and s_u when the viscosity of either heavy or light fluid is varied. It is clear that both s_d and s_u increase when the viscosity of the heavy fluid increases, but decrease when that of the light fluid increases. These results cannot be explained in terms of theories proposed so far, in which the critical heights do not depend on the viscosity of fluids [40].

Thus, it becomes clear that the flow-reversal process is significantly affected by the viscosity of the fluid. Figure 4.8 shows the temporal evolution of the intrusion length when the viscosity of either heavy or light fluid is varied. Here, we set the origin of time at the very moment of the flow reversal and plot the intrusion length against the time leading to the flow reversal. It is clearly seen that the intrusion grows slowly at first (process B), but begins to grow rapidly when the intrusion length exceeds about 1 mm (process C).

For a large μ_H and small μ_L , the intrusion of the light fluid persists an extremely long time before the flow reversal occurs, and the growth rate during the rapid-growing process is also relatively small, as shown in Fig. 4.8(a). On the other hand, for a large μ_L and small μ_H , the growth rate of the intrusion is relatively large and essentially does not depend on μ_L (Fig. 4.8(b)). However, in the latter case, it is observed that the interface between the two fluids is somehow disturbed at a certain intrusion length and its growth is thus obstructed for some time, particularly at a large μ_L . A typical example is shown in Fig. 4.9. In addition to the intrusion length, its width within the pipe depends on the viscosity of the fluids, as shown in Fig. 4.10. In general, the width is larger for $\mu_H > \mu_L$,

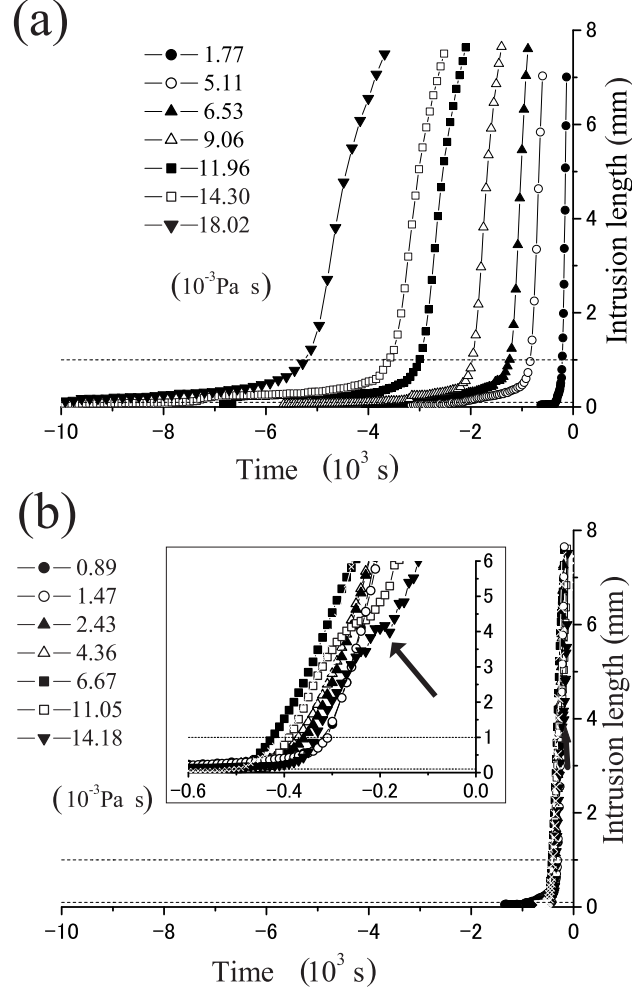


Figure 4.8: Viscosity-dependent temporal evolution of the intrusion of light fluid. (a) μ_H is varied while μ_L is fixed at 0.89×10^{-3} Pa·s. (b) μ_L is varied while μ_H is fixed at $(2.63 \pm 0.03) \times 10^{-3}$ Pa·s. Because of the limitation of the visual field under the stereomicroscope, an intrusion length of more than 8 mm is not observed. The dotted lines indicate 0.1 mm and 1 mm of intrusion length. The inset in (b) shows an enlarged view. The obstruction of the growth is observed at a large μ_L (shown as an arrow, see also Fig. 4.9).

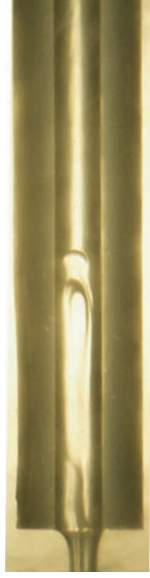


Figure 4.9: Front view of the disturbance of the interface at a large μ_L . $\mu_H = 2.66 \times 10^{-3} \text{ Pa} \cdot \text{s}$ and $\mu_L = 14.18 \times 10^{-3} \text{ Pa} \cdot \text{s}$.

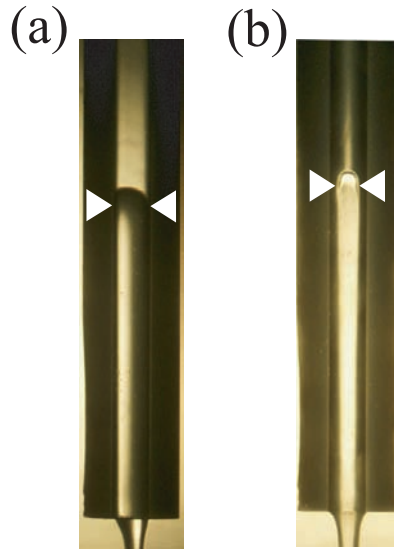


Figure 4.10: Front views of the intrusions during the flow-reversal processes for (a) $\mu_H = 18.02 \times 10^{-3} \text{ Pa} \cdot \text{s}$ and $\mu_L = 0.89 \times 10^{-3} \text{ Pa} \cdot \text{s}$, and (b) $\mu_H = 2.65 \times 10^{-3} \text{ Pa} \cdot \text{s}$ and $\mu_L = 8.48 \times 10^{-3} \text{ Pa} \cdot \text{s}$. The width of the intrusion is larger in (a) than in (b) (white arrow heads).

while it is smaller for $\mu_H < \mu_L$.

We characterize the viscosity-dependent behavior of the intrusion by employing the following two quantities:

$$s_{da} = \left\langle \frac{x_{da}^{(i)} - x_{d0}^{(i)}}{x_{u0}^{(i-1)} - x_{d0}^{(i)}} \right\rangle \quad (4.3)$$

$$s_{db} = \left\langle \frac{x_{db}^{(i)} - x_{d0}^{(i)}}{x_{u0}^{(i-1)} - x_{d0}^{(i)}} \right\rangle, \quad (4.4)$$

where $x_{da}^{(i)}$ and $x_{db}^{(i)}$ are the heights of the heavy fluid surface at the time when the intrusion lengths exceed 0.1 mm and 1 mm, respectively. Because the intrusion begins to grow rapidly when its length becomes nearly 1 mm, as shown in Fig. 4.8, the two quantities s_{da} and s_{db} roughly characterize the timings for the beginning of the intrusion (process B) and for the onset of its rapid growth (process C), respectively. With increasing μ_H , significant increases in both s_{da} and s_{db} are observed, which are more remarkable than those of s_d (Fig. 4.7(a)). Thus, the clear sign of the flow reversal is expressed, which is more prominent with increasing μ_H . On the other hand, with increasing μ_L , the behaviors of s_{da} and s_{db} are similar to those of s_d (Fig. 4.7(b)). Thus, these newly-introduced quantities sensitively characterize the dynamics of the flow reversal and then clarify definitively the viscosity dependence of the density oscillation.

Chapter 5

Modeling and simulation

As shown in Sec. 2.1, the behavior of each up- and down-flow of density oscillator was theoretically described in the study reported before [31]. However, to understand its overall behavior, it is clearly needed to describe the flow-reversal process correctly. The viscosity dependence of the flow reversal found in the previous chapter is helpful in understanding the fundamental mechanism of the flow reversal. Unfortunately, an exact treatment of flow stability is difficult owing to the complexity of the flow within a pipe during the flow-reversal process. Thus, a simple model describing the essential mechanism of the flow-reversal process is required. In the present chapter, I will propose a model by considering only forces parallel to a pipe wall, which acts on a unit volume element located at the tip of the intrusion. Here, the case of the viscous damping regime ($\beta\sigma^{1/2} \ll 1$) with the pipe length much larger than the diameter ($d \gg a$) is considered. In addition, we assume that the interface between the flow and the intrusion fluid is completely parallel to the pipe axis except for that at the tip of the intrusion, where it is assumed to be parallel to the cross section of the pipe (see Fig. 5.1).

5.1 Essential forces for flow reversal

In this section, the forces concerned with this phenomenon are considered separately. In the following, the case for the flow reversal from down- to up-flow is considered.

5.1.1 Viscous drag force

First, there should be a viscous drag force acting on a unit volume element. We denote this force as F_1 . F_1 should be given by the summation of the shear stresses acting on the inner and outer sides of the volume element (see green arrows in Fig. 5.1), which generates owing to the velocity difference of the down-flow and the intrusion growing upward, and the no-slip boundary condition at the pipe wall. Thus, it is found from

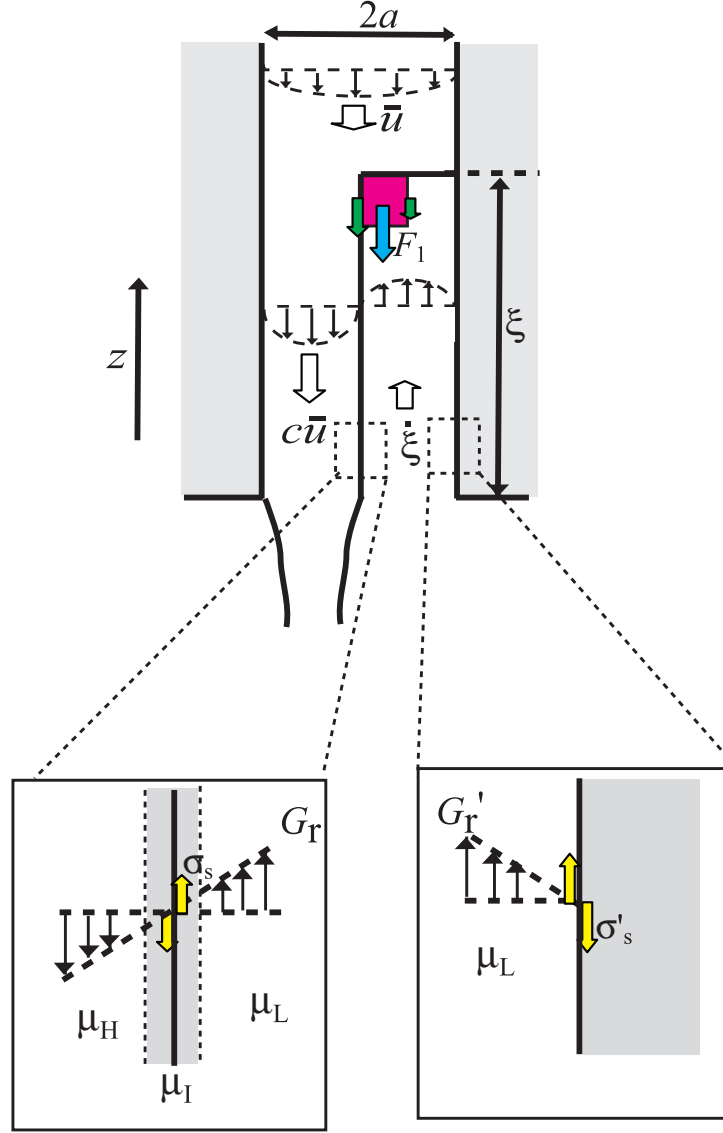


Figure 5.1: Scheme of the viscous drag force (blue arrow) acting on the unit volume element at the tip of the intrusion (red square). Velocity profiles of the down-flow and the intrusion are also shown. The mean velocity of the down flow where the intrusion does not exist is denoted as \bar{u} , while that in the presence of the intrusion is $c\bar{u}$. The growth rate of the intrusion is $\dot{\xi}$, where ξ denotes the intrusion length. Notice that upper direction is taken as positive for \bar{u} and ξ . The shear stresses acting on the inner and outer sides of the volume element are shown by green arrows. Lower pictures show the magnified views of the interface between the two fluids and that between the intrusion fluid and the pipe wall. Although the actual interface between the two fluids does not exist, an extremely thin volume element at the boundary between the two fluids is regarded as an interface (gray region), whose viscosity is denoted as μ_I . G_r and G'_r denote the gradient of the velocity profile at the interface between the two fluids and that at the pipe wall, respectively. The shear stress at the interface between the two fluids σ_s and that at the pipe wall σ'_s are also shown (yellow arrows).

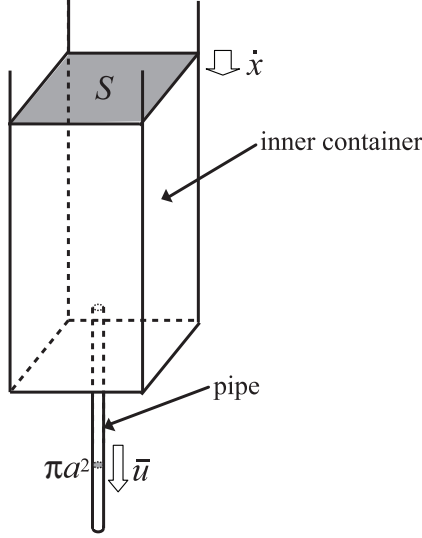


Figure 5.2: Relation between \dot{x} and \bar{u} (upper direction is taken as positive). The surface area of an inner container and the area of the cross section of a pipe is S and πa^2 , respectively.

the law of action and reaction that F_1 equals to the difference between the shear stress which the inner side of the volume element acts on the fluid flowing downward and that which the intrusion fluid acts on the outer side of the volume element. Then, because the difference arises within the unit length scale, F_1 is described by the radial gradient of the shear stress.

If we assume that the radial gradient of the shear stress is homogeneous with regard to the pipe radius, F_1 is derived by considering the shear stress at the interface between the two fluids and that at the pipe wall (see yellow arrows in Fig. 5.1). Let σ_s and σ'_s be defined as the shear stress acting on the fluid flowing downward at the interface between the two fluids and that acting on the intrusion fluid at the pipe wall, respectively. Because the difference between σ_s and σ'_s generates within a spatial scale of the pipe radius a , the radial gradient of the shear stress F_1 is described as

$$F_1 = \frac{\sigma'_s - \sigma_s}{a}. \quad (5.1)$$

Now let us derive σ_s and σ'_s individually. σ_s is given by the product of the viscosity and the velocity gradient at the interface between two fluids, which are denoted as μ_I and G_r , respectively. Actually, a definite interface between these two fluids will not exist, since the viscosity of the fluid will vary continuously in space because of the miscible nature of the heavy and light fluids. However, for convenience, it is assumed that the mixed region consists of an extremely thin volume element at an interface with a fluid having an appropriate viscosity. Since the viscosity of the fluid at the interface μ_I may be somehow dependent on the viscosities of the two fluids, the following relation is assumed

to hold:

$$\mu_I = \frac{\mu_H + \mu_L}{2}. \quad (5.2)$$

The velocity gradient at the interface G_r is estimated in the following way. When ξ is defined as the intrusion length, *i.e.*, the distance between the lower end of the pipe and the tip of the intrusion, the growth rate of the intrusion is given as $\dot{\xi}$. Meanwhile, the velocity of the down-flow in the presence of the intrusion is thought to be described as $c\bar{u}$, where c is a positive constant larger than unity and \bar{u} is the mean velocity of the flow inside a pipe (upper direction is taken as positive) when an intrusion does not exist (see Eq. (2.3)). Because the velocity difference between the intrusion and the down-flow generates within a spatial scale of the pipe radius a , G_r should satisfy

$$G_r \propto \frac{\dot{\xi} - c\bar{u}}{a}. \quad (5.3)$$

Here, as shown in Eq. (2.7), \bar{u} is related to \dot{x} from the condition of continuity as (see Fig.5.2)

$$S\dot{x} = \pi a^2 \bar{u}. \quad (5.4)$$

Hence, σ_s is derived using Eqs. (5.2), (5.3), and (5.4) as

$$\begin{aligned} \sigma_s &= \mu_I G_r \\ &\propto \frac{\mu_H + \mu_L}{2} \frac{\dot{\xi} - c(S/\pi a^2)\dot{x}}{a}. \end{aligned} \quad (5.5)$$

On the other hand, the shear stress at the pipe wall σ'_s is also given by the product of the viscosity and the velocity gradient on the pipe wall. Here, for simplicity, we assume that the viscosity is equal to μ_I , although it is considered that the viscosity on the pipe wall is actually equal to μ_L . As I will discuss in Sec. 7.1, this assumption is not essentially important in the processes A and B, although the growth rate of the intrusion in the process C is thought to be somewhat affected by this assumption. Meanwhile, because the velocity difference between the intrusion and the pipe wall generates within a spatial scale of the pipe radius a , the velocity gradient on the pipe wall G'_r is given under the assumption of no-slip condition as

$$G'_r \propto -\frac{\dot{\xi}}{a}. \quad (5.6)$$

Thus, σ'_s is described as

$$\sigma'_s \propto -\frac{\mu_H + \mu_L}{2} \frac{\dot{\xi}}{a}, \quad (5.7)$$

Thus, from Eqs. (5.1), (5.5) and (5.7), the viscous drag force F_1 is derived as

$$F_1 = \frac{\mu_H + \mu_L}{2a^2} \left(b_1 \frac{S}{\pi a^2} \dot{x} - b_2 \dot{\xi} \right), \quad (5.8)$$

where b_1 and b_2 are positive constants. It is noticed that the first term in the right hand side of Eq. (5.8) is originated only from σ_s , while the second term includes the contributions of both σ_s and σ'_s .

5.1.2 Hydrostatic pressure gradient

Second, there must be a gravitational force and the force due to the gradient of hydrostatic pressure. Let these forces be denoted as F_2 . When the intrusion exists sufficiently at the interior of the pipe, F_2 will satisfy the relation

$$F_2 = -\frac{P(d) - P(0)}{d} - \rho_L g, \quad (5.9)$$

where $P(d)$ and $P(0)$ are the hydrostatic pressures at the upper and lower ends of the pipe (see Fig. 5.3). Here, we have assumed that the gradient of the hydrostatic pressure is homogeneous inside the pipe. The second term in the right hand side of Eq. (5.9) denotes the gravitational force acting on the unit volume element. Notice that the density of the volume element is assumed to be ρ_L , because it exists within the intrusion fluid. Because the viscous damping regime is now considered, the effect of ‘head loss’ (see Sec. 2.1) can be neglected. Thus, if $P(d)$ and $P(0)$ are assumed to be simply derived from the heights of the fluid surfaces, they are given as (see Fig. 5.3)

$$P(d) = \rho_H g(x - d), \quad (5.10)$$

$$P(0) = \rho_L g h. \quad (5.11)$$

Here, the heights of the heavy and light fluid surfaces x and h are related through R , which is the ratio of the surface area of the heavy fluid to that of the light fluid, in the following way (see Eq. (2.6)):

$$h - h_{de} = -R(x - x_{de}), \quad (5.12)$$

where x_{de} and h_{de} should satisfy (see Eq. (2.12))

$$\rho_H x_{de} = \rho_L h_{de}. \quad (5.13)$$

By substituting Eqs. (5.10), (5.11), (5.12) and (5.13) into Eq. (5.9), we obtain

$$\begin{aligned} F_2 &= -\frac{\rho_H g(x - d) - \rho_L g h}{d} - \rho_L g \\ &= -\frac{\rho_H g x}{d} + \frac{\rho_L g}{d} \left[-R(x - x_{de}) + \frac{\rho_H}{\rho_L} x_{de} \right] + \delta \rho g \\ &= -\frac{\rho_H g(x - x_{de})(1 + RD)}{d} + \delta \rho g, \end{aligned} \quad (5.14)$$

where $D = \rho_L / \rho_H$ and $\delta \rho = \rho_H - \rho_L$.

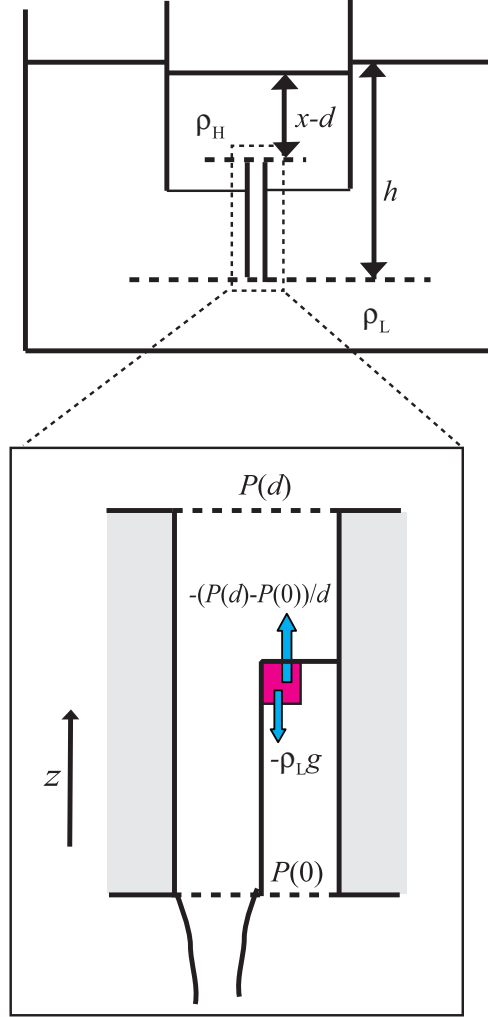


Figure 5.3: Scheme of the hydrostatic pressure gradient (up-blue arrow) and the gravitational force (down-blue arrow) acting on the unit volume element (red square). $P(d)$ and $P(0)$ are the hydrostatic pressures at the upper and lower ends of the pipe. If the hydrostatic pressure is assumed to be derived simply from the height of the fluid surface, $P(d)$ and $P(0)$ are obtained like Eqs. (5.10) and (5.11), which can be easily understood from the upper picture.

On the other hand, if the volume element of the light fluid exists outside the pipe, it is obvious that the hydrostatic pressure gradient balances the gravitational force. Hence, when there is no intrusion ($\xi = 0$), the relation $F_2 = 0$ should be automatically satisfied. However, it is unnatural that the value of F_2 jumps from 0 to $-\rho_H g(x - x_{de})(1 + RD)/d + \delta\rho g$ discontinuously with regard to ξ at $\xi = 0$. This contradiction comes from the assumption that the hydrostatic pressures $P(d)$ and $P(0)$ are simply derived from the height of the fluid surface. Actually, it is considered that the flow near the end of a pipe is thought to be complicated and hence the hydrostatic pressure near the end deviates from that expected from the height of the fluid surface.

Although it is difficult to obtain the hydrostatic pressure strictly, we will describe it phenomenologically so that F_2 becomes continuous at $\xi = 0$. It seems appropriate to describe F_2 in the following way:

$$F_2 = \left[-\frac{\rho_H g(x - x_{de})(1 + RD)}{d} + \delta\rho g \right] (1 - e^{-\xi/\alpha}). \quad (5.15)$$

The term $(1 - e^{-\xi/\alpha})$ is introduced in order to connect $F_2 = -\rho_H g(x - x_{de})(1 + RD)/d + \delta\rho g$ for $\xi \gg \alpha$ and $F_2 = 0$ at $\xi = 0$. Here, α characterizes the spatial range where F_2 takes a value between 0 and $-\rho_H g(x - x_{de})(1 + RD)/d + \delta\rho g$.

5.1.3 Effect of acceleration of fluid outside a pipe

Third, the effect of the acceleration of the fluid outside the pipe should be considered. Let us arbitrarily consider two planes inside and outside the pipe as PL_1 and PL_2 , as shown in Fig. 5.4. The absolute value of the mean velocity of the flow at PL_2 is defined as V , while that at PL_1 is $-\bar{u}$. Since the heavy fluid that has passed through the pipe is accelerated due to the hydrostatic pressure gradient, the following relation is expected to hold:

$$V = -\bar{u} + \kappa, \quad (5.16)$$

where κ expresses the effect of the acceleration. The continuity condition naturally holds, which results in

$$-\bar{u}\pi a^2 = VS_c, \quad (5.17)$$

where S_c denotes the area of the cross section of the down-flow in a plane of PL_2 . When S_c is sufficiently small, it is expected that the intrusion of the light fluid is enforced as a consequence, because the contraction of the flow causes a detachment of the down-flow from the pipe wall. F_3 is defined as the force due to this enforcement. Since it seems difficult to derive F_3 analytically, I will describe it phenomenologically. It is found from Eqs. (5.16) and (5.17) that $-\bar{u} = \kappa(\pi a^2/S_c - 1)^{-1}$. Hence, since F_3 increases as S_c decreases, it is qualitatively found that F_3 increases as $-\bar{u}$ decreases. In addition, F_3 is

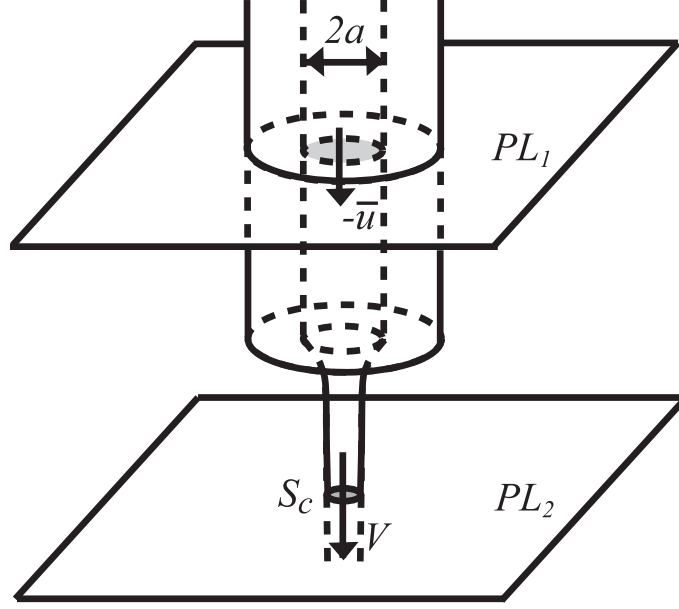


Figure 5.4: Schematic illustration of two planes, PL_1 and PL_2 , which are vertical to the direction of the flow. PL_1 crosses the pipe, while PL_2 is below but not too far from the lower end of the pipe. S denotes the surface area of down-flow at PL_2 . $-\bar{u}$ and V are the absolute value of the mean velocities of the down-flow at PL_1 and PL_2 , respectively.

also expected to be large when the intrusion length ξ is small. Thus, it seems appropriate to describe F_3 phenomenologically as

$$F_3 = -\frac{ke^{-\xi/\gamma}}{\bar{u}}. \quad (5.18)$$

where k is a positive constant. γ expresses the spatial range where the force works effectively. Eq. (5.18) is rewritten by using Eq. (5.4) as

$$F_3 = -ke^{-\xi/\gamma} \left(\frac{\pi a^2}{S} \right) \dot{x}^{-1}. \quad (5.19)$$

5.2 Description of flow-reversal process

5.2.1 Down- to up-flow

From Eqs. (5.8), (5.15), and (5.19), the equation of motion for a unit volume element located at the tip of the intrusion is given as

$$\begin{aligned} \rho_L \ddot{\xi} &= F_1 + F_2 + F_3 \\ &= \frac{\mu_H + \mu_L}{2a^2} \left(b_1 \frac{S}{\pi a^2} \dot{x} - b_2 \dot{\xi} \right) \\ &\quad + \left[-\frac{\rho_H g(x - x_{de})(1 + RD)}{d} + \delta \rho g \right] (1 - e^{-\xi/\alpha}) - ke^{-\xi/\gamma} \left(\frac{\pi a^2}{S} \right) \dot{x}^{-1}. \end{aligned} \quad (5.20)$$

It is noticed that there is an exception that ξ remains zero in the case of $F_1 + F_2 + F_3 < 0$ at $\xi = 0$. On the other hand, because the viscous damping regime is now considered, the temporal evolution of x exhibits an exponential response, expressed as in Eqs. (2.20) and (2.22): it is described as

$$x = C_d \exp \left[-\frac{(1 + DR)ga^4\pi\rho_H}{8Sd\mu_H}t \right] + x_{de}. \quad (5.21)$$

Here, we have assumed that the temporal evolution of x is not affected by an intrusion. This assumption is thought to be valid because it was found experimentally that the deviation from an exponential response at the flow-reversal process is sufficiently small compared with the amplitude of the oscillation, as shown in Fig. 4.1 (an exception will be shown in Sec. 6.3). Equation (5.21) is rewritten as

$$\dot{x} = -\frac{(1 + DR)ga^4\pi\rho_H}{8Sd\mu_H}(x - x_{de}). \quad (5.22)$$

By substituting Eq. (5.22) into Eq. (5.20), the temporal evolution of ξ is obtained as

$$\begin{aligned} \rho_L \ddot{\xi} = & \frac{\mu_H + \mu_L}{2} \left[-\frac{b_1 g \rho_H (1 + DR)}{8d\mu_H} (x - x_{de}) - \frac{b_2}{a^2} \dot{\xi} \right] \\ & + \left[-\frac{\rho_H (1 + RD)(x - x_{de})}{d} + \delta \rho g \right] (1 - e^{-\xi/\alpha}) \\ & + \frac{8kd\mu_H}{ga^2\rho_H(1 + DR)(x - x_{de})} e^{-\xi/\gamma}, \end{aligned} \quad (5.23)$$

and when ξ becomes equal to the pipe length d , the flow reverses completely. Thus, Eqs. (5.22) and (5.23) describe the behavior of the flow reversal from down- to up-flow.

5.2.2 Up- to down-flow

The flow reversal from up- to down-flow can be modelled in the same way as that of down- to up-flow, although the analysis becomes somewhat complicated because the decrease in the density of the heavy fluid due to inflow of the light fluid into the inner container should be taken into account. Here ξ is taken as the distance between the lower end of the pipe and the tip of the intrusion.

The viscous drag force F_1 and the effect of the acceleration of the fluid outside the pipe F_3 are derived in the same way as the case of the flow reversal from down- to up-flow. Thus, it is straightforward to obtain the following equations:

$$F_1 = \frac{\mu_H + \mu_L}{2a^2} \left(b_1 \frac{S}{\pi a^2} \dot{x} - b_2 \dot{\xi} \right) \quad (5.24)$$

$$F_3 = -ke^{-(d-\xi)/\gamma} \left(\frac{\pi a^2}{S} \right) \dot{x}^{-1}. \quad (5.25)$$

On the other hand, the derivation of the hydrostatic pressure gradient F_2 is somewhat complicated. Here, we assume that the density of the fluid that intrudes into a pipe is $\rho_H^{(i)}$, whereas the mean density of the fluid in the inner container depends on time, which is given as

$$\rho_H(t) = \rho_L + \frac{\delta\rho^{(i)}(x_d^{(i)} - d)}{x - d}. \quad (5.26)$$

This assumption is thought to be valid because the light fluid that has passed through the pipe accumulates above the heavy fluid in the inner container and hence the density of the fluid at the lower part of the inner container does not vary during the up-flow significantly. Thus, when the intrusion exists sufficiently at the interior of the pipe, F_2 is given in the following way by assuming that the gradient of the hydrostatic pressure is homogeneous inside the pipe:

$$F_2 = -\frac{P(d) - P(0)}{d} - \rho_H^{(i)} g. \quad (5.27)$$

If it is assumed that the hydrostatic pressure is simply derived by the height of the fluid surface, $P(d)$ and $P(0)$ are described in the same way as the case of the flow reversal from down- to up-flow as

$$P(d) = \rho_H(t)g(x - d), \quad (5.28)$$

$$P(0) = \rho_L gh. \quad (5.29)$$

By substituting Eqs. (5.12), (5.13), (5.26), (5.28) and (5.29) into Eq. (5.27), F_2 is derived as follows:

$$\begin{aligned} F_2 &= -\frac{[\rho_H^{(i)}(x_d^{(i)} - d) + \rho_L(x - x_d^{(i)})]g - \rho_L g[-R(x - x_{de}^{(i)}) + (\rho_H^{(i)}/\rho_L)x_{de}^{(i)}]}{d} - \rho_H^{(i)} g \\ &= -\frac{g}{d}[\rho_H^{(i)}(x_d^{(i)} - x_{de}^{(i)}) + \rho_L(x - x_d^{(i)}) + \rho_L R(x - x_{de}^{(i)})]. \end{aligned} \quad (5.30)$$

On the other hand, it is obvious that $F_2 = 0$ when there is no intrusion ($\xi = d$). Because F_2 is a continuous function of ξ , F_2 is phenomenologically described in the same as the flow reversal from down- to up-flow, that is,

$$F_2 = -\frac{g}{d}[\rho_H^{(i)}(x_d^{(i)} - x_{de}^{(i)}) + \rho_L(x - x_d^{(i)}) + \rho_L R(x - x_{de}^{(i)})](1 - e^{-(d-\xi)/\alpha}). \quad (5.31)$$

From Eqs. (5.24), (5.25) and (5.31), the equation of motion for a unit volume element located at the tip of the intrusion is obtained as follows:

$$\begin{aligned} \rho_H^{(i)} \ddot{\xi} &= F_1 + F_2 + F_3 \\ &= \frac{\mu_H + \mu_L}{2a^2} \left[b_1 \left(\frac{S}{\pi a^2} \right) \dot{x} - b_2 \dot{\xi} \right] \\ &\quad - \frac{g}{d}[\rho_H^{(i)}(x_d^{(i)} - x_{de}^{(i)}) + \rho_L(x - x_d^{(i)}) + \rho_L R(x - x_{de}^{(i)})](1 - e^{-(d-\xi)/\alpha}) \\ &\quad - k e^{-(d-\xi)/\gamma} \left(\frac{\pi a^2}{S} \right) \dot{x}^{-1}. \end{aligned} \quad (5.32)$$

Because the viscous damping regime is now considered, the temporal evolution of x exhibits an exponential response under the assumption that it is not affected by an intrusion. As shown in Eqs. (2.19) and (2.21), x is described as

$$x = C_u \exp \left[-\frac{(1+R)ga^4\pi\rho_L}{8Sd\mu_L} t \right] + x_{ue}^{(i)}, \quad (5.33)$$

with

$$x_{ue}^{(i)} = x_{de}^{(i)} + \frac{\delta\rho^{(i)}d}{(1+R)\rho_L} \quad (5.34)$$

From Eqs. (5.33) and (5.34), the temporal evolution of x is described as

$$\dot{x} = -\frac{(1+R)ga^4\pi\rho_L}{8Sd\mu_L} \left[x - x_{de}^{(i)} - \frac{\delta\rho^{(i)}d}{(1+R)\rho_L} \right]. \quad (5.35)$$

By substituting Eq. (5.35) into Eq. (5.32), the temporal evolution of ξ is derived in the following way:

$$\begin{aligned} \rho_H^{(i)} \ddot{\xi} &= \frac{\mu_H + \mu_L}{2} \left[-\frac{b_1 g \rho_L (1+R)}{8d\mu_L} \left(x - x_{de}^{(i)} - \frac{\delta\rho^{(i)}d}{(1+R)\rho_L} \right) - \frac{b_2}{a^2} \dot{\xi} \right] \\ &\quad - \frac{g}{d} [\rho_H^{(i)} (x_d^{(i)} - x_{de}^{(i)}) + \rho_L (x - x_d^{(i)}) + \rho_L R (x - x_{de}^{(i)})] (1 - e^{-(d-\xi)/\alpha}) \\ &\quad + \frac{8kd\mu_L}{ga^2\rho_L(1+R)[x - x_{de}^{(i)} - \delta\rho^{(i)}d/((1+R)\rho_L)]} e^{-(d-\xi)/\gamma}, \end{aligned} \quad (5.36)$$

and when the intrusion reaches the lower end of the pipe ($\xi = 0$), the flow reverses completely. In this way, Eqs. (5.35) and (5.36) describe the behavior of the flow reversal from up- to down-flow.

5.2.3 Non-dimensionalized model

I have derived the model describing whole oscillatory process including the flow reversal by using two variables, x and ξ (Eqs. (5.22) and (5.23) from down- to up-flow, and (5.35), and (5.36) for up- to down-flow). This model can be simplified by describing it in the non-dimensionalized form. Indeed, Eqs. (5.22), (5.23), (5.35), and (5.36) are written as

$$\phi^{-1} \frac{d\hat{x}}{d\hat{t}} = -\frac{\hat{x}}{\hat{\mu}_H}, \quad (5.37)$$

$$\begin{aligned} \epsilon \frac{d\hat{\xi}}{d\hat{t}} &= -C_1 \frac{\hat{x}}{\hat{\mu}_H} + C_2 \frac{1-\hat{x}}{\hat{\mu}_I} (1 - e^{-\hat{\xi}/\alpha'}) \\ &\quad + C_3 \frac{\hat{\mu}_H e^{-\hat{\xi}/\gamma'}}{\hat{\mu}_I \hat{x}} - \frac{C_4}{\hat{\mu}_I} \frac{d^2\hat{\xi}}{d\hat{t}^2}, \end{aligned} \quad (5.38)$$

$$\phi^{-1} \frac{d\hat{x}}{d\hat{t}} = \frac{1-\psi\hat{x}}{\hat{\mu}_L}, \quad (5.39)$$

$$\epsilon \frac{d\hat{\xi}}{d\hat{t}} = C_1 \frac{1-\psi\hat{x}}{\hat{\mu}_L} - C_2 \frac{\psi\hat{x} + (x_d - x_{de})/d}{\hat{\mu}_I} (1 - e^{-(\epsilon^{-1}-\hat{\xi})/\alpha'})$$

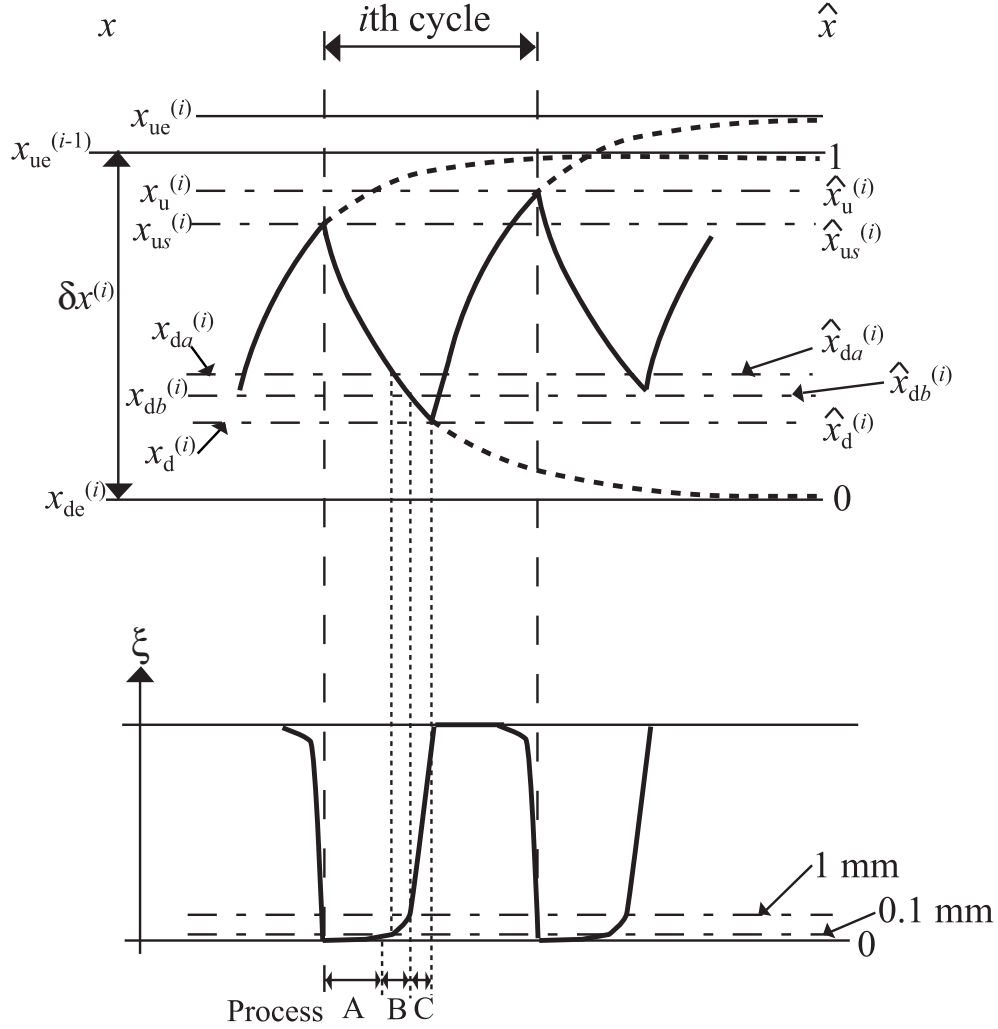


Figure 5.5: Definitions of parameters. The parameters with dimension are shown in the left side, while non-dimensionalized parameters are shown in the right side. Upper picture is the scheme of the temporal evolution of the height of heavy fluid surface, while lower picture is that of the intrusion length ξ . $x_u^{(i)}$, $x_{us}^{(i)}$ and $x_d^{(i)}$ are the heights of the heavy fluid surface when the flow reverses from i th up- to $(i+1)$ th down-flow, from $(i-1)$ th up- to i th down-flow, and i th down- to i th up-flow, respectively. x_{da} and x_{db} are the heights of the heavy fluid surface when the intrusion length becomes 0.1 mm and 1 mm, respectively. $x_{ue}^{(i)}$ and $x_{de}^{(i)}$ are the heights at the hydrostatic equilibria where a pipe is filled with light and heavy fluids at i th cycle, respectively, and $\delta x^{(i)}$ is the difference between the $x_{ue}^{(i-1)}$ and $x_{de}^{(i)}$. Non-dimensionalized variables are normalized by $\delta x^{(i)}$, and thus $\hat{x} = 0$ and 1 correspond to the $x_{ue}^{(i-1)}$ and $x_{de}^{(i)}$ in the dimensional form, respectively. $\hat{x}_u^{(i)}$, $\hat{x}_{us}^{(i)}$, $\hat{x}_d^{(i)}$, $\hat{x}_{da}^{(i)}$ and $\hat{x}_{db}^{(i)}$ correspond to $x_u^{(i)}$, $x_{us}^{(i)}$, $x_d^{(i)}$, $x_{da}^{(i)}$ and $x_{db}^{(i)}$ in the dimensional form, respectively. Processes A, B, and C denote the processes where the fluid flows one-way ($\xi = 0$), where an intrusion grows slowly, and where an intrusion grows rapidly, respectively.

$$-C_3 \frac{\hat{\mu}_L}{\hat{\mu}_1} \frac{e^{-(\epsilon^{-1}-\hat{\xi})/\gamma'}}{1-\psi\hat{x}} - \frac{C_4}{\hat{\mu}_1 D} \frac{d^2 \hat{\xi}}{d\hat{t}^2}, \quad (5.40)$$

where $\epsilon = a/d \ll 1$, $\hat{\xi} = \xi/a$, $\hat{t} = \eta\epsilon t$, $\eta = 2\zeta\mu_W\rho_H^{(i)}/(a^2\rho_L^2)$, $\zeta = ga^5\pi\rho_L^2/(16S\mu_W^2)$, $\hat{\mu}_H = \mu_H/\mu_W$, $\hat{\mu}_L = \mu_L/\mu_W$, $\hat{\mu}_1 = \mu_1/\mu_W = (\mu_H + \mu_L)/(2\mu_W)$, $\alpha' = \alpha/a$, $\gamma' = \gamma/a$, $\phi = 1 + DR$, and $\psi = D(1 + R)/(1 + DR)$, with μ_W the viscosity of water at 25.0 °C, 0.89×10^{-3} Pa · s. C_1 , C_2 , C_3 , and C_4 are given as

$$C_1 = \frac{b_1 \delta \rho S}{b_2 \rho_H a^2 \pi}, \quad (5.41)$$

$$C_2 = \frac{8S\delta\rho}{b_2 \rho_H a^2 \pi}, \quad (5.42)$$

$$C_3 = \frac{64kS\mu_W}{b_2 \delta \rho g^2 \rho_H a^4 \pi}, \quad (5.43)$$

$$C_4 = \frac{a^7 \rho_L \rho_H \pi g}{8b_2 S \mu_W^2 d^2}. \quad (5.44)$$

\hat{x} is defined as $\hat{x} = (x - x_{de})/\delta x$, where $\delta x^{(i)} = \delta\rho^{(i)}d/(\rho_H^{(i)} + \rho_L R)$ is the difference between the two hydrostatic equilibrium, as shown in Eq. (2.42). Hence, $\hat{x} = 0$ and 1 correspond to the hydrostatic equilibrium where a pipe is filled with the heavy and light fluid, respectively (see Fig. 5.5).

Here, the term $(x_d - x_{de})/d$ in Eq. (5.40) is neglected, because $x_d - x_{de}$ is thought to be much smaller than the pipe length d . In addition, the last terms in the right hand sides of Eqs. (5.38) and (5.40) are neglected, which is understood from the following consideration. Now we compare the contributions of the second and last terms in the right hand sides of Eqs. (5.38) and (5.40). From Eqs. (5.42) and (5.44), we find that the ratio of C_4 to C_2 is given as

$$\frac{C_4}{C_2} = \frac{a^9 \pi^2 \rho_H^2 \rho_L g}{64 S^2 \delta \rho \mu_W^2 d^2} = (\beta \sigma^{1/2})^2 \cdot \frac{\mu_L^2}{\mu_W^2} \cdot \frac{3\epsilon}{8\sigma^2 D^2}, \quad (5.45)$$

where $\beta^2 = ga^6\pi\rho_L^2/(16S\mu_L^2d)$ and $\sigma = 3S\delta\rho^{(i)}/(2a^2\pi\rho_L)$. As described in Sec. 2.1, $\beta\sigma^{1/2} \ll 1$ is satisfied in the viscous damping regime and $\sigma > 3/2$ should be satisfied so that an oscillation occur. Moreover, D and μ_L^2/μ_W^2 are usually not extremely larger than unity, and we now consider the case of $\epsilon \ll 1$. Hence, we can confirm that $C_4/C_2 \ll 1$ from Eq. (5.45), and thus the contributions of the last terms in the right hand sides of Eqs. (5.38) and (5.40) are considered to be negligible compared with those of the second terms.

Thus, the non-dimensionalized model is described in the following way: The behavior during the down-flow is described as

$$\phi^{-1} \frac{d\hat{x}}{d\hat{t}} = -\frac{\hat{x}}{\hat{\mu}_H}, \quad (5.46)$$

$$\epsilon \frac{d\hat{\xi}}{d\hat{t}} = -C_1 \frac{\hat{x}}{\hat{\mu}_H} + C_2 \frac{1-\hat{x}}{\hat{\mu}_I} (1 - e^{-\hat{\xi}/\alpha'}) + C_3 \frac{\hat{\mu}_H}{\hat{\mu}_I} \frac{e^{-\hat{\xi}/\gamma'}}{\hat{x}}, \quad (5.47)$$

and the flow reverses at $\hat{\xi} = \epsilon^{-1}$, which corresponds to $\xi = d$. On the other hand, the behavior during the up-flow is described as

$$\phi^{-1} \frac{d\hat{x}}{d\hat{t}} = \frac{1 - \psi\hat{x}}{\hat{\mu}_L}, \quad (5.48)$$

$$\epsilon \frac{d\hat{\xi}}{d\hat{t}} = C_1 \frac{1 - \psi\hat{x}}{\hat{\mu}_L} - C_2 \frac{\psi\hat{x}}{\hat{\mu}_I} (1 - e^{-(\epsilon^{-1}-\hat{\xi})/\alpha'}) - C_3 \frac{\hat{\mu}_L}{\hat{\mu}_I} \frac{e^{-(\epsilon^{-1}-\hat{\xi})/\gamma'}}{1 - \psi\hat{x}}, \quad (5.49)$$

and the flow reverses at $\hat{\xi} = 0$. Equations (5.46)-(5.49) are considered to be the fundamental equations describing the whole oscillatory behavior including the flow reversal processes.

5.3 Simulations

In order to confirm the validity of the model derived in the previous section, numerical simulations are performed. Figures 5.6-5.8 show the temporal evolutions of the height of the heavy fluid surface \hat{x} and the intrusion length $\hat{\xi}$, which are obtained by simulating Eqs. (5.46)-(5.49). The parameters C_1 , C_2 , C_3 , α' , and γ' are chosen so that the experimental results are well reproduced. Although the density of the heavy fluid $\rho_H(t)$ decreases as the number of cycles increases in the actual system, it is assumed that $\rho_H(t)$ is reset to a finite value at the beginning of the cycle, for simplicity. Runge-Kutta method is used, and the time step is set at 0.0005.

Figure 5.6 shows the case where the viscosities of the two fluids are identical. As is expected, the temporal evolution of \hat{x} shows an exponential response for each up- and down-flow. On the other hand, $\hat{\xi}$ is found to behave in the following way: During the down-flow, $\hat{\xi}$ remains zero when the value of \hat{x} is large (process A). As \hat{x} decreases, $\hat{\xi}$ begins to increase gradually (process B). When $\hat{\xi}$ exceeds a certain threshold, it suddenly begins to increase rapidly (process C). Then, when the intrusion reaches the upper end of the pipe, *i.e.*, $\hat{\xi}$ becomes ϵ^{-1} , the flow reverses. On the other hand, during the up-flow, $\hat{\xi}$ remains ϵ^{-1} for small \hat{x} (process A), and begins to decrease gradually as \hat{x} increases (process B). When the intrusion length exceeds a threshold, $\hat{\xi}$ begins to decrease rapidly, and the flow reverses when the intrusion reaches the lower end of the pipe ($\hat{\xi} = 0$). Thus, the three processes found in the experiments are well reproduced by the simulation.

Figure 5.7 shows the case where the viscosity of the heavy fluid is extremely larger than that of the light fluid. As is expected, the time constant of the exponential curve of \hat{x} is larger in the down-flow than in the up-flow. The temporal evolution of $\hat{\xi}$ is also much affected by the viscosity. For the flow reversal from down- to up-flow, the processes

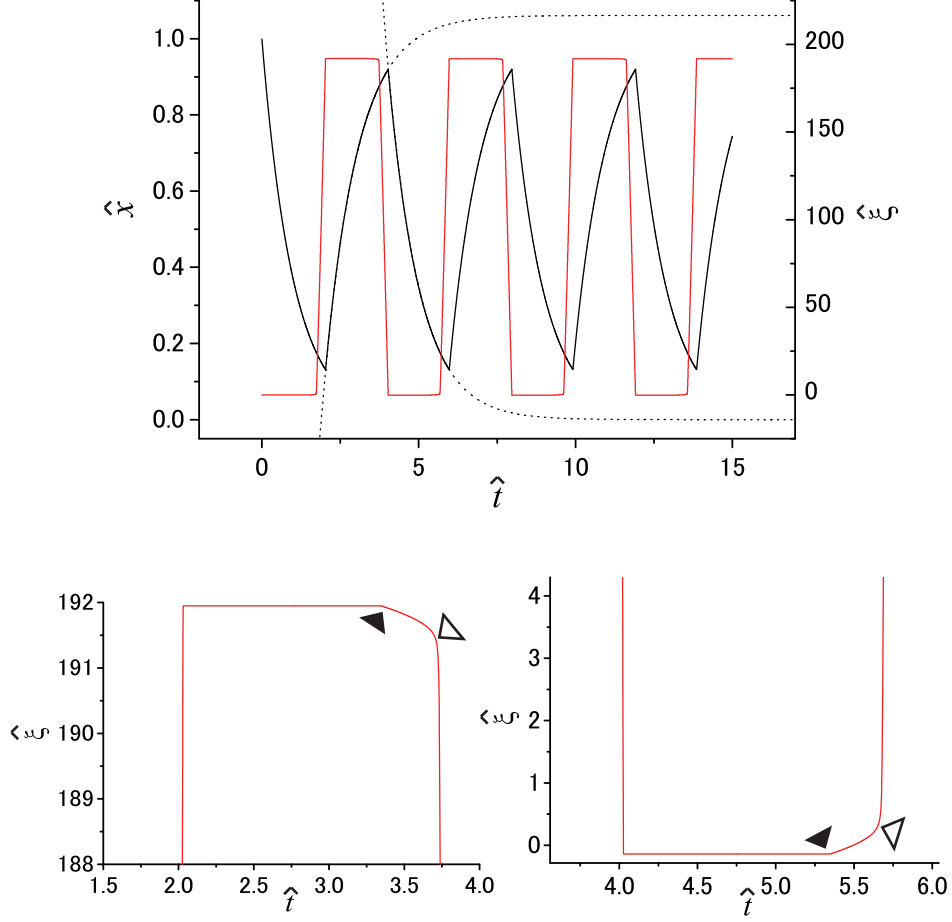


Figure 5.6: The temporal evolutions of the height of the heavy fluid surface \hat{x} (black solid line) and the intrusion length $\hat{\xi}$ (red solid line) simulated from Eqs. (5.46)-(5.49) in the case of $\mu_H = 0.89 \times 10^{-3} \text{ Pa} \cdot \text{s}$ and $\mu_L = 0.89 \times 10^{-3} \text{ Pa} \cdot \text{s}$. The oscillatory behavior is well reproduced. The temporal evolution of \hat{x} exhibits an exponential response (black dotted line). Before the flow reverses from down-(up-) to up-(down-)flow, $\hat{\xi}$ begins to increase(decrease) rapidly. Lower graphs show the magnified views of the temporal evolution of $\hat{\xi}$. It is clearly seen that the intrusion grows gradually before the onset of its rapid growth occurs. The onsets of the gradual growth and rapid growth are shown by filled and empty arrowheads, respectively. The parameters of the simulation are as follows: $2a = 0.73 \text{ mm}$, $d = 70 \text{ mm}$, $\rho_H = 1.057 \times 10^3 \text{ kg m}^{-3}$, $\rho_L = 0.996 \times 10^3 \text{ kg m}^{-3}$, $S = 7.70 \times 10^{-4} \text{ m}^2$, $R = 1.44 \times 10^{-4}$, $b_1 = 10.7$, $b_2 = 160$, $k = 0.40 \text{ kg m}^{-1} \text{s}^{-3}$, $C_1=7.11$, $C_2=5.31$, $C_3=0.32$, $\alpha'=1.82$, and $\gamma'=0.30$.

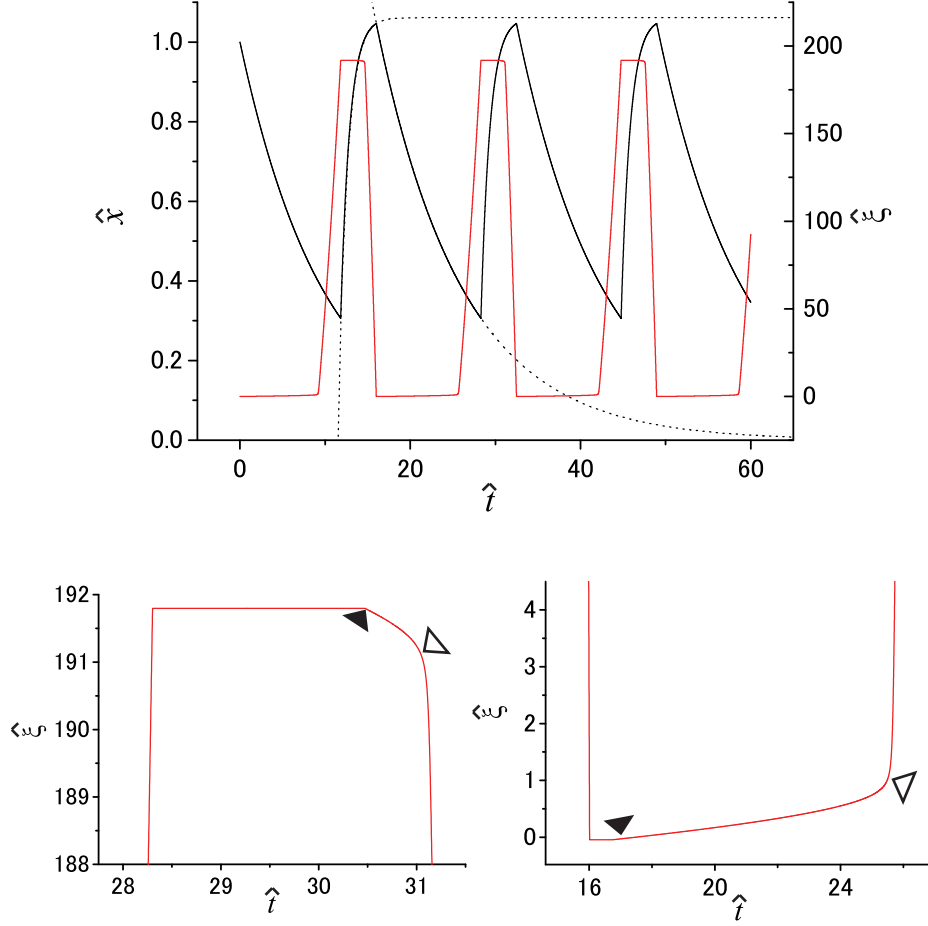


Figure 5.7: The temporal evolutions of the height of the heavy fluid surface \hat{x} (black solid line) and the intrusion length $\hat{\xi}$ (red solid line) simulated from Eqs. (5.46)-(5.49) in the case of $\mu_H = 8.90 \times 10^{-3} \text{ Pa} \cdot \text{s}$ and $\mu_L = 0.89 \times 10^{-3} \text{ Pa} \cdot \text{s}$. The oscillatory behavior is well reproduced. The temporal evolution of \hat{x} exhibits an exponential response (black dotted line). Before the flow reverses from down-(up-) to up-(down-)flow, $\hat{\xi}$ begins to increase(decrease) rapidly. Lower graphs show the magnified views of the temporal evolution of $\hat{\xi}$. It is clearly seen that the intrusion grows gradually before the onset of its rapid growth occurs. The onsets of the gradual growth and rapid growth are shown by filled and empty arrowheads, respectively. The parameters of the simulation are as follows: $2a = 0.73 \text{ mm}$, $d = 70 \text{ mm}$, $\rho_H = 1.057 \times 10^3 \text{ kg m}^{-3}$, $\rho_L = 0.996 \times 10^3 \text{ kg m}^{-3}$, $S = 7.70 \times 10^{-4} \text{ m}^2$, $R = 1.44 \times 10^{-4}$, $b_1 = 10.7$, $b_2 = 160$, $k = 0.40 \text{ kg m}^{-1} \text{s}^{-3}$, $C_1=7.11$, $C_2=5.31$, $C_3=0.32$, $\alpha'=1.82$, and $\gamma'=0.30$.

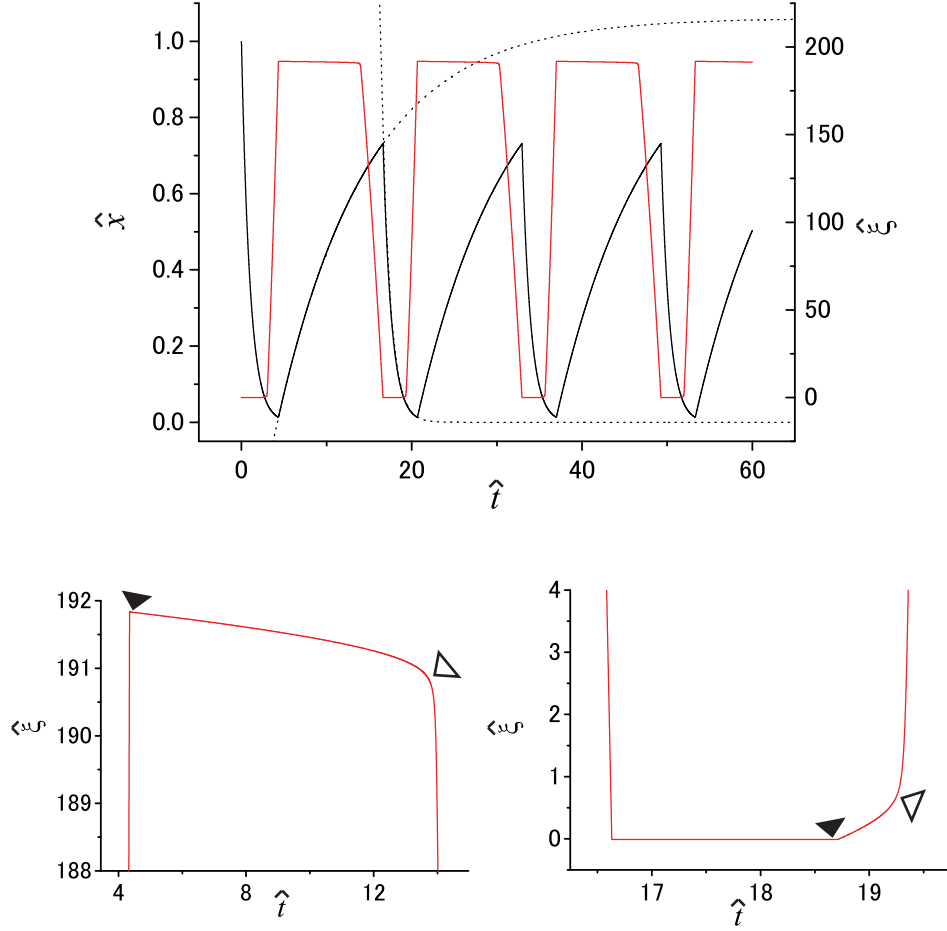


Figure 5.8: The temporal evolutions of the height of the heavy fluid surface \hat{x} (black solid line) and the intrusion length $\hat{\xi}$ (red solid line) simulated from Eqs. (5.46)-(5.49) in the case of $\mu_H = 0.89 \times 10^{-3} \text{ Pa} \cdot \text{s}$ and $\mu_L = 8.90 \times 10^{-3} \text{ Pa} \cdot \text{s}$. The oscillatory behavior is well reproduced. The temporal evolution of \hat{x} exhibits an exponential response (black dotted line). Before the flow reverses from down-(up-) to up-(down-)flow, $\hat{\xi}$ begins to increase(decrease) rapidly. Lower graphs show the magnified views of the temporal evolution of $\hat{\xi}$. It is clearly seen that the intrusion grows gradually before the onset of its rapid growth occurs. The onsets of the gradual growth and rapid growth are shown by filled and empty arrowheads, respectively. The parameters of the simulation are as follows: $2a = 0.73 \text{ mm}$, $d = 70 \text{ mm}$, $\rho_H = 1.057 \times 10^3 \text{ kg m}^{-3}$, $\rho_L = 0.996 \times 10^3 \text{ kg m}^{-3}$, $S = 7.70 \times 10^{-4} \text{ m}^2$, $R = 1.44 \times 10^{-4}$, $b_1 = 10.7$, $b_2 = 160$, $k = 0.40 \text{ kg m}^{-1} \text{s}^{-3}$, $C_1=7.11$, $C_2=5.31$, $C_3=0.32$, $\alpha'=1.82$, and $\gamma'=0.30$.

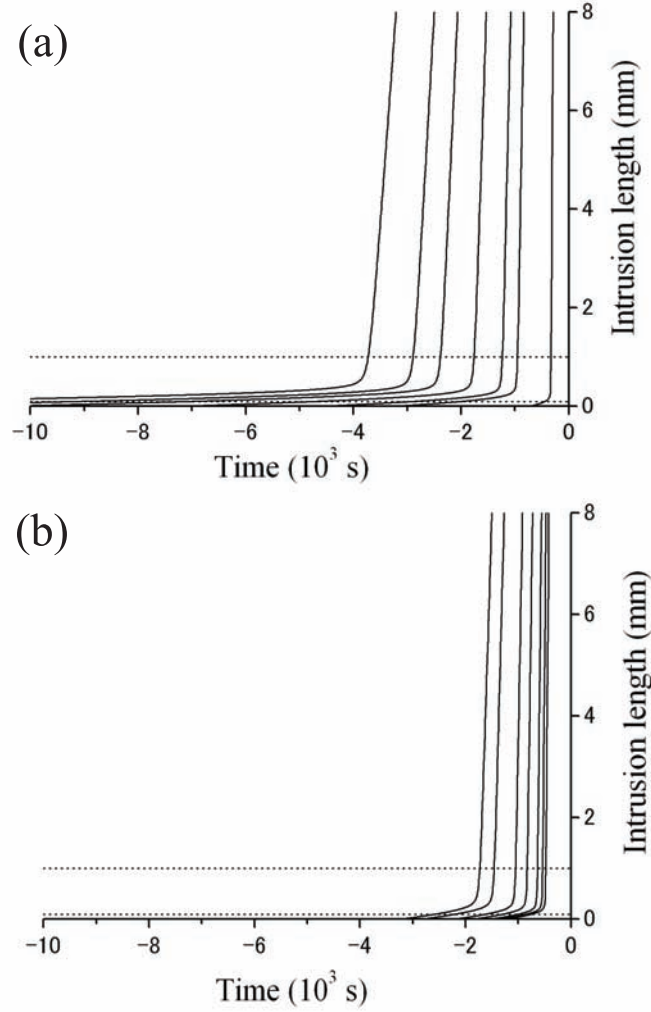


Figure 5.9: The viscosity-dependent temporal evolution of the intrusion of light fluid calculated from Eqs. (5.46) and (5.47). (a) μ_H is varied while μ_L is fixed at 0.89×10^{-3} Pa·s. Each curve corresponds to $\mu_H = 1.77, 5.11, 6.53, 9.06, 11.96, 14.30$, and 18.02 ($\times 10^{-3}$ Pa·s) from right to left, respectively. (b) μ_L is varied while μ_H is fixed at 2.63×10^{-3} Pa·s. Each curve corresponds to $\mu_L = 0.89, 1.47, 2.43, 4.36, 6.67, 11.05$, and 14.18 ($\times 10^{-3}$ Pa·s) from right to left, respectively. The dotted lines denote 0.1 mm and 1 mm of intrusion length. The parameters of the simulation are as follows: $a = 0.365$ mm, $d = 70$ mm, $\rho_H = 1.057 \times 10^3$ kg m $^{-3}$, $\rho_L = 0.996 \times 10^3$ kg m $^{-3}$, $S = 7.70 \times 10^{-4}$ m 2 , $R = 1.44 \times 10^{-4}$, $b_1 = 10.7$, $b_2 = 160$, $k = 0.40$ kg m $^{-1}$ s $^{-3}$, $C_1=7.11$, $C_2=5.31$, $C_3=0.32$, $\alpha'=1.82$, and $\gamma'=0.30$.

B and C begin even when \hat{x} is still large, and hence the flow reverses for relatively large \hat{x} compared with the case shown in Fig. 5.6. On the contrary, for the flow reversal from up- to down-flow, the processes B and C do not begin until the value of \hat{x} becomes close to the asymptotic value of the exponential curve, and as a consequence the flow reverses for relatively large \hat{x} compared with the case shown in Fig. 5.6.

The case where the viscosity of the light fluid is extremely larger than that of the heavy fluid is shown in Fig. 5.8. Obviously, the opposite trend to Fig. 5.7 is shown: The time constant of the exponential curve of \hat{x} is larger in the up-flow than the down-flow. For the flow reversal from down- to up-flow, the processes B and C do not begin until the value of \hat{x} becomes close to the asymptotic value of the exponential curve, and as a consequence the flow reverses for relatively small \hat{x} . For the flow reversal up- to down-flow, the processes B and C begin even when \hat{x} is still small, and hence the flow reverses for relatively small \hat{x} .

Figure 5.9(a) shows the viscosity dependence of the temporal evolution of ξ at the flow reversal from down- to up-flow, which is obtained by solving Eqs. (5.46) and (5.47). In this figure, t is redefined so that its origin agrees with the time when the intrusion reaches the upper end of the pipe, $\xi = 70$ mm, which corresponds to the moment when the flow reverses completely. When μ_H is increased while μ_L is kept constant, the intrusion of the light fluid tends to last for an extremely long time before the flow reversal occurs and the growth rate in the process C becomes relatively small, as shown in Fig. 5.9(a), which is in good agreement with the experimental result (Fig. 4.8(a)). In the same way as the experiment, we have defined the parameters \hat{x}_{da} and \hat{x}_{db} as the values of \hat{x} when the intrusion length ξ becomes 0.1 mm and 1 mm, corresponding to $\hat{\xi} = 0.27$ and 2.74, which characterize the timings for the beginning of the intrusion and the onset of its rapid growth, respectively. In addition, we have defined \hat{x}_d as the value of \hat{x} when ξ becomes 70 mm, corresponding to $\hat{\xi} = 191.78$, which characterizes the timing for the flow reversal. Then, the parameters \hat{x}_{da} , \hat{x}_{db} and \hat{x}_d are compared with the experimental parameters s_{da} , s_{db} and s_d . As shown in Fig. 4.7(a), \hat{x}_{da} , \hat{x}_{db} , and \hat{x}_d are surprisingly in good agreement with s_{da} , s_{db} , and s_d .

On the other hand, when μ_L is increased while μ_H is kept constant, \hat{x}_{da} , \hat{x}_{db} , and \hat{x}_d decrease as μ_L increases, and their values are generally consistent with the experimental results, as shown in Fig. 4.7(b). However, the values of \hat{x}_{da} , \hat{x}_{db} , and \hat{x}_d for large μ_L are slightly lower than s_{da} , s_{db} , and s_d , respectively. Further, the growth rate of the intrusion is generally slower for large μ_L in the simulation (Fig. 5.9(b)) than that in the experiment (Fig. 4.8(b)).

The flow reversal from up- to down-flow is also simulated by using Eqs. (5.48) and (5.49), and compared with the experimental result. Here, the experimental parameter

s_u should be compared with the value of \hat{x} when the flow reverses from $(i-1)$ th up- to i th down-flow, which we denote as $\hat{x}_{us}^{(i)}$ (see Fig.5.5). However, $\hat{x}_{us}^{(i)}$ cannot be obtained directly from the simulation. Hence, it is derived in the following way. Let $\hat{x}_u^{(i)}$ be defined as the value of \hat{x} when the flow reverses from i th up- to $(i+1)$ th down-flow (see Fig.5.5). Notice that $\hat{x}_u^{(i)}$ is obtained directly from the simulation, because it corresponds to the value of \hat{x} when ξ becomes 0 mm for the i th up-flow. Then, by assuming that the relation $x_u^{(i)} - x_u^{(i-1)} \approx x_{ue}^{(i)} - x_{ue}^{(i-1)}$ holds (see Fig. 5.5), the difference between $\hat{x}_u^{(i)}$ and $\hat{x}_{us}^{(i)}$ is derived as

$$\begin{aligned}\hat{x}_u^{(i)} - \hat{x}_{us}^{(i)} &= \frac{x_u^{(i)} - x_{us}^{(i)}}{\delta x^{(i)}} \\ &\approx \frac{x_{ue}^{(i)} - x_{ue}^{(i-1)}}{\delta x^{(i)}} \\ &= \frac{x_{ue}^{(i)} - x_{de}^{(i)}}{\delta x^{(i)}} - 1.\end{aligned}\quad (5.50)$$

On the other hand, as we have shown in Chap. 2, $x_{ue}^{(i)} - x_{de}^{(i)}$ and $\delta x^{(i)}$ are described as

$$x_{ue}^{(i)} - x_{de}^{(i)} = \frac{\delta \rho^{(i)} d}{D(1+R)\rho_H^{(i)}}, \quad (5.51)$$

$$\delta x^{(i)} = \frac{\delta \rho^{(i)} d}{(1+DR)\rho_H^{(i)}}. \quad (5.52)$$

By substituting Eqs. (5.51) and (5.52) into Eq. (5.50), $\hat{x}_{us}^{(i)}$ is obtained as follows:

$$\hat{x}_{us} = \hat{x}_u + 1 - \frac{1}{\psi}. \quad (5.53)$$

Thus, \hat{x}_{us} can be calculated from $\hat{x}_u^{(i)}$. In Fig. 4.7, \hat{x}_{us} is compared with the experimental value s_u . It is found that \hat{x}_{us} is qualitatively in good agreement with s_u , although \hat{x}_{us} is slightly larger than s_u for $\mu_H > \mu_L$.

In this way, the flow-reversal process is generally reproduced by the model, although not completely. Especially, the behaviors of the slow (process B) and rapid (process C) growth of an intrusion are well reproduced. Indeed, this behavior is easily understandable by the following considerations. Let $f(\hat{\xi})$ be defined as the right hand side of Eq. (5.47). Because \hat{x} is a slowly varying variable compared with $\hat{\xi}$ with respect to time, which can be deduced from Eqs. (5.46) and (5.47), \hat{x} is regarded as a parameter characterizing the functional form of $f(\hat{\xi})$. Figure 5.10 shows the \hat{x} -dependence of $f(\hat{\xi})$, where the functional forms of $F'_1 \equiv -C_1/\hat{\mu}_H \hat{x}$, $F'_2 \equiv C_2/\hat{\mu}_I \cdot (1 - \hat{x})(1 - e^{-\hat{\xi}/\alpha'})$, and $F'_3 \equiv C_3 \hat{\mu}_H/\hat{\mu}_I \cdot e^{-\hat{\xi}/\gamma'}/\hat{x}$, are also shown. Notice that F'_1 , F'_2 , and F'_3 are originated from the viscous drag force due to the flow, the hydrostatic pressure gradient, and the effect of the acceleration of the fluid that has passed through the pipe, respectively. When the value of \hat{x} is large, the

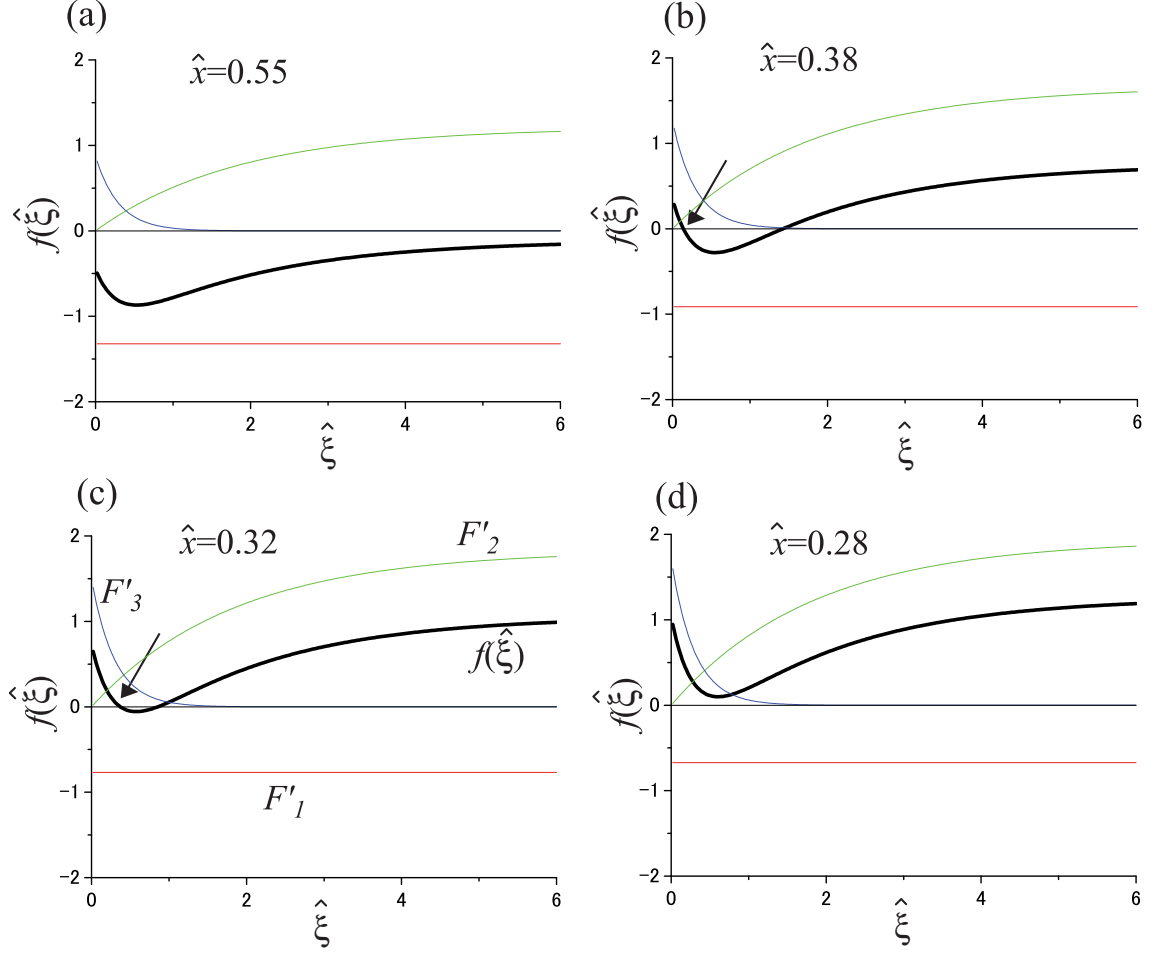


Figure 5.10: The functional form of $f(\hat{\xi})$ (bold black line), F'_1 (red solid line), F'_2 (green solid line), and F'_3 (blue solid line) in the case of $\hat{\mu}_H=2.96$ and $\hat{\mu}_L=1.00$. The value of \hat{x} is varied: (a) $\hat{x}=0.55$, (b) $\hat{x}=0.38$, (c) $\hat{x}=0.32$, and (d) $\hat{x}=0.28$. The arrows denote the stable solution of Eq. (5.47), $\hat{\xi} = \hat{\xi}_0$. The parameters of the simulation are as follows: $a = 0.365$ mm, $d = 70$ mm, $\rho_H = 1.057 \times 10^3$ kg m $^{-3}$, $\rho_L = 0.996 \times 10^3$ kg m $^{-3}$, $S = 7.70 \times 10^{-4}$ m 2 , $R = 1.44 \times 10^{-4}$, $b_1 = 10.7$, $b_2 = 160$, $k = 0.40$ kg m $^{-1}$ s $^{-3}$, $C_1=7.11$, $C_2=5.31$, $C_3=0.32$, $\alpha'=1.82$, and $\gamma'=0.30$.

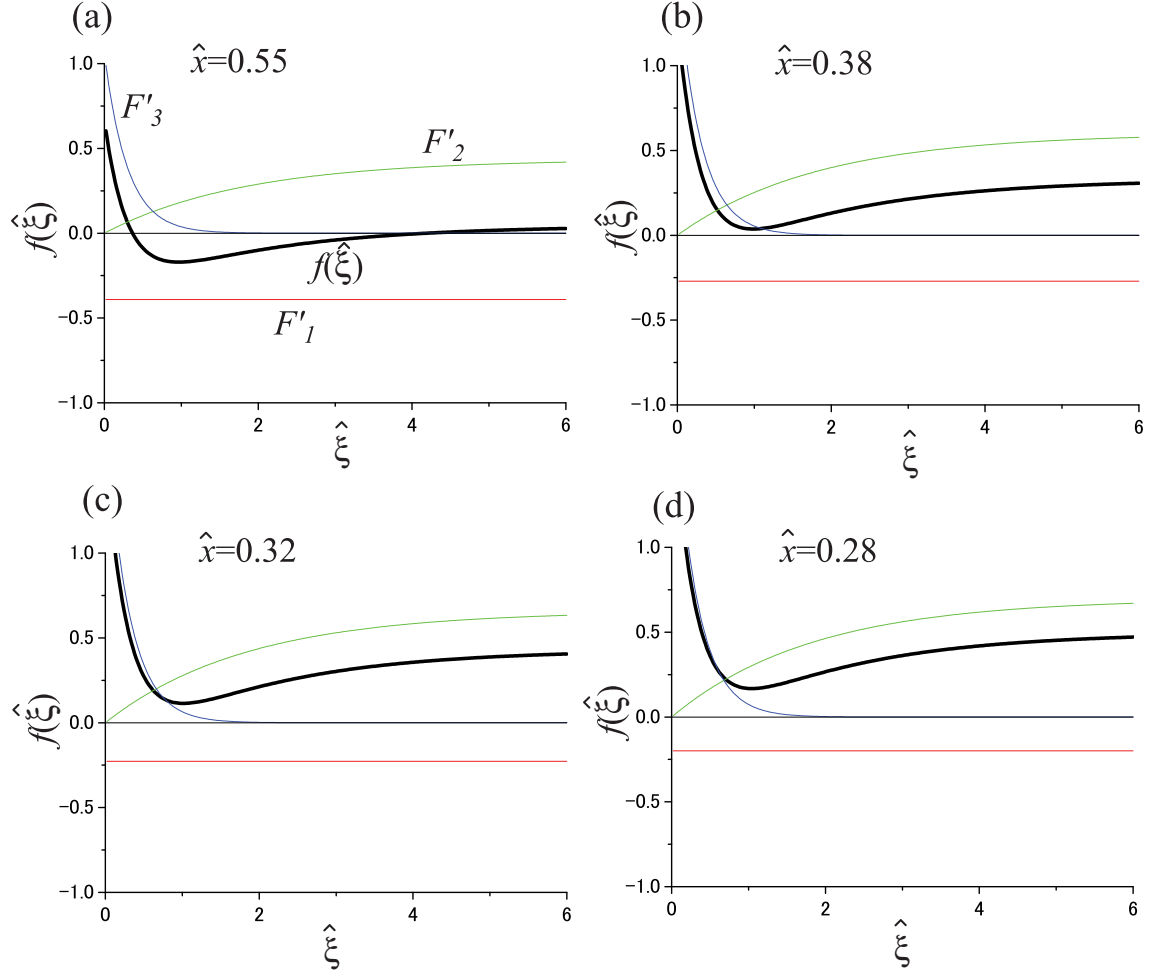


Figure 5.11: The functional form of $f(\hat{\xi})$ (bold black line), F'_1 (red solid line), F'_2 (green solid line), and F'_3 (blue solid line) in the case of $\hat{\mu}_H=10.00$ and $\hat{\mu}_L=1.00$. The value of \hat{x} is varied: (a) $\hat{x}= 0.55$, (b) $\hat{x}= 0.38$, (c) $\hat{x}= 0.32$, and (d) $\hat{x}= 0.28$. The arrows denote the stable solution of Eq. (5.47), $\hat{\xi} = \hat{\xi}_0$. The parameters of the simulation are as follows: $a = 0.365$ mm, $d = 70$ mm, $\rho_H = 1.057 \times 10^3$ kg m $^{-3}$, $\rho_L = 0.996 \times 10^3$ kg m $^{-3}$, $S = 7.70 \times 10^{-4}$ m 2 , $R = 1.44 \times 10^{-4}$, $b_1 = 10.7$, $b_2 = 160$, $k = 0.40$ kg m $^{-1}$ s $^{-3}$, $C_1=7.11$, $C_2=5.31$, $C_3=0.32$, $\alpha'=1.82$, and $\gamma'=0.30$.

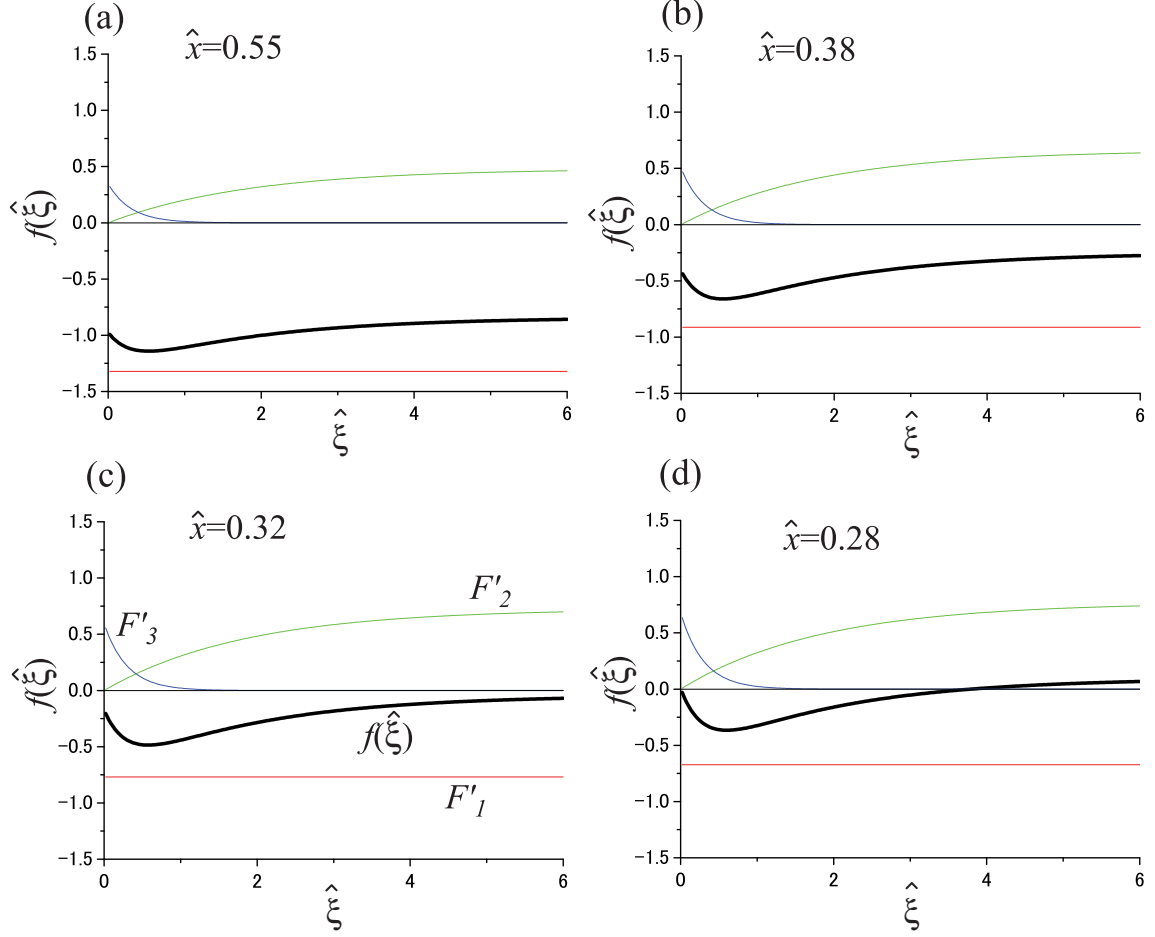


Figure 5.12: The functional form of $f(\hat{\xi})$ (bold black line), F'_1 (red solid line), F'_2 (green solid line), and F'_3 (blue solid line) in the case of $\hat{\mu}_H=2.96$ and $\hat{\mu}_L=7.00$. The value of \hat{x} is varied: (a) $\hat{x}=0.55$, (b) $\hat{x}=0.38$, (c) $\hat{x}=0.32$, and (d) $\hat{x}=0.28$. The arrows denote the stable solution of Eq. (5.47), $\hat{\xi} = \hat{\xi}_0$. The parameters of the simulation are as follows: $a = 0.365$ mm, $d = 70$ mm, $\rho_H = 1.057 \times 10^3$ kg m $^{-3}$, $\rho_L = 0.996 \times 10^3$ kg m $^{-3}$, $S = 7.70 \times 10^{-4}$ m 2 , $R = 1.44 \times 10^{-4}$, $b_1 = 10.7$, $b_2 = 160$, $k = 0.40$ kg m $^{-1}$ s $^{-3}$, $C_1=7.11$, $C_2=5.31$, $C_3=0.32$, $\alpha'=1.82$, and $\gamma'=0.30$.

intrusion does not occur and $\hat{\xi}$ remains zero, because the relation $f(0) \leq 0$ clearly holds owing to the large contribution of F'_1 (process A) (Fig. 5.10(a)). However, when \hat{x} is decreased, $f(0)$ becomes positive, because the contribution of F'_3 becomes large and also because the contribution of F'_1 decreases while that of F'_2 increases. Then, the relation $f(\hat{\xi}) = 0$ leads to a positive solution $\hat{\xi}_0$ with $f'(\hat{\xi}_0) < 0$; hence, $\hat{\xi} = \hat{\xi}_0$ becomes a stable solution of Eq. (5.47). Thus, the light fluid begins to intrude into a pipe (process B) (Fig. 5.10(b)). As \hat{x} decreases much more, $\hat{\xi}_0$ increases gradually (Fig. 5.10(c)), and when the summation of F'_2 and F'_3 overcomes F'_1 , the solution of $f(\hat{\xi}) = 0$ vanishes, which leads to $f(\hat{\xi}) > 0$ for all $\hat{\xi}$ (Fig. 5.10(d)). Thus, the intrusion becomes accelerated suddenly (process C), and the flow reverses completely when the tip of the intrusion reaches the upper end of the pipe ($\hat{\xi} = \epsilon^{-1}$).

When the viscosities of the fluids are varied, the functional form of $f(\hat{\xi})$ changes significantly, as shown in Figs. 5.11 and 5.12. For large $\hat{\mu}_H$, $f(\hat{\xi})$ becomes relatively large, especially for small $\hat{\xi}$, which is due to the relatively large contribution of F'_3 (Fig. 5.11). Thus, the intrusion and hence the onset of its rapid growth occur even when \hat{x} is still large. On the other hand, for large $\hat{\mu}_L$, the value of $f(\hat{\xi})$ generally becomes small because of the large contribution of F'_1 (Fig. 5.12). Hence, the intrusion and the onset of its rapid growth occur, when \hat{x} becomes sufficiently small. In this way, the viscosity dependence of \hat{x}_{da} , \hat{x}_{db} , and \hat{x}_d are well explained.

Chapter 6

Other factors related to oscillation

In the previous chapters, I have shown that the behavior of density oscillation, particularly that of the flow-reversal process, is affected by the viscosities of the fluids, and have explained it using a model, in which the forces acting on a unit volume element at the tip of an intrusion at the flow-reversal process are considered. However, the behavior of density oscillation is thought to be also affected by several factors other than the viscosity. In this chapter, the effects of the length and diameter of a pipe, the density difference between the fluids, and the fluid materials are investigated.

6.1 Pipe length

It is considered that the pipe length relates to the flow-reversal process. I have performed the experiments, in which the pipe lengths are varied from 10 mm to 70 mm, while the pipe diameter is kept constant at 0.73 mm. For each pipe length, the viscosity of heavy fluid μ_H was varied, while that of light fluid μ_L is kept constant. In the present experimental conditions, $\beta\sigma^{1/2}/4 \leq 8.84 \times 10^{-2}$ is satisfied so that the viscous damping regime (see Sec. 2.1) is employed¹. Each up- and down-flow is found to be fitted well using an exponential function. As shown in Fig. 6.1, the difference between the asymptotic values for the exponential curves fitted to adjacent up- and down-flows Δ is almost consistent with the difference between the two hydrostatic equilibria δx , even when the length of a pipe and the viscosity of the fluid are varied.

The temporal evolution of an intrusion is shown in Fig. 6.2. The time and intrusion length are described by the non-dimensional variables \hat{t} and $\hat{\xi}$, respectively, because the non-dimensional description is helpful for us to understand whether the model proposed in the previous section (Eqs. (5.46)-(5.49)) is valid or not. Namely, if the model is valid,

¹Although $\beta\sigma^{1/2} \ll 1$ had to be satisfied so that the viscous damping regime was employed in the theory previously reported [31], it is obvious that it can be employed as far as $\beta\sigma^{1/2}/4 \ll 1$ is satisfied, because in this case the non-linear terms are negligibly small compared with the viscous terms in Eqs. (2.15) and (2.16).

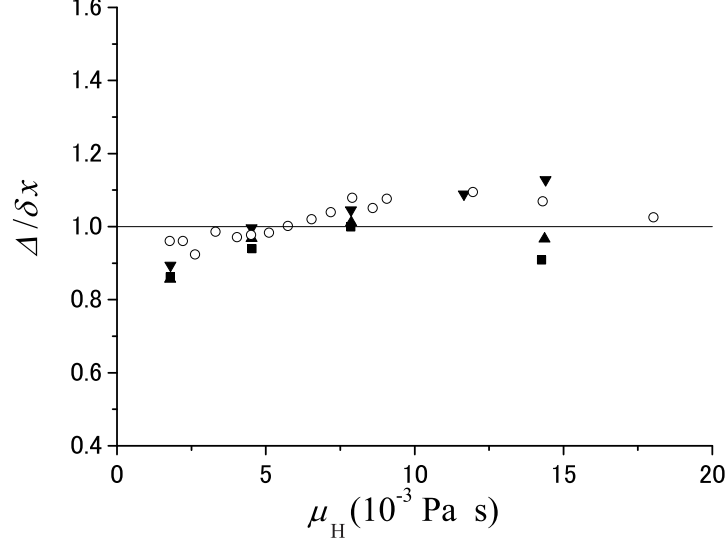


Figure 6.1: The ratio of the difference between the asymptotic values for the exponential curves fitted to adjacent up- and down-flows Δ to the difference between the two hydrostatic equilibria δx for various pipe lengths: 70mm (open circle), 50mm (filled square), 20mm (filled up triangle), and 10mm (filled down triangle). Each data is averaged over 4 cycles from the 2nd to the 5th. μ_H is varied while μ_L is fixed at $0.89 \times 10^{-3} \text{ Pa} \cdot \text{s}$.

the processes A and B and the non-dimensionalized time leading to the flow reversal in the process C will not be affected by the pipe length, since the pipe length relates only to ϵ in Eqs. (5.46) and (5.47), and since $d\hat{\xi}/d\hat{t} \propto \epsilon^{-1}$ is satisfied during the process C while the flow reverses at $\hat{\xi} = \epsilon^{-1}$.

It is clearly seen in Fig. 6.2 that even when the pipe length is varied, an intrusion grows slowly at first (process B), which is followed by the rapid growth (process C), and the growth rate in these processes decreases significantly as μ_H is increased. However, as the pipe length is shortened, the non-dimensionalized time taken for the processes B and C decrease significantly, which implies that the non-dimensionalized model is not quantitatively valid with respect to the change of the pipe length.

Figure 6.3 shows the heavy-fluid viscosity dependence of s_{da} , s_{db} , s_d , and s_u for various pipe lengths. We find that the experimental results are almost in good agreement with the simulations in the case of a long pipe. However, as the pipe length is shortened, s_{db} and s_d for large μ_H become slightly larger than the simulated values, and also the difference between s_{db} and s_d becomes smaller than the simulated result. These tendencies are considered to be originated from the fact that the non-dimensionalized time taken for the processes B and C decreases as the pipe length is shortened.

The case where the pipe length is extremely short is also examined. Because it is difficult to attach a short pipe at the bottom of the inner container, the orifice is made

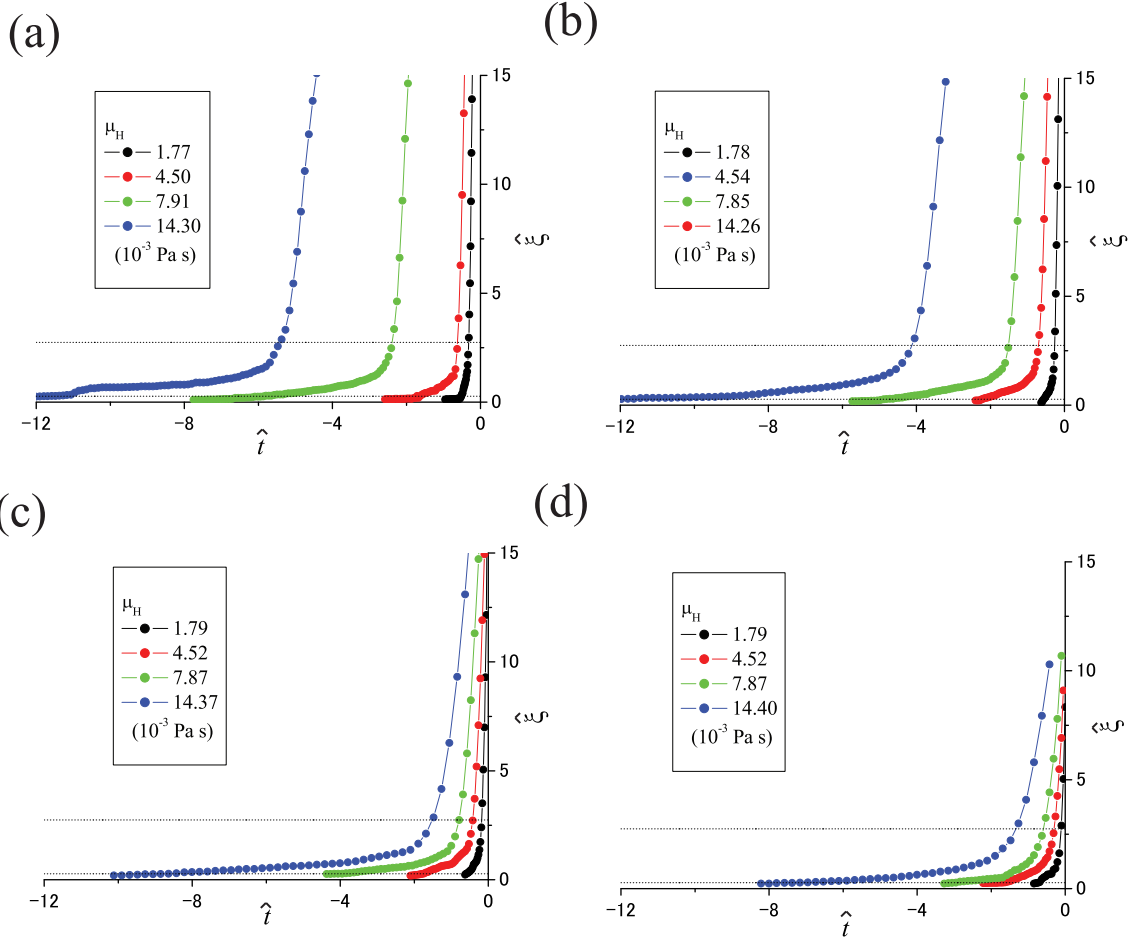


Figure 6.2: The temporal evolution of an intrusion for the pipe length of (a) 70 mm, (b) 50mm, (c) 20mm, and (d) 10mm. The data are shown in the non-dimensional form. The origin of the time \hat{t} is chosen to be the time when the flow reverses completely. For each pipe length, μ_H is varied while μ_L is fixed at $0.89 \times 10^{-3} \text{ Pa} \cdot \text{s}$. The dotted lines indicate 0.1 mm and 1 mm of intrusion length. In (d), the data for $\hat{\xi} > 10$ are not shown because the intrusion could not be observed because of the bottom of the inner container.

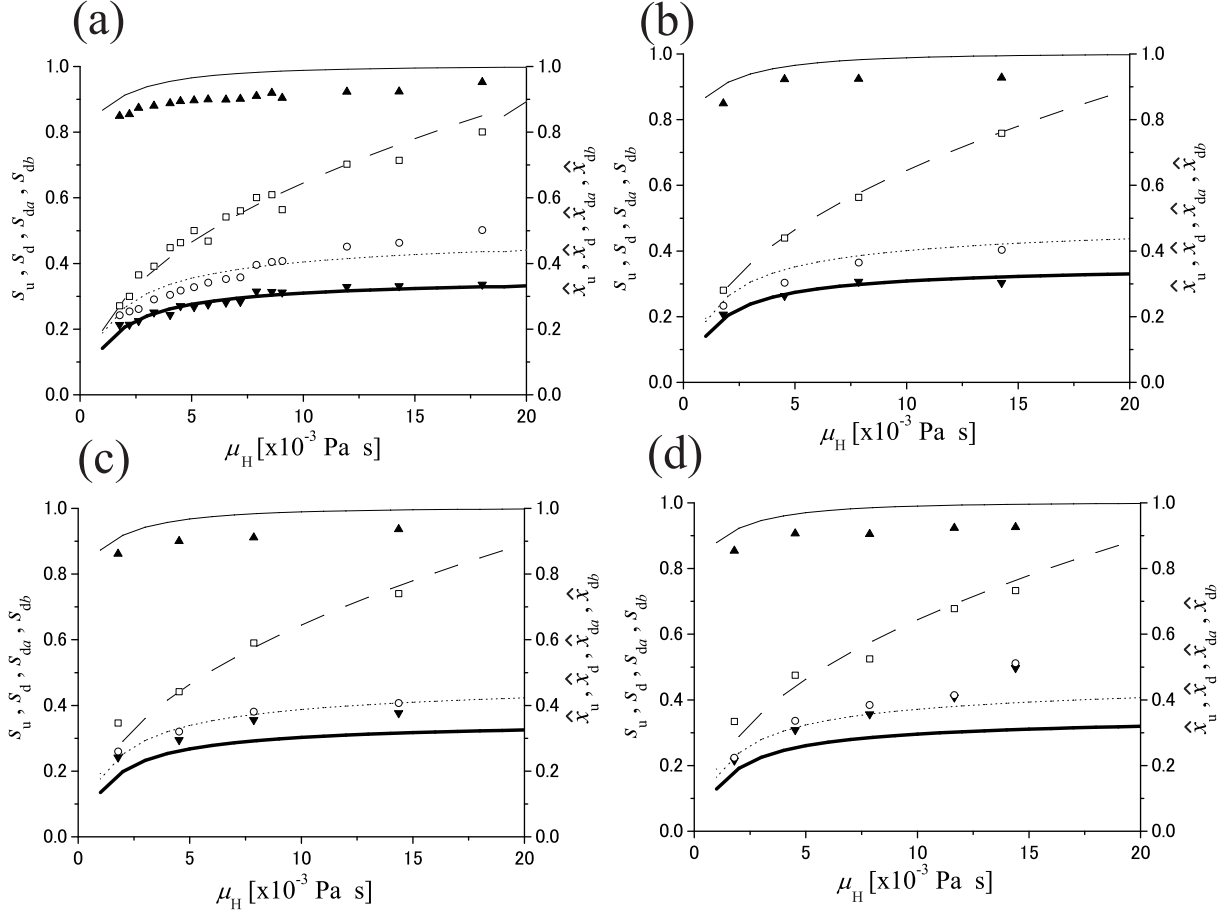


Figure 6.3: Viscosity dependence of s_u (filled up triangle), s_d (filled down triangle), s_{da} (open square), and s_{db} (open circle) for the pipe length of (a) 70 mm, (b) 50 mm, (c) 20mm, and (d) 10mm. μ_H is varied while μ_L is fixed at $0.89 \times 10^{-3} \text{ Pa} \cdot \text{s}$. The data are averaged over 4 cycles from the 2nd to the 5th. Simulated results \hat{x}_u (solid line), \hat{x}_d (bold line), \hat{x}_{da} (dashed line), and \hat{x}_{db} (dotted line) are also shown. The parameters of the simulation are as follows: $a = 0.365 \text{ mm}$, $\rho_H = 1.057 \times 10^3 \text{ kg m}^{-3}$, $\rho_L = 0.996 \times 10^3 \text{ kg m}^{-3}$, $\mu_L = 0.89 \times 10^{-3} \text{ Pa} \cdot \text{s}$, $S = 7.70 \times 10^{-4} \text{ m}^2$, $R = 1.44 \times 10^{-4}$, $b_1 = 10.7$, $b_2 = 160$, $k = 0.40 \text{ kg m}^{-1} \text{s}^{-3}$, $C_1=7.11$, $C_2=5.31$, $C_3=0.32$, $\alpha'=1.82$, and $\gamma'=0.30$.

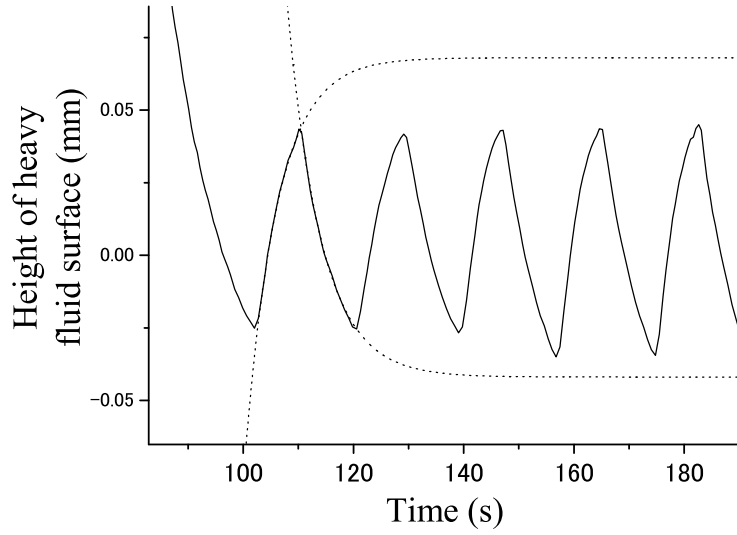


Figure 6.4: The temporal evolution of the height of the heavy fluid surface when a pipe is replaced by an orifice. The thickness of the bottom of the inner container is 2 mm, while the diameter of an orifice is 1.12 mm. The viscosities of the heavy and light fluids are $1.77 \times 10^{-3} \text{ Pa} \cdot \text{s}$ and $0.89 \times 10^{-3} \text{ Pa} \cdot \text{s}$, respectively. Although each up- and down-flow is seemingly well fitted by an exponential function, its asymptotic value is not consistent with that at the hydrostatic equilibrium (see Fig. 6.5).

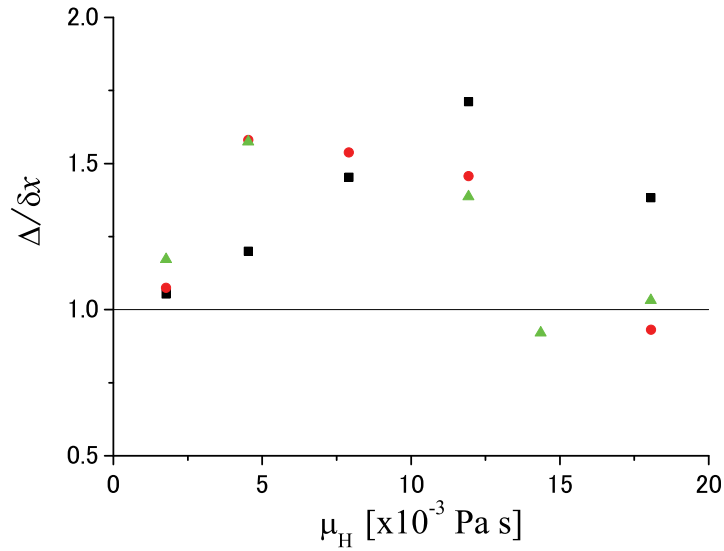


Figure 6.5: The ratio of the difference between the asymptotic values for the exponential curves fitted to adjacent up- and down-flows Δ to the difference between the two hydrostatic equilibria δx when a pipe is replaced by an orifice. The thickness of the bottom of the inner container is 5 mm (black filled square), 3 mm (red circle), and 2 mm (green up triangle). Each data is averaged over 4 cycles from the 2nd to the 5th. μ_H is varied while μ_L is fixed at $0.89 \times 10^{-3} \text{ Pa} \cdot \text{s}$.

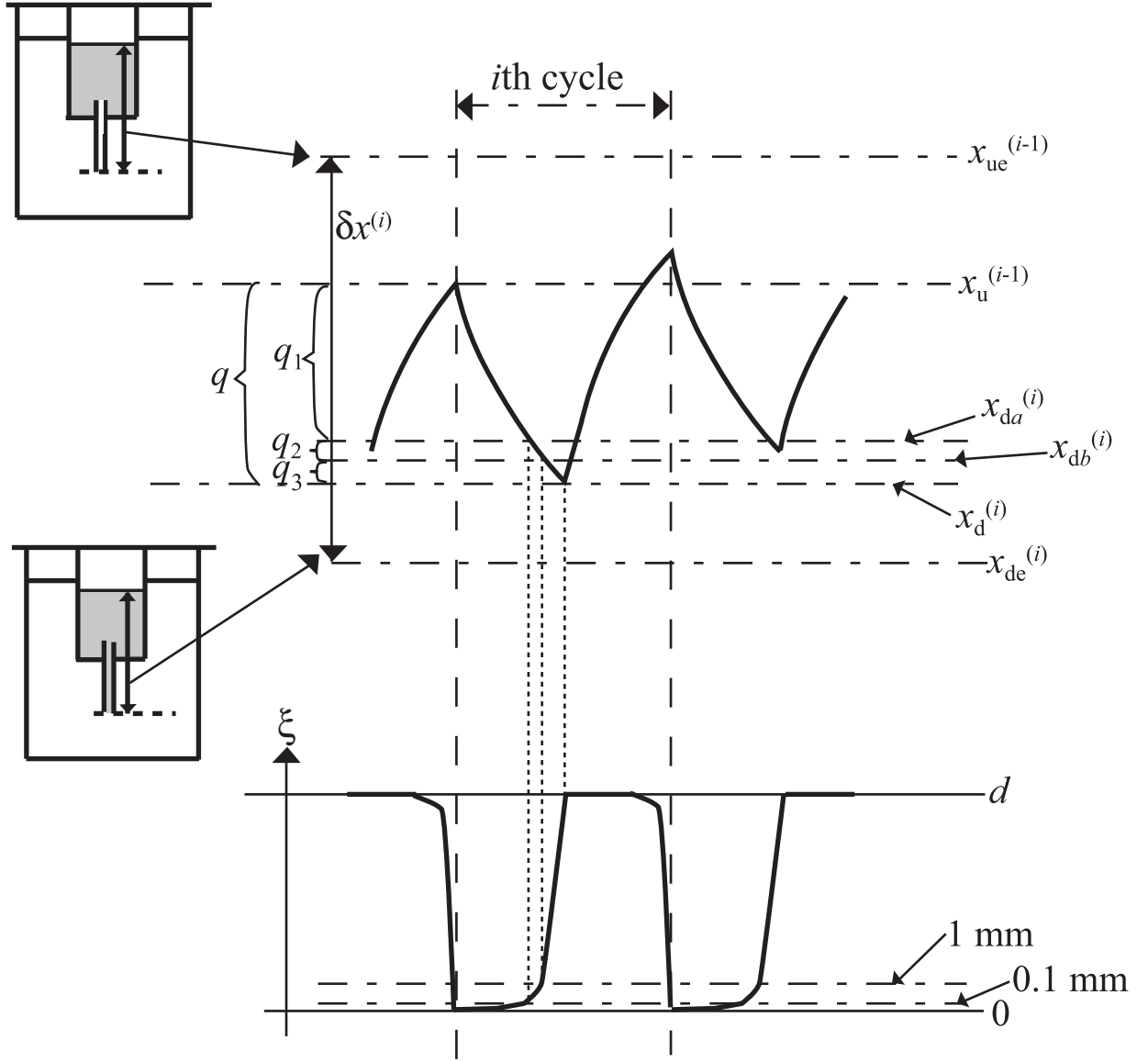


Figure 6.6: Definition of parameters. Upper picture is the scheme of the temporal evolution of the height of heavy fluid surface, while lower picture is that of the intrusion length ξ . $x_u^{(i-1)}$ and $x_d^{(i)}$ are the heights of the heavy fluid surface when the flow reverses from $(i-1)$ th up- to i th down-flow and i th down- to i th up-flow, respectively. x_{da} and x_{db} are the heights of the heavy fluid surface when the intrusion length becomes 0.1 mm and 1 mm, respectively. $x_{ue}^{(i-1)}$ and $x_{de}^{(i)}$ are the heights at the hydrostatic equilibria where a pipe is filled with light and heavy fluids, respectively, and $\delta x^{(i)}$ is the difference between the two. q_1 , q_2 , and q_3 characterize the difference between $x_u^{(i-1)}$ and $x_{da}^{(i)}$, $x_{da}^{(i)}$ and $x_{db}^{(i)}$, and $x_{db}^{(i)}$ and $x_d^{(i)}$, respectively, which are normalized by $\delta x^{(i)}$. q is the summation of q_1 , q_2 , and q_3 .

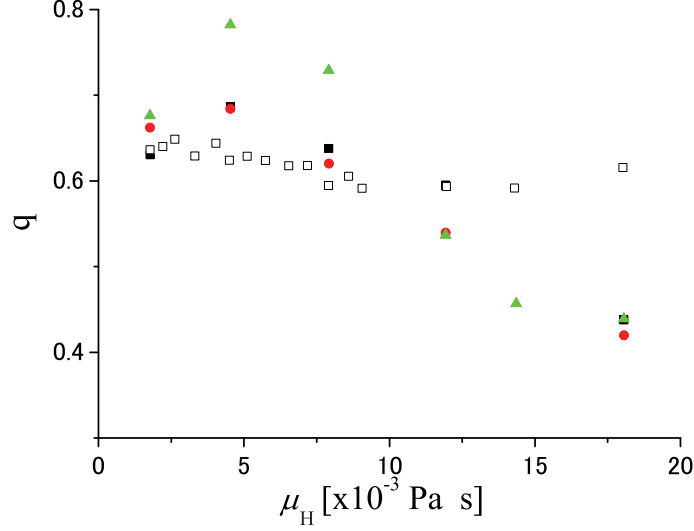


Figure 6.7: Viscosity dependence of q when a pipe is replaced by an orifice. The thickness of the bottom of the inner container is 5 mm (black filled square), 3 mm (red circle), and 2 mm (green up triangle). For $\mu_H > 14 \times 10^{-3} \text{ Pa} \cdot \text{s}$, the reproducibility of oscillation was poor and simultaneous up- and down-flow within an orifice was often observed. For comparison, the case where a pipe is used (the pipe diameter and length is 0.73 mm and 70 mm, respectively) is also shown (black open square).

at the bottom of the inner container by using a drilling machine. The diameter of the orifice is $1.12 \pm 0.02 \text{ mm}$, and the thickness of the bottom of the inner container (and hence the length of the orifice) is varied from 2 mm to 5 mm. Because it is difficult to observe the flow inside an orifice, only the height of the heavy fluid surface is measured.

Figure 6.4 shows the temporal evolution of the heavy fluid surface in the case where a pipe is replaced by an orifice. Although each up- and down-flow is seemingly well fitted by an exponential function, the difference between the asymptotic values for the adjacent exponential curves Δ is not consistent with the difference between the two hydrostatic equilibria δx , as shown in Fig. 6.5. This is probably because S/N ratio is low compared with the case of a long pipe and also because nonlinear damping terms in Eqs. (2.15) and (2.16) are no longer neglected in the present case. Thus, the parameters s_d , s_u , s_{da} , and s_{db} cannot be used for the present analysis. Instead, a new parameter q is introduced as follows:

$$q = \left\langle \frac{x_u^{(i-1)} - x_d^{(i)}}{\delta x^{(i)}} \right\rangle, \quad (6.1)$$

where $\langle \dots \rangle$ denotes the average over four cycles from the 2nd to 5th. In fact, q is an appropriate parameter for estimating the timings of the flow reversals because q becomes large when the flow reversal occurs near the hydrostatic equilibrium (see Fig. 6.6). Figure 6.7 shows the relation between q and μ_H for various thickness of the bottom of the inner container. It is clearly seen that q decreases significantly with increasing μ_H ,

although it does not depend much on μ_H when the pipe length is long. This tendency corresponds to the increase of s_d for large μ_H in Fig. 6.3. Moreover, for extremely large μ_H , the reproducibility of oscillation is poor, and simultaneous up- and down-flow in the orifice instead of oscillation is often observed.

6.2 Pipe diameter

Next, the viscosity-dependent flow-reversal processes for the inner pipe diameter of 1.60 mm and 3.50 mm are investigated. In the experiments, the pipe length is set constant at 50 mm and the surface areas of the inner and outer containers are set at $1.66 \times 10^{-3} \text{ m}^2$ and $1.24 \times 10^{-2} \text{ m}^2$, respectively. In the case of the pipe diameter of 3.50 mm, high speed camera (Photron FASTCAM Viewer) is used for the observation of the flow inside the pipe because the flow reversal occurs rapidly, and the pictures are taken at an interval of 0.33 s. Figure 6.8 shows an example of the pictures taken by the high speed camera. The interface between the heavy and light fluids is clearly seen.

Figure 6.9 shows the temporal evolution of an intrusion. It is found that even when the diameter is varied, the flow reversal begins with an intrusion (process B) and is followed by a rapid growth (process C), and the growth rate of the intrusion decreases significantly with increasing μ_H . Moreover, the onset of the rapid growth begins at $\hat{\xi} \sim 1$, which does not depend significantly on the diameter. However, in the case of the large diameter, the intrusion is accelerated gradually and thus the processes B and C are not clearly separated. In addition, for extremely large μ_H with the pipe diameter of 3.50 mm, an intrusion of light fluid is always observed during the down-flow, and the oscillation is quite irregular, as shown in Fig. 6.10.

Next, we analyze the height of the fluid surface at which the onset of intrusion and its rapid growth occurs. Because the nonlinear damping terms in Eqs. (2.15) and (2.16) are not negligible and hence each up- and down-flow is no longer fitted by an exponential function, the parameters s_d , s_u , s_{da} , and s_{db} cannot be used for the present analysis. Hence, the flow-reversal process is analyzed using the following parameters (see Fig. 6.6):

$$\begin{aligned} q_1 &= \left\langle \frac{x_u^{(i-1)} - x_{da}^{(i)}}{\delta x^{(i)}} \right\rangle, \\ q_2 &= \left\langle \frac{x_{da}^{(i)} - x_{db}^{(i)}}{\delta x^{(i)}} \right\rangle, \\ q_3 &= \left\langle \frac{x_{db}^{(i)} - x_d^{(i)}}{\delta x^{(i)}} \right\rangle, \end{aligned}$$

where $\langle \dots \rangle$ denotes the average over four cycles from the 2nd to 5th. Here, x_{da} and x_{db} denote the height of the heavy fluid surface when the non-dimensionalized intrusion

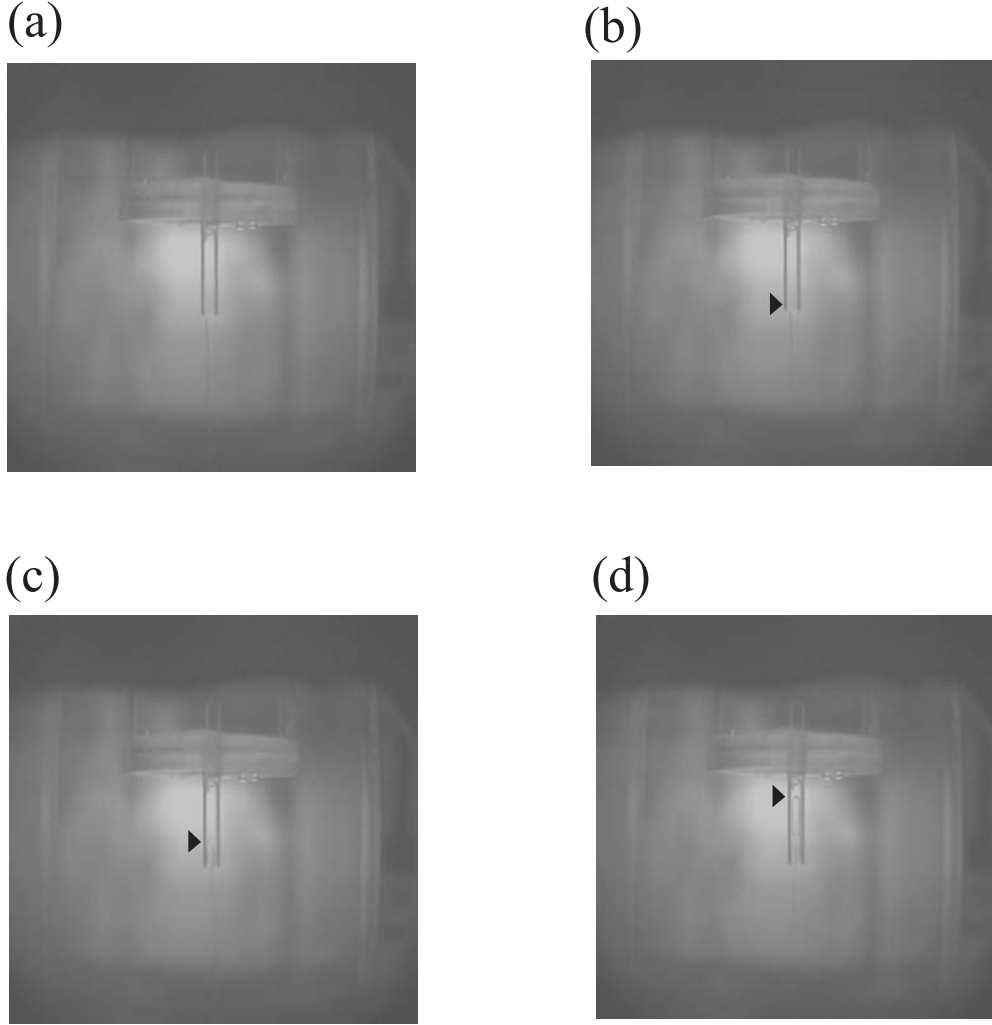


Figure 6.8: Microscopic images of the intrusion in the time course of down-flow ((a)→(b)→(c)→(d)) taken by the high speed camera. An intrusion of light fluid is clearly seen (arrowheads). The experimental conditions are as follows: $2a=3.5$ mm, $d=50$ mm, $\rho_H = 1.056 \times 10^3 \text{ kg} \cdot \text{m}^{-3}$, $\rho_L = 0.997 \times 10^3 \text{ kg} \cdot \text{m}^{-3}$, $\mu_H = 1.76 \times 10^{-3} \text{ Pa} \cdot \text{s}$ and $\mu_L = 0.89 \times 10^{-3} \text{ Pa} \cdot \text{s}$.

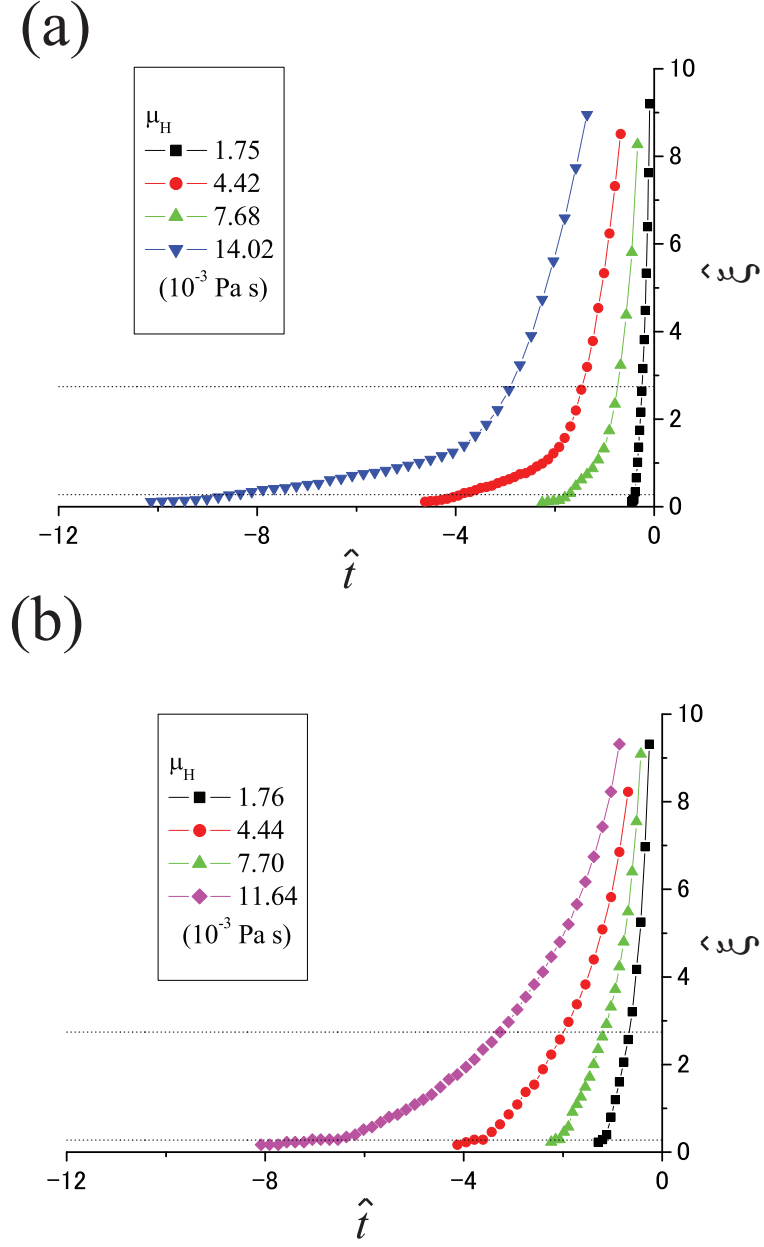


Figure 6.9: The temporal evolution of an intrusion for the pipe diameter of (a) 1.60 mm and (b) 3.50 mm. μ_H is varied while μ_L is fixed at $0.89 \times 10^{-3} \text{ Pa} \cdot \text{s}$. The data are shown in nondimensional forms. The dotted lines indicate $\hat{\xi} = 0.27$ and 2.74 .

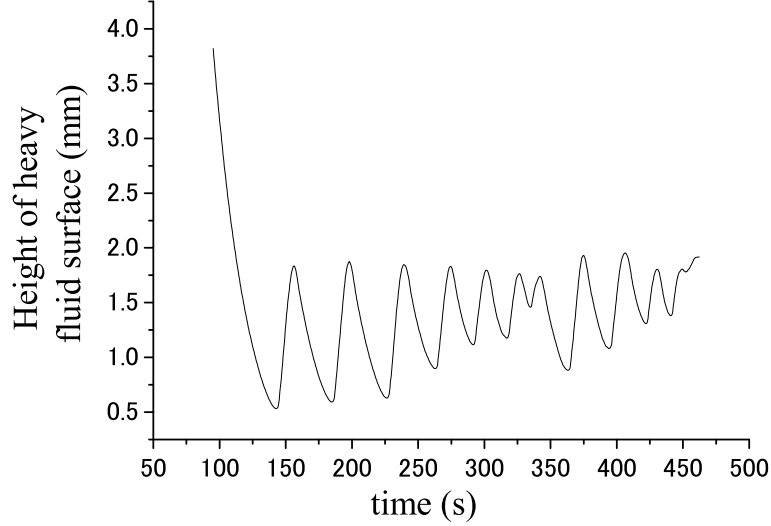


Figure 6.10: The temporal evolution of the height of the heavy fluid surface for the pipe diameter of 3.50 mm with $\mu_H = 14.02 \times 10^{-3} \text{ Pa} \cdot \text{s}$ and $\mu_L = 0.89 \times 10^{-3} \text{ Pa} \cdot \text{s}$. The waveform of oscillation is irregular.

length $\hat{\xi}$ becomes 0.27 and 2.74, respectively. Notice that the parameter q introduced in Eq. (6.1) corresponds to the summation of q_1 , q_2 and q_3 . Although we cannot exactly know the timing of the flow reversal from these parameters, q_1 , q_2 and q_3 roughly characterize the durations of the processes A, B, and C, respectively.

Figure 6.11 shows the heavy-fluid viscosity dependence of q_1 , q_2 , q_3 , and q for the pipe diameter of 1.60 mm and 3.50 mm. For comparison, the values of these parameters at the experimental conditions shown in Chap. 3, where the pipe diameter of 0.73 mm is employed, are shown in Fig. 6.12. It is clearly seen in Fig. 6.12 that q_1 decreases, while q_2 and q_3 increase as μ_H is increased, whereas q does not depend much on μ_H . However, when the pipe diameter is large, q_2 and q_3 are relatively small for large μ_H , while q_1 is relatively large particularly for small μ_H , and as a consequence q decreases with increasing μ_H , as shown in Fig. 6.11.

From these results, I speculate that the flow reversal from the down- to up-flow in the case of the large pipe diameter occurs in the following way: For small μ_H , the intrusion does not occur until the height of the fluid surface becomes close to the hydrostatic equilibrium. On the other hand, for large μ_H , the onset of an intrusion occurs even when the height of the fluid surface is still high, and once the intrusion occurs, it is gradually accelerated and then the flow reverses immediately.

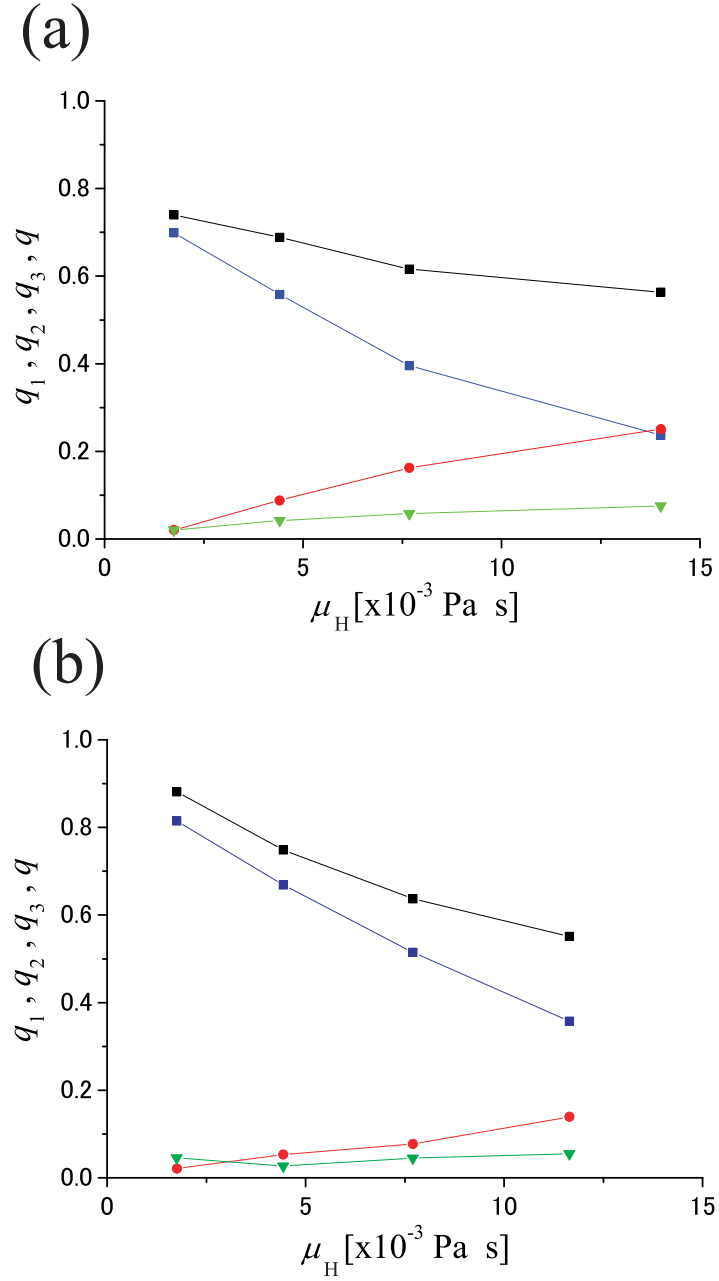


Figure 6.11: The values of q_1 (blue square), q_2 (red circle), q_3 (green down triangle) and q (black square) for the pipe diameter of (a) 1.60 mm and (b) 3.50 mm. μ_H is varied while μ_L is fixed at $0.89 \times 10^{-3} \text{ Pa} \cdot \text{s}$.

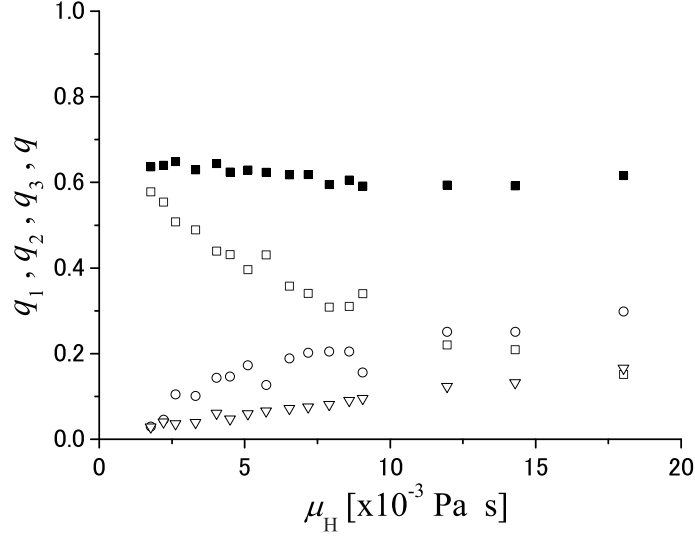


Figure 6.12: The values of q_1 (open square), q_2 (open circle), q_3 (open down triangle) and q (filled square) for the pipe diameter of 0.73 mm. The experimental conditions are same as those in Chap. 3. μ_H is varied while μ_L is fixed at $0.89 \times 10^{-3} \text{ Pa} \cdot \text{s}$.

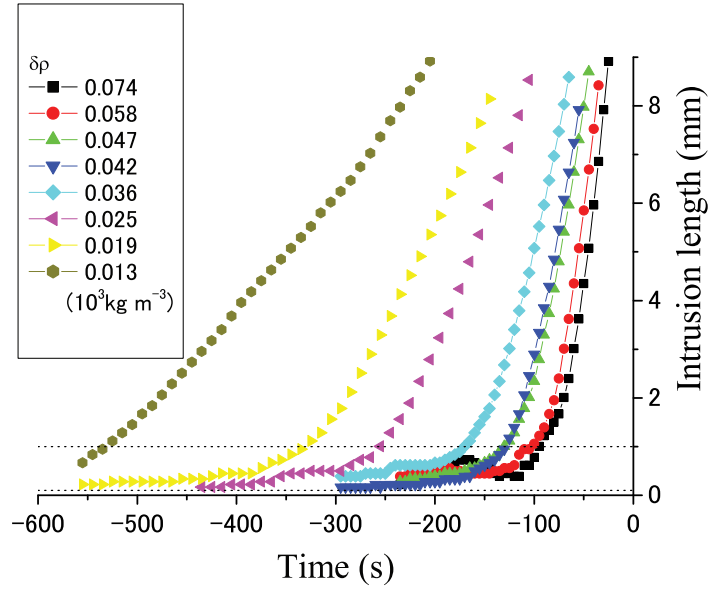


Figure 6.13: Density-difference dependence of the temporal evolution of the intrusion. Because of the limitation of the visual field under the stereomicroscope, an intrusion length of more than 8 mm is not observed. The dotted lines indicate 0.1 mm and 1 mm of intrusion length.

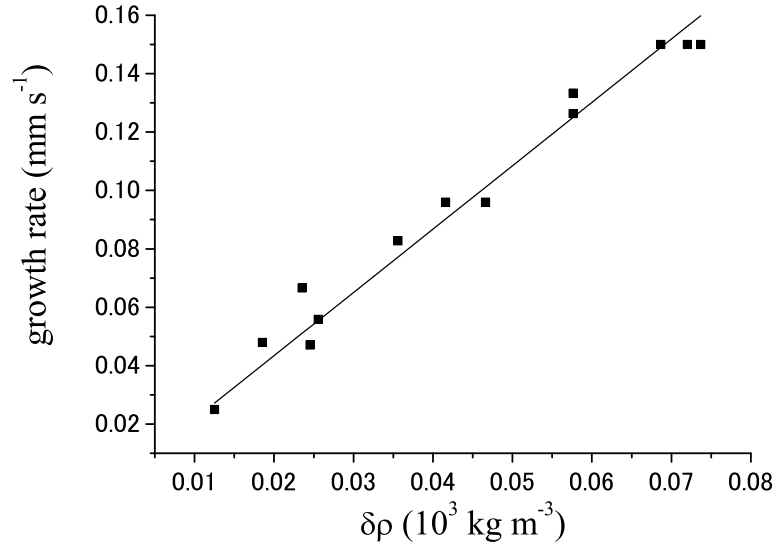


Figure 6.14: The relation between the average growth rate from 2mm to 8mm of the intrusion length and the density difference $\delta\rho$. These two are in proportional relation (solid line).

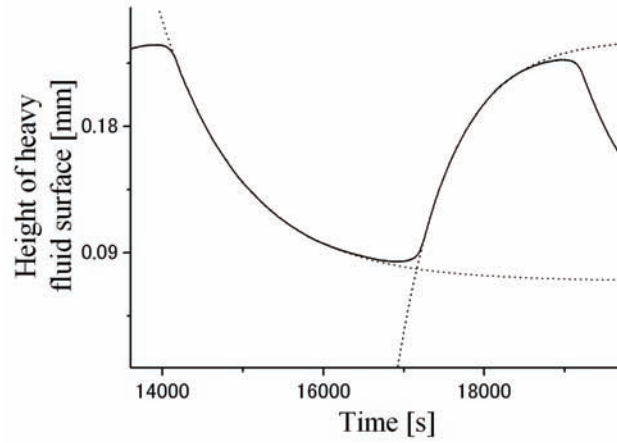


Figure 6.15: Temporal evolution of the height of the heavy fluid surface when $\delta\rho$ is extremely small: $\rho_L = 0.997 \times 10^3 \text{ kg} \cdot \text{m}^{-3}$, $\rho_H = 1.003 \times 10^3 \text{ kg} \cdot \text{m}^{-3}$, $\mu_H = 1.39 \times 10^{-3} \text{ Pa} \cdot \text{s}$, and $\mu_L = 0.86 \times 10^{-3} \text{ Pa} \cdot \text{s}$. Each branch for up- and down-flow is well fitted by an exponential curve (dotted line), but deviates from it significantly before the flow reversal.

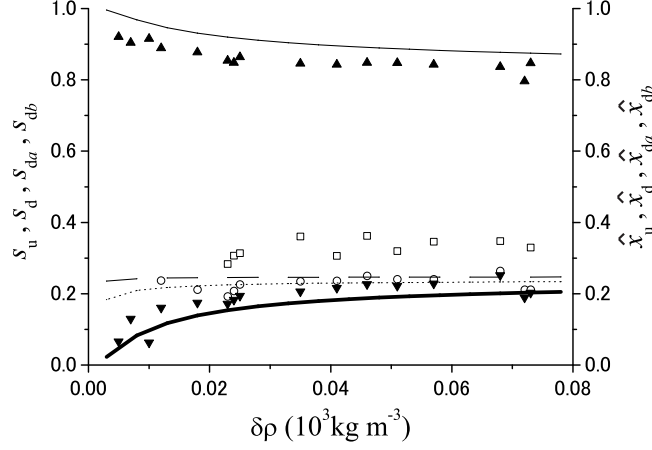


Figure 6.16: Density-difference dependence of s_u (filled up triangle), s_d (filled down triangle), s_{da} (open square), and s_{db} (open circle). The data are averaged over 4 cycles from the 2nd to the 5th. The density of the light fluid was kept constant at $0.997 \times 10^3 \text{ kg} \cdot \text{m}^{-3}$. The viscosities of the heavy and light fluids were $(1.45 \pm 0.07) \times 10^{-3} \text{ Pa} \cdot \text{s}$ and $0.86 \times 10^{-3} \text{ Pa} \cdot \text{s}$, respectively. Because the interface between the fluids is not clearly observed when density difference is small, s_{da} and s_{db} are not shown for small $\delta\rho$. Simulated results \hat{x}_u (solid line), \hat{x}_d (bold line), \hat{x}_{da} (dashed line), and \hat{x}_{db} (dotted line) are also shown. The parameters of the simulation are as follows: $a = 0.365 \text{ mm}$, $d = 50 \text{ mm}$, $\rho_L = 0.996 \times 10^3 \text{ kg m}^{-3}$, $\mu_H = 1.45 \times 10^{-3} \text{ Pa} \cdot \text{s}$, $\mu_L = 0.89 \times 10^{-3} \text{ Pa} \cdot \text{s}$, $S = 1.66 \times 10^{-3} \text{ m}^2$, $R = 0.337$, $b_1 = 10.7$, $b_2 = 160$, $k = 1.07 \times 10^{-4} \times \delta\rho^2 \text{ kg m}^{-1}\text{s}^{-3}$, $\alpha' = 1.82$, and $\gamma' = 0.30$.

6.3 Density of fluid

Next, the density difference between the fluids is varied. In the experiments, glucose solution and water are used as the heavy and light fluids, respectively, and the concentration of the glucose solution is varied, which changes the density of the heavy fluid. Moreover, a small amount of methyl-cellulose is dissolved into the heavy fluid to keep the viscosity nearly constant. The viscosities of the heavy and light fluids are $(1.45 \pm 0.07) \times 10^{-3} \text{ Pa} \cdot \text{s}$ and $0.86 \times 10^{-3} \text{ Pa} \cdot \text{s}$, respectively. The surface areas of the inner and outer containers are $1.66 \times 10^{-3} \text{ m}^2$ and $4.93 \times 10^{-3} \text{ m}^2$, and the diameter and length of a pipe are 0.73 mm and 50 mm , respectively. The temperature of the fluid is kept at $26.5 \pm 0.5^\circ\text{C}$.

Figure 6.13 shows the temporal evolution of the intrusion length. Even when the density difference between the fluids $\delta\rho$ is varied, the flow reversal begins with an intrusion (process B) and is followed by the rapid growth (process C). Noticeably, the onset of the rapid growth begins at about 1 mm in the intrusion length, irrespective of $\delta\rho$. After the onset of the rapid growth, the growth rate depends much on $\delta\rho$. As shown in Fig. 6.14, the average growth rate from 2 mm to 8 mm of the intrusion length is almost in proportion to $\delta\rho$.

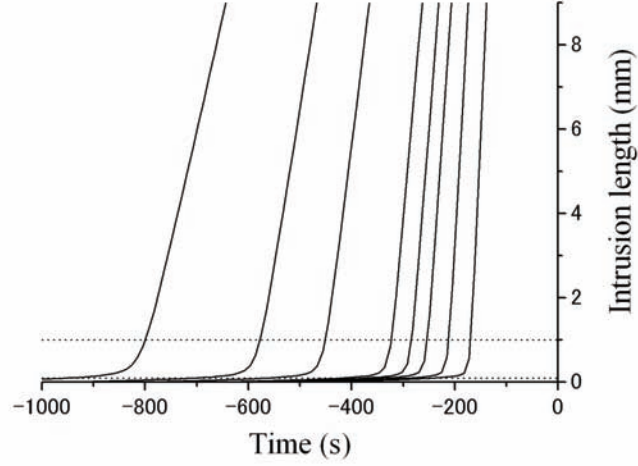


Figure 6.17: The simulated result of the temporal evolution of an intrusion when $\delta\rho$ is varied while ρ_L is fixed at $0.997 \times 10^3 \text{ kg} \cdot \text{m}^{-3}$. Each curve corresponds to $\delta\rho = 0.013, 0.019, 0.025, 0.036, 0.042, 0.047, 0.058, \text{ and } 0.074 (\times 10^3 \text{ kg} \cdot \text{m}^{-3})$ from left to right, respectively. The dotted lines denote 0.1 mm and 1 mm of intrusion length. The parameters of the simulation are as follows: $a = 0.365 \text{ mm}$, $d = 50 \text{ mm}$, $\rho_L = 0.996 \times 10^3 \text{ kg m}^{-3}$, $\mu_H = 1.45 \times 10^{-3} \text{ Pa} \cdot \text{s}$, $\mu_L = 0.89 \times 10^{-3} \text{ Pa} \cdot \text{s}$, $S = 1.66 \times 10^{-3} \text{ m}^2$, $R = 0.337$, $b_1 = 10.7$, $b_2 = 160$, $k = 1.07 \times 10^{-4} \times \delta\rho^2 \text{ kg m}^{-1}\text{s}^{-3}$, $\alpha' = 1.82$, and $\gamma' = 0.30$.

Figure 6.15 shows the temporal evolution of the height of the heavy fluid surface in the case where the density difference $\delta\rho$ is extremely small. Even in this case each up- and down-flow is fitted by an exponential function, and the asymptotic values of the exponential functions are generally in good agreement with the theoretical values derived from Eqs. (2.15) and (2.16). However, the height clearly deviates from the exponential response before the flow reversal, which is thought to be due to the slow growth of the intrusion in the process C.

The density-difference dependence of s_d , s_u , s_{da} and s_{db} is shown in Fig. 6.16. Although s_{da} and s_{db} do not depend much on $\delta\rho$, s_d decreases while s_u increases as $\delta\rho$ is decreased. This is probably because the time taken for the process C is extremely long when $\delta\rho$ is small and thus the flow-reversal process does not completely finish until the height of the heavy fluid surface approaches near the hydrostatic equilibrium, while the processes A and B do not depend on $\delta\rho$.

These density-dependent behaviors are compared with the simulations of the model. Figure 6.17 shows the simulated result of the temporal evolution of the intrusion length where the parameters b_1 , b_2 and k are chosen so that the relation $k \propto \delta\rho^2$ is satisfied, while b_1 and b_2 take constant values with regard to $\delta\rho$ (hence, C_1 , C_2 , and C_3 are all in proportion to $\delta\rho$). Obviously, the onset of the rapid growth of intrusion occurs at the

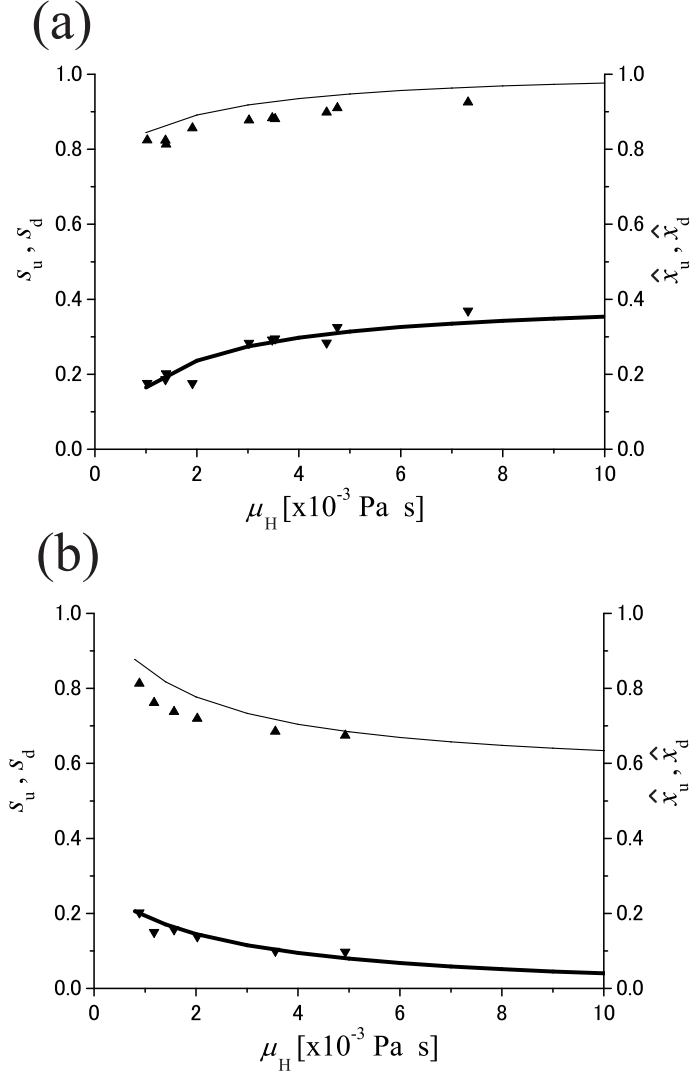


Figure 6.18: Viscosity dependence of s_u (filled up triangle) and s_d (filled down triangle) when glucose solution and water were used as the heavy and light fluids with methyl-cellulose dissolved to change the viscosity. The data are averaged over 4 cycles from the 2nd to the 5th. Simulated results \hat{x}_u (solid line) and \hat{x}_d (bold line) are also shown. (a) μ_H is varied while μ_L is fixed at $0.89 \times 10^{-3} \text{ Pa} \cdot \text{s}$. (b) μ_L is varied while μ_H is fixed at $1.40 \times 10^{-3} \text{ Pa} \cdot \text{s}$. The parameters of the simulation are as follows: $a = 0.365 \text{ mm}$, $d = 50 \text{ mm}$, $\rho_H = 1.060 \times 10^3 \text{ kg m}^{-3}$, $\rho_L = 0.996 \times 10^3 \text{ kg m}^{-3}$, $S = 1.66 \times 10^{-3} \text{ m}^2$, $R = 7.76 \times 10^{-2}$, $b_1 = 10.7$, $b_2 = 160$, $k = 0.42 \text{ kg m}^{-1} \text{s}^{-3}$, $\alpha' = 1.82$, and $\gamma' = 0.30$.

same intrusion length even when $\delta\rho$ is varied, and the growth rate during the process C is slow for small $\delta\rho$, which is qualitatively in good agreement with the experimental result. The density-difference dependence of the values of \hat{x}_d , \hat{x}_u , \hat{x}_{da} and \hat{x}_{db} is shown in Fig. 6.16. It is clearly seen that \hat{x}_d , \hat{x}_u , \hat{x}_{da} and \hat{x}_{db} are generally in good agreement with s_d , s_u , s_{da} and s_{db} , although \hat{x}_u and \hat{x}_{da} are slightly larger than s_u and s_{da} , respectively.

6.4 Fluid materials

While the mixtures of water, one-propanol, and glycerin are used in the experiments shown in Chap. 4, the viscosity dependence of the flow reversal is also investigated with using other materials: glucose solution and water are used as the heavy and light fluids, respectively, and methyl-cellulose is dissolved into the fluids to change the viscosity without changing the density. The densities of the heavy and light fluids are kept constant at $(1.060 \pm 0.002) \times 10^3 \text{ kg} \cdot \text{m}^{-3}$ and $0.997 \times 10^3 \text{ kg} \cdot \text{m}^{-3}$, respectively. In the present experiment, the surface areas of the inner and outer containers are $1.66 \times 10^{-3} \text{ m}^2$ and $2.34 \times 10^{-2} \text{ m}^2$, and the length and the diameter of a pipe are 50 mm and 0.73 mm, respectively.

Figure 6.18 shows the viscosity dependence of s_d and s_u when glucose solution and water are used as the fluids. The simulated results obtained from Eqs. (5.46)-(5.49) are also shown. It is obvious that the viscosity dependence of s_d and s_u is well reproduced by the model. It is noted that the temporal evolution of an intrusion is not quantitatively measured in the present experiment, and thus s_{da} and s_{db} are not obtained. However, it is observed by the naked eyes that an intrusion grows extremely slowly at the flow reversal from down- (up-) to up- (down-) flow for large $\mu_H(\mu_L)$, which qualitatively agrees with the results when the mixtures of water, 1-propanol, and glycerin are used as the fluids.

6.5 Summary

In this section, I will briefly summarize the results obtained when a short pipe or an orifice is employed (Sec. 6.1), when the pipe diameter is large (Sec. 6.2), when the density difference between the fluids is small (Sec. 6.3), and when other materials are used as the fluids (Sec. 6.4).

(Short pipe)

- Non-dimensionalized time taken for the processes B and C is relatively short.

- s_{db} and s_d are relatively large.
- The difference between s_{db} and s_d is relatively small.

(Orifice)

- q decreases with increasing μ_H .
- Simultaneous up- and down-flow is observed for extremely large μ_H .

(Large pipe diameter)

- Onset of the rapid growth of intrusion occurs at $\hat{\xi} \sim 1$.
- An intrusion is accelerated throughout the processes B and C.
- q_2 and q_3 is relatively small for large μ_H .
- q_1 is relatively large for small μ_H .
- Irregular oscillation is observed for extremely large μ_H .

(Small density difference)

- Onset of the rapid growth of intrusion occurs at $\xi \sim 1$ mm.
- Growth rate in the process C is in proportion to $\delta\rho$.
- The height of the fluid surface clearly deviates from exponential response before the flow reversal.
- s_d is relatively small while s_u is relatively large.
- The above results are reproduced by the simulation by putting $k \propto \delta\rho^2$.

(Other fluid materials)

- The result is well reproduced by the simulation.

Chapter 7

Discussion

7.1 Mechanism of density oscillation

I have investigated the mechanism of density oscillation experimentally and theoretically. Particularly, I have focused on the mechanism of the flow-reversal process, which is essential but has not been well understood [31, 40]. In the above experiments, it is found that the flow reversal from down- to up-flow in a density oscillator occurs in the following way: At first, the heavy fluid flows in one-way (process A). After a while, the light fluid intrudes into the pipe and the intrusion grows rather slowly (process B). When it grows to some extent, it suddenly begins to grow rapidly (process C). Finally, the flow reverses completely when it reaches the upper end of the pipe. The flow reversal in the opposite direction also occurs in the similar way.

When the viscosities of the fluids are changed, the flow-reversal process is found to change significantly. In the case of the flow-reversal from down- to up-flow, for instance, an intrusion of the light fluid starts long before the flow reversal and grows slowly when the viscosity of the heavy fluid is larger than that of the light fluid, while an intrusion does not occur until the height of the heavy fluid surface becomes close to that at the hydrostatic equilibrium when the viscosity of the light fluid is larger than that of the heavy fluid.

Since it is difficult to analyze the viscosity-dependent flow-reversal process strictly, I have described it by a simple model in which three forces acting on the tip of the intrusion (viscous drag force F_1 , hydrostatic pressure gradient F_2 , and the effect of acceleration of fluid that has passed through a pipe F_3) are taken into account. Then, it is found that the model well reproduces the experimental result.

Although the model reported previously (Eq. (2.29)) described the phenomenological behavior of oscillation [32–34], the essential mechanism of the oscillation was not well understood. On the contrary, the present model properly describes the whole oscillatory

behavior based on its essential mechanism. Namely, the present model properly includes the mechanism of the flow-reversal process, which is a key process of the oscillation. Indeed, I conclude from the present model that the flow-reversal process occurs in the following way:

1. The acceleration of the flow that has passed through a pipe causes the contraction of the flow, which triggers the fluid to intrude into the pipe (F_3).
2. After the intrusion occurs, it does not grow immediately but grows slowly, because the viscous drag force (F_1) hinders the growth of the intrusion.
3. As the height of the heavy fluid surface approaches the hydrostatic equilibrium, the viscous drag force (F_1) decreases while the hydrostatic pressure gradient (F_2) which accelerates the intrusion increases. Then, at a threshold, the intrusion is accelerated suddenly and begins to grow rapidly.
4. The flow reverses completely when the intrusion reaches the upper (lower) end of the pipe.

Thus, the present model is expected to become a useful model for the future studies on the density oscillator. In the following, I will discuss several important aspects of the model in detail.

7.1.1 Properties of forces

From the model, the properties of the three forces can be well understood. In the non-dimensionalized model (Eqs. (5.46)-(5.49)), the three forces are characterized by F'_1 , F'_2 , and F'_3 . As shown in Sec. 5.3, the contributions of these forces vary depending on the value of the non-dimensionalized height of the heavy fluid surface \hat{x} . When the non-dimensionalized viscosities $\hat{\mu}_H$ and $\hat{\mu}_L$ are constants of $O(1)$, the contributions of F'_1 and F'_2 are of the same order, and F'_1 is dominant at large \hat{x} , while F'_2 is dominant at small \hat{x} . The contribution of F'_3 is small as compared with F'_1 and F'_2 when \hat{x} is large. However, when the value of \hat{x} becomes small, F'_3 becomes comparable to F'_1 and F'_2 and causes the intrusion (see Fig. 5.10).

When the viscosity of the fluid is changed, the properties of the forces change considerably: the contribution of F'_3 becomes relatively large for large $\hat{\mu}_H$, while that of F'_1 becomes relatively large for large $\hat{\mu}_L$. Such viscosity dependence is originated from the fact that the viscosity of the fluid at the interface $\hat{\mu}_I$ depends both on the viscosities of the heavy and light fluids while the velocity of down- (up-) flow depends solely on the viscosity of the heavy (light) fluid, and that the effect of the acceleration of the flow that has passed through the pipe F_3 is related to the velocity of the flow. Although

the effect of the viscosity to the flow-reversal process was not considered in the analysis reported previously [40], I have properly taken it into account and described the viscosity-dependent behaviors quite well.

The properties of the forces are characterized by the parameters α' , γ' , C_1 , C_2 , and C_3 , as well as by the viscosities of the fluids. α' and γ' characterize not only the region where the pressure gradient is not simply derived from the height of the fluid surface, but also the intrusion length where the onset of its rapid growth occurs. Obviously, the characteristic length of this region is thought to be of the order of the pipe diameter. In fact, the onset of the rapid growth of an intrusion occurs necessarily at $\hat{\xi} \sim 1$, as shown in Chaps. 4 and 6. Thus, it is expected that α' and γ' are constants of $O(1)$. Actually, the values we set to fit the experimental result, *i.e.*, $\alpha' = 1.82$ and $\gamma' = 0.30$, are within this order, and these values do not vary depending on experimental conditions. Hence, with regard to the parameters α' and γ' , the present model has a universal character.

On the other hand, the parameters C_1 , C_2 , and C_3 , which characterize the contributions of F'_1 , F'_2 , and F'_3 , respectively, are thought to depend on the pipe diameter (see Eqs. (5.41)-(5.43)). As shown in Sec. 6.2, when the pipe diameter is large, q_1 is relatively large for small $\hat{\mu}_H$ and hence it is considered that in this case an intrusion does not occur until the height of the fluid surface approaches close to the hydrostatic equilibrium. However, q_1 decreases significantly as $\hat{\mu}_H$ is increased. This result implies that the contribution of F'_1 is larger than that of F'_2 for the large pipe diameter, and the contribution of F'_3 becomes comparable to F'_1 as $\hat{\mu}_H$ is increased. Hence, it is considered that C_1 and C_3 are relatively large while C_2 is relatively small for the large pipe diameter.

C_1 , C_2 , and C_3 contain the parameters b_1 , b_2 , and k , which are determined experimentally. If we assume b_1 , b_2 , and k are constants with regard to the pipe diameter, it is found from Eqs. (5.41)-(5.43) that $C_1 \propto a^{-2}$, $C_2 \propto a^{-2}$, and $C_3 \propto a^{-4}$, respectively. However, since the contributions of C_1 and C_3 become relatively large as the pipe diameter increases, it is considered that k increases significantly as the pipe diameter increases. Moreover, b_1 is also thought to increase as the pipe diameter increases, although its detailed mechanism is still unclear.

The parameters C_1 , C_2 , and C_3 also depend on the density difference between the fluids $\delta\rho$. In Sec. 6.3, I have shown that the intrusion length where the onset of the rapid growth of the intrusion occurs does not depend on $\delta\rho$ and the growth rate during the process C is in proportion to $\delta\rho$. These behaviors have been well reproduced by the simulation with putting k as $k \propto \delta\rho^2$ and b_1 and b_2 as constants with regard to $\delta\rho$, so that C_1 , C_2 , and C_3 become all in proportion to $\delta\rho$. Intuitively, the increase of k with increasing $\delta\rho$ is qualitatively understandable, because the acceleration of the fluid that has passed through a pipe is thought to be in proportion to $\delta\rho$. However, the reason

that k is in proportion not to $\delta\rho$ but to $\delta\rho^2$ is still unclear.

7.1.2 Future problems concerning the model

As described above, the model contains the essence of density oscillation. Whereas the model describes the behavior of oscillation fairly well, there remains some problems. In the following, I will discuss them individually.

Growth rate of intrusion

At the derivation of F_1 , I have assumed that the shear stress at the pipe wall σ'_s is in proportion to the viscosity at the interface μ_I , for simplicity. However, it is considered that σ'_s is actually in proportion to the viscosity of the fluid of intrusion. Now consider how the behavior changes if the relation $\sigma'_s \propto \mu_L$ is assumed to hold in the case of the flow reversal from down- to up-flow. In this case, F_1 is described in the following way:

$$\begin{aligned} F_1 &= \frac{b_1(\mu_H + \mu_L)}{2a^2} \left(\frac{S}{\pi a^2} \dot{x} - \dot{\xi} \right) - \frac{b'_2 \mu_L}{a^2} \dot{\xi} \\ &= \frac{b_1(\mu_H + \mu_L)}{2a^2} \frac{S}{\pi a^2} \dot{x} - \left[\frac{b_1(\mu_H + \mu_L)}{2a^2} + \frac{b'_2 \mu_L}{a^2} \right] \dot{\xi}, \end{aligned} \quad (7.1)$$

where b'_2 is a positive constant. It is found that Eq. (7.1) is obtained by replacing b_2 in Eq. (5.8) with $b_1 + 2b'_2 \mu_L / (\mu_H + \mu_L)$. Hence, we can regard b_2 as a variable dependent on the viscosities of fluids: it decreases as μ_H is increased while it increases as μ_L is increased. Meanwhile, because the non-dimensionalized parameters C_1 , C_2 , and C_3 in Eqs. (5.47) and (5.49) are all in proportion to b_2^{-1} , the growth rate of intrusion is in proportion to b_2^{-1} . Hence, when μ_H (μ_L) is large, the growth rate in the process C under the assumption of $\sigma'_s \propto \mu_L$ should be faster (slower) than that under the assumption of $\sigma'_s \propto \mu_I$, while the processes A and B should not be affected by the assumptions.

However, even when $\sigma'_s \propto \mu_I$ is assumed, the growth rate of an intrusion in the case of $\mu_L > \mu_H$ at the flow reversal from down- to up-flow is somewhat slower in the simulation than in the experiment (Figs. 4.8 and 5.9). Hence, if we assume $\sigma'_s \propto \mu_L$, the discrepancy of the growth rate between the simulation and the experiment is thought to become large.

Such discrepancy of the growth rate is thought to be closely related to the actual width of the intrusion within the pipe. As described above, it has been found experimentally that the width of the intrusion is smaller for $\mu_L > \mu_H$ (Fig. 4.10). It is considered that as the width becomes smaller, the growth of an intrusion becomes less hindered, which enables the intrusion to grow more rapidly. The reason for the relatively slow growth rate in the simulation is thought to be due to the neglect of this effect. However, the reason that the width depends on the viscosities of the fluids is not yet clear.

It is noted that the fact that \hat{x}_d becomes slightly lower than s_d (Fig. 4.7) is thought to be due to the discrepancy of the growth rate. The fact that \hat{x}_u is slightly larger than s_u for $\mu_H > \mu_L$ is considered in the similar manner. Hence, for the proper description of the flow-reversal process, the effect of the width of intrusion should be properly considered.

Acceleration effect

As the flow is obstructed by the intrusion, the intrusion should be accelerated because the intrusion is less obstructed by the flow. Then, the flow becomes much more obstructed by the accelerated intrusion. In this way, the positive feedback loop should exist at the flow-reversal process, although it is not considered in the model. In fact, we have observed that the intrusion is accelerated gradually as the intrusion approaches the upper end of the pipe. While the acceleration occurs at the late stage of the process C (hence it occurs out of the visual field of the stereomicroscope) when the pipe diameter is small, it occurs obviously throughout the processes B and C when the pipe diameter is large, as shown in Fig. 6.9.

The deviation from exponential response before the flow reversal shown in Figs. 4.1 and 6.15 is thought to be caused by the acceleration of intrusion. Actually, the deviation is found to occur at the process C, which corresponds to the timing when the acceleration of intrusion occurs. The deviation is prominent when $\delta\rho$ is small (see Fig. 6.15), because the growth rate during the process C is extremely slow and hence the acceleration of intrusion is thought to occur also slowly.

The decrease of q_2 and q_3 for large μ_H with increasing the pipe diameter can be also explained by the acceleration of intrusion. As estimated above, the parameters C_1 , C_2 , and C_3 decrease significantly as the pipe diameter increases if we assume that b_1 , b_2 and k are constants. Hence, it is expected that the growth rate of intrusion decreases as the pipe diameter increases, although b_1 , b_2 and k may depend somewhat on the pipe diameter. Nevertheless, it is found that q_2 and q_3 , which characterize the durations of the processes B and C, respectively, decrease as the pipe diameter increases. This is thought to be because the acceleration shortens the durations of the processes B and C. In addition, when the pipe length is short, it is found that the duration of the process C becomes shorter than that expected from the model (see Fig. 6.2). This is also considered to be due to the acceleration of intrusion.

Onset of rapid growth

It is shown in Sec. 6.1 that not only the duration of the process C but also the process B is shorter than that expected from the model when the pipe length is short. Although the detailed mechanism of the reduction of the duration of the process B is still unclear,

it is considered that the flow tends to lose its stability even by a slight intrusion when the pipe length is short, while the flow is relatively stable against a slight intrusion when the pipe length is long. Thus, more strict analysis of the flow stability is actually needed to describe the onset of the rapid growth precisely.

Continuous connection between up- and down-flows

In the actual system, the flow reversal proceeds in a continuous manner. However, it is assumed in the present model that the flow reversal occurs discontinuously when the intrusion reaches the end of a pipe. Although this assumption is approximately valid in most of the cases, it is no longer valid when the density difference $\delta\rho$ is extremely small, in which the flow reversal proceeds rather slowly (see Figs. 6.13 and 6.15). For the exact description of the flow-reversal process, it is clearly needed to improve the model so that the flow-reversal process is described in a continuous manner.

Interfacial tension

In the experiments shown in Chap. 4, mixtures of water, 1-propanol, and glycerin were used as the fluids, and their viscosities were varied by changing their compositions. However, when the composition of the fluid is varied, not only the viscosity but also the interfacial tension between the fluid and the glass pipe will vary. Thus, it is needed to exclude the possibility that the interfacial tension plays an essential role for the flow-reversal process other than the three factors considered in Sec. 5.1. However, I consider that the main factor causing the change in the flow-reversal process is the viscosity of the fluids, because similar results for s_d and s_u are obtainable irrespectively of the materials employed, as shown in Sec. 6.4. Thus, it seems that the effect of the interfacial tension between the fluid and the pipe is not essentially important, even if it exists. However, further investigations are needed to clarify the effect of the interfacial tension in detail.

Disturbance of interface

I have found that the obstruction of the growth of an intrusion due to a disturbance of the interface occurs when a high-viscosity fluid intrudes into the flow of low-viscosity fluid (Fig. 4.9). This phenomenon seems to be due to some kind of hydrodynamic instability at the interface. However, the detailed mechanism of the instability has not been clarified yet, and thus further study is needed from a hydrodynamic viewpoint.

Irregular oscillation and simultaneous up- and down-flow

It is found that an irregular oscillation occurs for large μ_H , when the pipe diameter is large. In addition, when a pipe is replaced by an orifice, simultaneous up- and down-flow inside the orifice has been found to occur also for large μ_H . Although the mechanisms of these phenomena have not been clarified yet, it is considered that in these cases the flow inside a pipe cannot exist stably for any height of the fluid surface because of the obstruction of the flow by an intrusion.

7.1.3 Extension to general cases

I have constructed the model under the assumption of $\beta\sigma^{1/2} \ll 1$, *i.e.*, the viscous damping regime (see Sec. 2.1), and $\epsilon = a/d \ll 1$. However, for the full understanding of the phenomenon, the nonlinear damping terms and the inertia terms in Eqs. (2.15), (2.16), (5.20), and (5.32) should be taken into account. Thus, the flow reversal from down- to up-flow is described by using Eqs. (2.16) and (5.20) in the following way:

$$\frac{d\hat{x}}{d\hat{t}} = \hat{z}, \quad (7.2)$$

$$\frac{\zeta\epsilon}{4D} \frac{d\hat{z}}{d\hat{t}} = -\hat{\mu}_H D \hat{z} + \frac{\zeta\epsilon\sigma}{8\phi} \hat{z}^2 - \phi D \tilde{x}, \quad (7.3)$$

$$\frac{d\hat{\xi}}{d\hat{t}} = \hat{\theta}, \quad (7.4)$$

$$C_4 \frac{d\hat{\theta}}{d\hat{t}} = -\epsilon \hat{\mu}_I \hat{\theta} + \frac{C_1 \hat{\mu}_I}{\phi} \hat{z} + C_2 (1 - \hat{x})(1 - e^{-\hat{\xi}/\alpha'}) + \frac{C_3 \phi e^{-\hat{\xi}/\gamma'}}{\hat{z}}. \quad (7.5)$$

In the same way, the flow reversal from up- to down-flow is derived from Eqs. (2.15) and (5.32) under the assumption of $(x_d - x_{de})/d \ll 1$ as follows:

$$\frac{d\hat{x}}{d\hat{t}} = \hat{z}, \quad (7.6)$$

$$\frac{\zeta\epsilon}{4D} \frac{d\hat{z}}{d\hat{t}} = -\hat{\mu}_L \hat{z} - \frac{\zeta\epsilon\sigma}{8\phi} \hat{z}^2 + \phi(1 - \psi \tilde{x}), \quad (7.7)$$

$$\frac{d\hat{\xi}}{d\hat{t}} = \hat{\theta}, \quad (7.8)$$

$$\frac{C_4}{D} \frac{d\hat{\theta}}{d\hat{t}} = -\epsilon \hat{\mu}_I \hat{\theta} + \frac{C_1 \hat{\mu}_I}{\phi} \hat{z} - C_2 \psi \tilde{x} (1 - e^{-(\epsilon^{-1} - \hat{\xi})/\alpha'}) - \frac{C_3 \phi e^{-(\epsilon^{-1} - \hat{\xi})/\gamma'}}{\hat{z}}. \quad (7.9)$$

Thus, Eqs. (7.2)-(7.9) are thought to be the generalized description of density oscillation. However, it should be noted that it is not yet clear whether these equations really reproduce the oscillatory behaviors correctly for any experimental condition. Thus, further investigation is clearly needed to clarify the validity of Eqs. (7.2)-(7.9).

7.2 Mechanism of relaxation oscillation

I have found that the flow-reversal process in a density oscillator is well described by a model in which three forces F_1 , F_2 and F_3 are considered. These three forces are regarded as ‘inhibiting factor’, ‘promoting factor’, and ‘triggering factor’ to characterize the growth of intrusion, respectively, because F_3 initiates the flow-reversal process and F_2 actually causes the flow reversal when it overwhelms F_1 that hinders the intrusion from growing.

The three factors are thought to be essential not only for the flow reversal in a density oscillator but also for any jumping process in relaxation oscillators generally found in nature. Namely, it is considered that the jumping process in a relaxation oscillator does not occur abruptly but a trigger of the jumping can be found before it occurs. A typical example is found in respiratory rhythms in mammals [14, 61]. The respiratory rhythm is known as a typical relaxation oscillation, and it has been long argued how the switching between the inspiration and expiration occurs. Although its mechanism has not been fully understood yet, it is known that lung inflation activates pulmonary stretch receptors (PSRs), and the afferent activity from the PSRs is carried to the brainstem by the vagus nerves, which ‘triggers’ the switching from inspiration to expiration [14, 61].

Thus, it is considered that the jumping process in relaxation oscillators occurs essentially in the same mechanism as the flow reversal in a density oscillator. Hence, the model of the density oscillator Eqs. (5.46)-(5.49) can be generalized so that various systems exhibiting relaxation oscillations will be universally described. The generalized equations are written using two variables X and Y as follows:

$$\dot{X} = -\frac{X}{\tau} \quad (7.10)$$

$$\epsilon \dot{Y} = -K_{\text{inh}}(Y; X) + K_{\text{pro}}(Y; X) + K_{\text{trig}}(Y; X) \quad (7.11)$$

for $\dot{X} < 0$ and

$$\dot{X} = \frac{1 - X}{\tau'} \quad (7.12)$$

$$\epsilon \dot{Y} = K'_{\text{inh}}(Y_{\text{th}} - Y; 1 - X) - K'_{\text{pro}}(Y_{\text{th}} - Y; 1 - X) - K'_{\text{trig}}(Y_{\text{th}} - Y; 1 - X) \quad (7.13)$$

for $\dot{X} > 0$, where X takes a value between 0 and 1, and the sign of \dot{X} changes when Y becomes 0 or Y_{th} . Exceptionally, Y remains 0 when the right hand side of Eq. (7.11) is negative, while Y remains Y_{th} when the right hand side of Eq. (7.13) is positive. τ and τ' denote the time constants in the relaxation processes, and ϵ is a parameter which satisfies $\epsilon \ll 1$. The functions $K_{\text{inh}}(Y; X)$, $K_{\text{pro}}(Y; X)$, $K_{\text{trig}}(Y; X)$, and their primes are the functions of Y , and takes positive values for $0 \leq Y \leq Y_{\text{th}}$. Here, X is regarded as a parameter characterizing the functional form of these functions, because X is a

slowly varying variable compared with Y with respect to time. The functional form of $K_{\text{inh}}(Y; X)$, $K_{\text{pro}}(Y; X)$, $K_{\text{trig}}(Y; X)$ have the following characteristics (see Fig. 7.1)¹:

1. $-K_{\text{inh}}(Y; X) + K_{\text{pro}}(Y; X)$ is a increasing function of Y .
2. $K_{\text{inh}}(Y; X)$ decreases while $K_{\text{pro}}(Y; X)$ increases as X is decreased.
3. $K_{\text{trig}}(Y; X)$ is a decreasing function of Y .
4. $K'_{\text{inh}}(Y; X)$, $K'_{\text{pro}}(Y; X)$, and $K'_{\text{trig}}(Y; X)$ have the same characteristics as $K_{\text{inh}}(Y; X)$, $K_{\text{pro}}(Y; X)$, and $K_{\text{trig}}(Y; X)$, respectively.

The dynamics of a system described by Eqs. (7.10)-(7.13) are explained in the following way. Now consider the case of $\dot{X} < 0$. When the value of X is large, Y remains zero because contribution of $K_{\text{inh}}(Y; X)$ is larger than those of $K_{\text{pro}}(Y; X)$ and $K_{\text{trig}}(Y; X)$ (see Fig. 7.1(a)). As X is decreased, Eq. (7.11) comes to have a positive stable solution owing to the contribution of $K_{\text{trig}}(Y; X)$ (Fig. 7.1(b)), and the solution increases gradually as X is decreased (Fig. 7.1(c)). With further decrease of X , the solution vanishes, and as a consequence Y increases rapidly (Fig. 7.1(d)). The case of $\dot{X} > 0$ can be considered in the similar way. In this way, the whole oscillatory behaviors of relaxation oscillators can be well described by using Eqs. (7.10)-(7.13).

Historically, many models of relaxation oscillators have been proposed [1, 8, 11, 15, 16, 22, 62]. However, some models lacked their essential mechanisms, although they roughly captured the oscillatory characteristics of relaxation oscillators. For instance, although the van der Pol equation is widely used for describing behaviors of relaxation oscillators [22], it did not give us an answer to the fundamental question of ‘‘How does the jumping process initiate?’’. Meanwhile, the other models lacked universality although they describe the detailed mechanisms of specific systems quite well. A typical example is Hodgkin-Huxley equation, which is a model of neural spiking [62]. Although it contained the detailed mechanisms of neural activities, it was quite complicated and cannot describe

¹In the case of density oscillator, these functions are given by replacing \hat{x} and $\hat{\xi}$ in Eqs. (5.46)-(5.49) with X and Y , respectively, as follows:

$$\begin{aligned}
K_{\text{inh}}(Y; X) &= \frac{C_1 X}{\mu_H} (= F'_1), \\
K_{\text{prom}}(Y; X) &= C_2(1 - X)(1 - e^{-Y/\alpha'}) (= F'_2), \\
K_{\text{trig}}(Y; X) &= \frac{C_3 \mu_H e^{-Y/\gamma'}}{\mu_I X} (= F'_3), \\
K'_{\text{inh}}(Y; X) &= \frac{C_1 X}{\mu_L}, \\
K'_{\text{prom}}(Y; X) &= C_2(1 - X)(1 - e^{-Y/\alpha'}), \\
K'_{\text{trig}}(Y; X) &= \frac{C_3 \mu_L e^{-Y/\gamma'}}{\mu_I X}.
\end{aligned}$$

Here, $\phi \approx \psi \approx 1$ has been assumed, for simplicity. Note that τ and τ' are given as $\tau = \mu_H$ and $\tau' = \mu_L$, respectively.

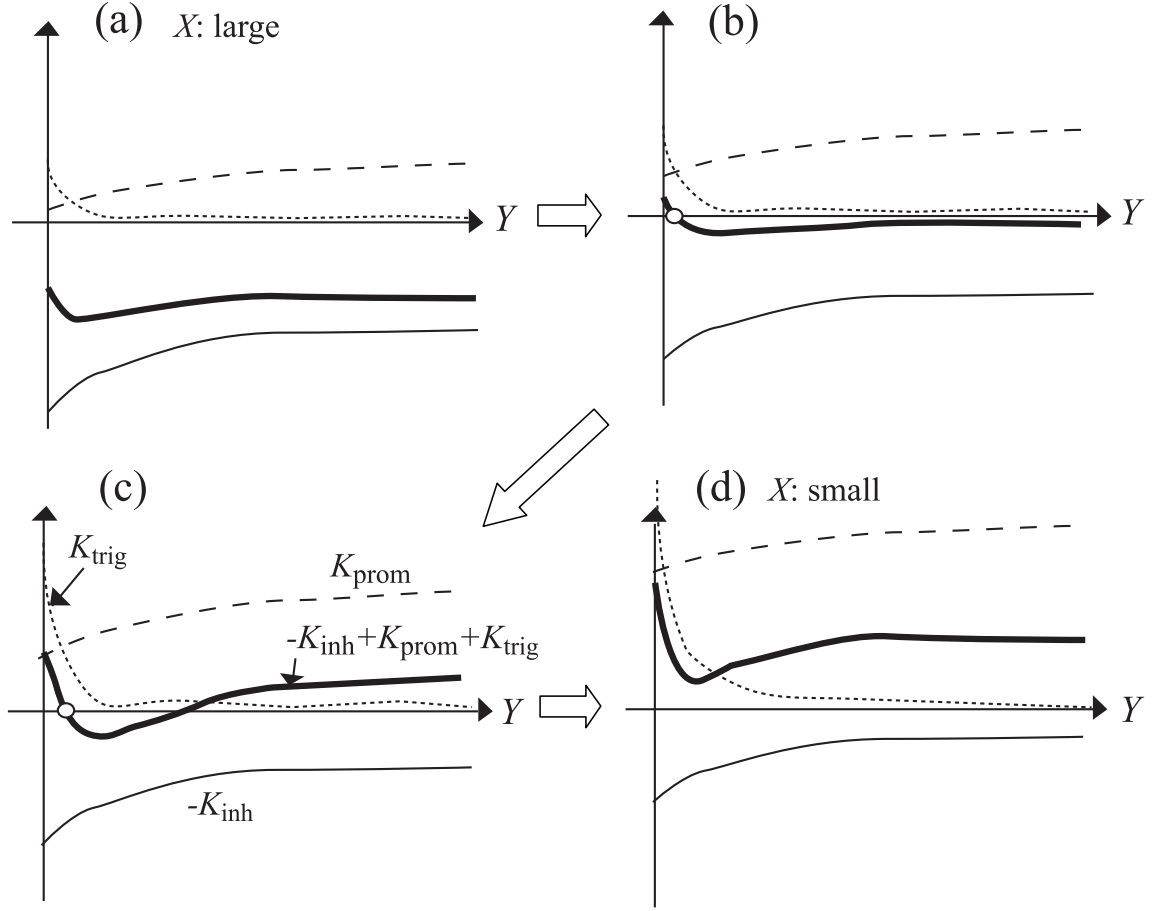


Figure 7.1: Scheme of the functional forms of $-K_{\text{inh}}(Y; X)$ (solid line), $K_{\text{pro}}(Y; X)$ (dashed line), $K_{\text{trig}}(Y; X)$ (dotted line), and $-K_{\text{inh}}(Y; X) + K_{\text{pro}}(Y; X)K + K_{\text{trig}}(Y; X)$ (bold line). The value of X is decreased as (a)→(b)→(c)→(d). Empty circles found in (b) and (c) are the stable solutions of Eq. (7.11).

the behaviors of relaxation oscillators other than those of neuronal systems. Therefore, a model of relaxation oscillators which describe their essential mechanisms universally has not been proposed up to now.

On the contrary, the present model (Eqs. (7.10)-(7.13)) not only contains the essential mechanism of oscillation but also describes the behaviors of relaxation oscillators universally. Hence, it is expected that the present model is applied to any system that exhibits relaxation oscillation, and makes it possible to understand its dynamics based on its essential mechanism.

7.3 Future prospect

In the present thesis, I have clarified the essence of relaxation oscillation by investigating the mechanism of density oscillation. Although systems exhibiting relaxation oscillations are diverse in nature and their detailed mechanisms are mostly complicated [1–6, 9, 11–14], their dynamics are thought to be simplified into a model described in Eqs. (7.10)-(7.13). This finding is extremely important, because we can understand macroscopic behaviors of relaxation oscillators from microscopic viewpoints. Indeed, the present study is expected to be developed further as follows.

One of the direction for the future study is its application to coupled oscillator systems. Although the generalized equations Eqs. (7.10)-(7.13) describe the behavior of a single relaxation oscillator, they can be extended to describe behaviors of coupled relaxation oscillators by adding coupling terms to them. Importantly, by using this model, we can understand how the essential mechanism of each oscillator relates to overall dynamics of coupled oscillators, whereas the detailed mechanism of each oscillator has been ignored for the description of coupled oscillators in the studies previously reported [2, 22, 25]. Thus, Eqs. (7.10)-(7.13) are expected to become the basis for the future theoretical studies of coupled relaxation oscillators. Indeed, using this model, the dynamics of various types of coupled oscillators such as the cases where time-delay exists at the coupling, where the coupling strength between oscillators depend on their spatial distributions, and where the properties of oscillators differ from each other, will be investigated.

Another possibility for the future application is the control of relaxation oscillation. Recently, controlling the dynamics of relaxation oscillation has attracted particular attention. A typical example is the bright light therapy to the patients with sleep disorders. It is well known that the sleep-wake cycles exhibit relaxation oscillations [63]. The sleep-wake rhythm can be modulated by light, and thus it usually synchronizes with the periodic day and night cycles. However, in the patients with sleep disorders, the synchronization does not occur or their phases are shifted for some reason. Hence, as the

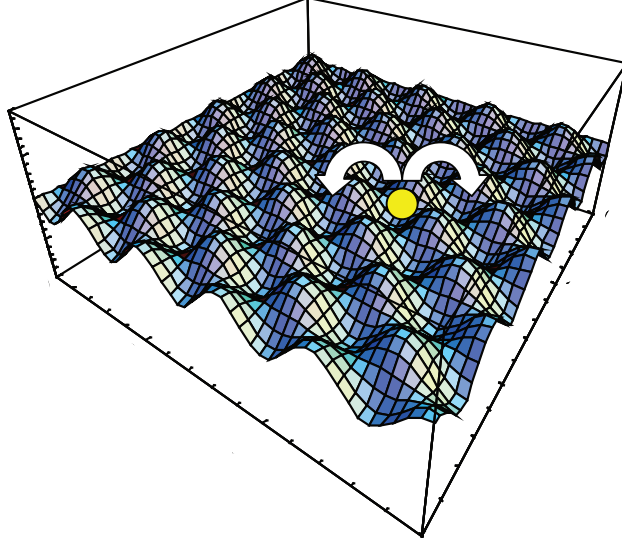


Figure 7.2: Schematic image of “attractor crowding”. The basin of attraction becomes crowded in the phase space and hence even small noise causes the system to hop freely among many coexisting stable attractors.

treatment of the sleep disorders, scheduled exposure to bright light has been often used to control the sleep-wake rhythms [64]. For the development of such control techniques, Eqs. (7.10)-(7.13) are considered to become a useful model, because both the essential cause of the disorder and the effect of the bright light can be taken into it, which will lead us to predict the dynamics under the control by a simulation.

In this way, Eqs. (7.10)-(7.13) are expected to be used as an excellent model describing the dynamics of relaxation oscillation. While the theoretical studies based on Eqs. (7.10)-(7.13) are thought to be important, it is also important to verify the validity of the theoretical expectation experimentally. For this purpose, density oscillator is thought to be an excellent experimental system. In the following, I will show some examples of the possible usage of the density oscillators for the studies on the coupled oscillators and the control techniques.

Firstly, coupled density oscillators will be used for the investigation of the robustness of splay state [56, 57, 65, 66]. The splay state is a state where the phases of oscillators differ from each other equidistantly, and hence the existence of a single splay state necessarily implies the coexistence of $(N - 1)!$ symmetry-related states. The multiplicity of the splay states has raised the possibility that they can be used as storage elements in a dynamic, rewritable memory [57, 66]. However, it has not been actually realized, because with increasing N the basin of attraction becomes crowded in the phase space and hence even small noise causes the system to hop freely among many coexisting stable attractors

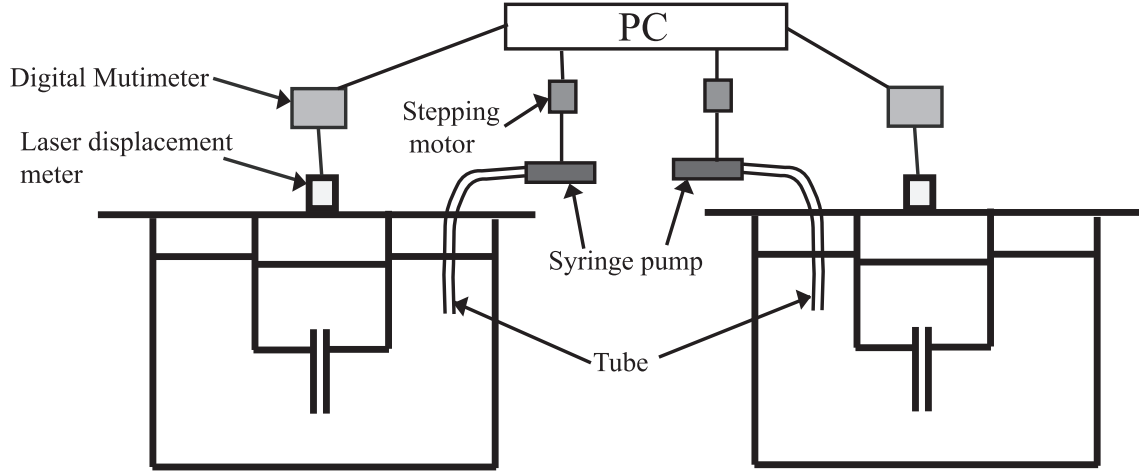


Figure 7.3: Scheme of density oscillators coupled to each other by tubes. The height of the heavy fluid surface is measured by a laser displacement meter, and recorded by a digital multimeter for each oscillator. The data obtained from oscillators are analyzed by a computer, which regulates stepping motors based on a finite algorithm. A syringe pump located at each oscillator is driven by the stepping motor, and then the light fluid in the outer container is added or reduced. Although the present figure shows the case where the number of oscillators is two, more than two oscillators can be coupled in the same way.

(Fig. 7.2) [65]. This phenomenon is called ‘attractor crowding’. Hence, we need to investigate how we can achieve a stable splay state robust to noise. For this purpose, density oscillators are thought to be a useful experimental system because they are known to exhibit the splay state when several oscillators are coupled to each other [33,36–39,45].

Secondly, coupled density oscillators will be used for the investigation of time-delayed feedback. Time-delayed feedback is a method that some proportion of the output signal of a system is fed back to the input with time-delay [28, 67, 68]. This method has been studied as an excellent scheme for the control of systems, and is known to be also applied to coupled relaxation oscillators. In fact, interaction between oscillators can be regulated arbitrarily using this method [28], and it is suggested that the method may be applied to the desynchronization of synchronized neurons which cause tremors in patients suffering from Parkinson’s disease or essential tremor [29]. For further development of the time-delayed feedback scheme, the density oscillators will be used as an excellent experimental system. Although the time-delayed coupling cannot be introduced if several inner containers are held within one outer container (Fig. 1.7), it will be possible if the oscillators are coupled to each other by tubes through which the light fluid is added or reduced, whose amount is determined by the height of the heavy fluid surface of the other inner containers (Fig. 7.3).

In this way, the dynamics of relaxation oscillators are expected to be clarified in the fu-

ture not only theoretically by the model based on their essential mechanisms (Eqs. (7.10)-(7.13)), but also experimentally by using density oscillators. Hence, further theoretical and experimental studies on the relaxation oscillation are clearly needed.

Appendix A

Hagen-Poiseuille flow

Hagen-Poiseuille flow is the steady flow of a incompressible fluid through a straight pipe of circular cross section with rotational symmetry [55]. Now consider a long pipe whose radius is a . Let z axis be selected along the axis of the pipe, and r denote the radial coordinate measured from the axis outwards. The flow is assumed to be parallel along the pipe, and thus the velocity components in the tangential and radial directions are assumed to be zero. The z component of the velocity is denoted by u .

Then, from the condition of continuity, we can easily obtain $\partial u / \partial z = 0$. Thus, u does not depend on z and is described as $u = u(r)$. On the other hand, we find that the hydrostatic pressure P does not depend on r and is described as $P = P(z)$, which is obtained from the radial and tangential components of the Navier-Stokes equation. Hence, the z component of the Navier-Stokes equations in cylindrical coordinates becomes

$$\mu \left(\frac{\partial^2 u}{\partial r^2} + \frac{1}{r} \frac{\partial u}{\partial r} \right) = \frac{\partial P}{\partial z}, \quad (\text{A.1})$$

where μ is the viscosity of the fluid. The boundary condition is given as $u = 0$ for $r = a$ (no-slip condition). By solving Eq. (A.1) with this boundary condition, it is found that

$$u(r) = -\frac{1}{4\mu} \frac{dP(z)}{dz} (a^2 - r^2), \quad (\text{A.2})$$

where $dP(z)/dz$ should be a constant, because $u(r)$ does not depend on z . The mean velocity \bar{u} is given as

$$\bar{u} = \frac{2}{a^2} \int_0^a u(r) r dr = -\frac{a^2}{8\mu} \frac{dP(z)}{dz}. \quad (\text{A.3})$$

From Eqs. (A.2) and (A.3), the following relation is obtained

$$\left. \frac{\partial u}{\partial r} \right|_{r=a} = -\frac{4\bar{u}}{a}. \quad (\text{A.4})$$

Two-dimensional Poiseuille flow

The steady flow between two parallel flat walls, which is known as two-dimensional Poiseuille flow, is considered in the same way. Now let y and z axis be selected vertical and parallel to the flat walls, respectively. The flat walls are assumed to be located at $y = 0, 2a$. When we assume that the flow is parallel to the flat walls, y component of the velocity becomes zero. Here let w be defined as the z component of the velocity.

From the condition of continuity, we obtain $\partial w / \partial z = 0$. Thus w is described as $w = w(y)$. From the z component of the Navier-Stokes equations, it is found that the hydrostatic pressure gradient P does not depend on y , and thus P is written as $P = P(z)$. Hence, z component of the Navier-Stokes equations becomes

$$\mu \frac{\partial^2 w}{\partial y^2} = \frac{dP(z)}{dz}. \quad (\text{A.5})$$

The boundary condition is given as $w = 0$ for $y = 0, 2a$ (no-slip condition). By solving Eq. (A.5) with this boundary condition, $w(y)$ is obtained as

$$w(y) = -\frac{1}{2\mu} \frac{dP(z)}{dz} [a^2 - (y - a)^2], \quad (\text{A.6})$$

where $dP(z)/dz$ should be a constant, because $w(y)$ does not depend on z . Thus, the flow rate Q is derived as

$$Q = \int_0^{2a} dy w(y) = -\frac{2a^3}{3\mu} \frac{dP(z)}{dz}. \quad (\text{A.7})$$

Appendix B

Complementary explanation for phenomenological model

Although an oscillatory behavior cannot be introduced by Eq. (2.28), Eq. (2.29) reproduces the behavior of relaxation oscillation phenomenologically. This fact can be understood in the following way [15]. Let Eqs. (2.28) and (2.29) be rewritten as

$$\frac{d\hat{x}'}{d\hat{t}} = \hat{y}' \quad (\text{B.1})$$

$$\frac{d\hat{y}'}{d\hat{t}} = -A_1\hat{y}'|\hat{y}'| - A_2\hat{y}' - A_3(1+R)\hat{x}' + \frac{A_3}{2}\text{sgn}(\hat{y}'). \quad (\text{B.2})$$

and

$$\frac{d\hat{x}'}{d\hat{t}} = \hat{y}' \quad (\text{B.3})$$

$$\frac{d\hat{y}'}{d\hat{t}} = B_1\hat{y}' - B_2\hat{y}'^3 - A'_3\hat{x}'. \quad (\text{B.4})$$

Here, notice that \hat{y}' is generally a fast variable compared with \hat{x}' because A_1 , A_2 , and A_3 are usually much larger than unity. Then, vector fields can be drawn in $\hat{y}' - \hat{x}'$ plane. Figure B.1 shows the examples. In the case of Eqs. (B.1) and (B.2), the system approaches to the equilibrium points $(\hat{y}', \hat{x}') = (0, \pm 1/[2(1+R)])$ in the phase plane and thus oscillatory behavior is not described. On the other hand, in the system described by Eqs. (B.3) and (B.4), limit-cycle oscillation occurs in the following way: \hat{x}' increases slowly along the curve of the steady solution of Eq. (B.4), $A'_3\hat{x}' = B_1\hat{y}' - B_2\hat{y}'^3$. At a threshold, the value of \hat{y}' jumps to the lower value, and \hat{x}' decrease slowly along the curve of $A'_3\hat{x}' = B_1\hat{y}' - B_2\hat{y}'^3$. Then, at the other threshold, the value of \hat{y}' jumps to the higher value, and \hat{x}' increases slowly along the curve again. In this way, the reason that Eq. (2.29) exhibits relaxation oscillation can be well understood.

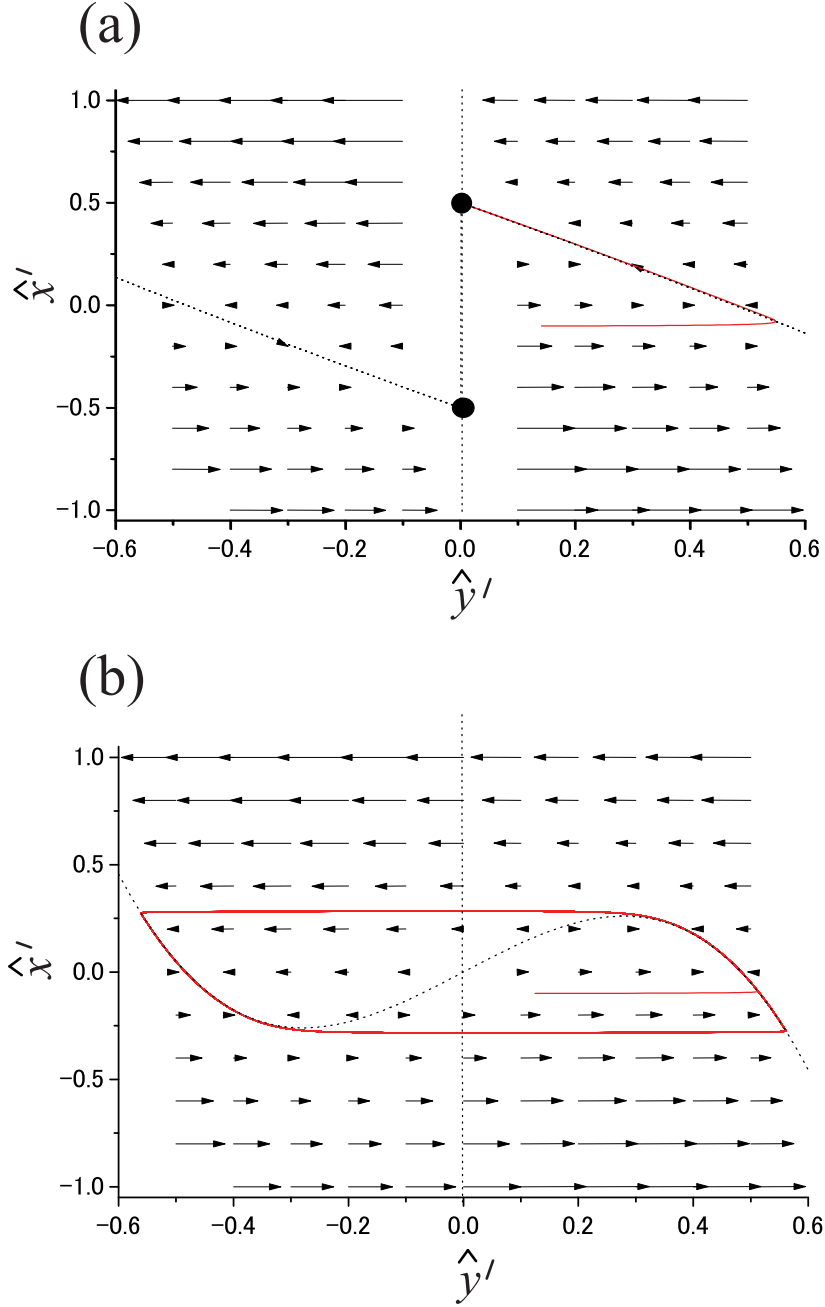


Figure B.1: Vector fields described by (a) Eqs. (B.1) and (B.2), and (b) Eqs. (B.3) and (B.4). The trajectories with the initial condition of $\hat{y}' = 0.1$ and $\hat{x}' = -0.1$ are also shown (red lines). Dotted lines denote the steady solutions of (a) Eqs. (B.1) and (B.2), and (b) Eqs. (B.3) and (B.4). While any initial condition is attracted to $(\hat{y}', \hat{x}') = (0, \pm 1/[2(1 + R)])$ (black circles) in the case of (a), the trajectory draws a limit cycle in the case of (b). The values of the parameters are as follows: $A_1 = 10$, $A_2 = 100$, $A_3 = 100$, $B_1 = 140$, $B_2 = 600$, $R = 0$.

Appendix C

Model of coupled density oscillators

A model describing coupled oscillators is derived by modifying Eq. (2.29). Although the formulations of the model slightly differed depending on the studies and their derivations were not described in detail [32–34], here the representative one with its derivation is shown.

Now consider the case of N coupled oscillators, and each oscillator is assumed to be nearly identical. Then, because the height of the light fluid surface h is determined by those of the heavy fluid surfaces in the inner containers, Eq. (2.6) is rewritten in the following way:

$$h - h_{\text{de}}^{(i)} = -R \sum_{j=1}^N (x_j^{(i)} - x_{\text{de}}^{(i)}), \quad j = 1, 2, \dots, N. \quad (\text{C.1})$$

By using Eq. (C.1) instead of Eq. (2.6), Eqs. (2.8) and Eqs. (2.9) should be changed to

$$\frac{S}{a^2\pi} \ddot{x}_k + \frac{3S^2}{4da^4\pi^2} \dot{x}_k^2 + \frac{8\nu_{\text{L}}S}{a^4\pi} \dot{x}_k + \frac{g}{d} \frac{\rho_{\text{H}}(t)}{\rho_{\text{L}}} x_k + \frac{g}{d} R \sum_{j=1}^N x_j = \frac{g}{d} (h_{\text{de}}^{(i)} + RNx_{\text{de}}^{(i)}) + \frac{\rho_{\text{H}}(t) - \rho_{\text{L}}}{\rho_{\text{L}}} g, \quad (\text{C.2})$$

$$\frac{S}{a^2\pi} \ddot{x}_k - \frac{3S^2}{4da^4\pi^2} \dot{x}_k^2 + \frac{8\nu_{\text{H}}(t)S}{a^4\pi} \dot{x}_k + \frac{g}{d} x_k + \frac{\rho_{\text{L}}}{\rho_{\text{H}}(t)} \frac{g}{d} R \sum_{j=1}^N x_j = \frac{\rho_{\text{L}}}{\rho_{\text{H}}(t)} \frac{g}{d} (h_{\text{de}}^{(i)} + RNx_{\text{de}}^{(i)}), \quad (\text{C.3})$$

where k is an oscillator number. In the non-dimensionalized forms, the following equations instead of Eqs. (2.15) and Eqs. (2.16) are obtained:

$$\frac{d^2 \hat{x}_k^{(i)}}{d\hat{t}^2} + \frac{2\sigma^{1/2}}{\beta} \left[\frac{d\hat{x}_k^{(i)}}{d\hat{t}} + \frac{\beta\sigma^{1/2}}{4} \left(\frac{d\hat{x}_k^{(i)}}{d\hat{t}} \right)^2 \right] + \sigma(\hat{x}_k - 1) + \sigma R \sum_{j=1}^N \hat{x}_j = 0, \quad (\text{C.4})$$

for up-flow and

$$\frac{d^2 \hat{x}_k^{(i)}}{d\hat{t}^2} + \frac{2\sigma^{1/2}}{\beta} \left[\frac{\nu_{\text{H}}^{(i)}}{\nu_{\text{L}}} \frac{d\hat{x}_k^{(i)}}{d\hat{t}} - \frac{\beta\sigma^{1/2}}{4} \left(\frac{d\hat{x}_k^{(i)}}{d\hat{t}} \right)^2 \right] + \sigma\hat{x}_k + \sigma DR \sum_{j=1}^N \hat{x}_j = 0, \quad (\text{C.5})$$

for down-flow.

Hence, by assuming that $D \approx 1$ and $\hat{\nu}_H = \hat{\nu}_L = \hat{\nu}$, and that $\rho_H^{(i)}$ and $\hat{x}^{(i)}$ do not depend on the number of cycles i , the following equation is obtained in the same way as Eq. (2.29):

$$\frac{d^2 \hat{x}'_k}{d\hat{t}^2} = B_1 \left(\frac{d\hat{x}'_k}{d\hat{t}} \right) - B_2 \left(\frac{d\hat{x}'_k}{d\hat{t}} \right)^3 - A_3 \hat{x}'_k - A_3 R \sum_{j=1}^N \hat{x}'_j. \quad (\text{C.6})$$

Here, \hat{x}'_k is defined as $\hat{x}'_k = \hat{x}_k - 1/2$. The last term in the right hand of Eq. (C.6) is originated from the change of the light fluid surface, through which the oscillators are coupled to each other.

Bibliography

- [1] P. S. Landa, *Nonlinear Oscillations and Waves in Dynamical Systems* (Kluwer Academic Publishers, Dordrecht, 1996).
- [2] A. Pikovsky, M. Rosenblum, and J. Kurths, *Synchronization: A Universal Concept in Nonlinear Sciences* (Cambridge University Press, Cambridge, 2001).
- [3] D. DiFrancesco, Ann. Rev. Physiol. **55**, 455 (1993).
- [4] K. Stern and M. K. McClintock, Nature, **392**, 177 (1998).
- [5] A. Takamatsu, R. Tanaka, H. Yamada, T. Nakagaki, T. Fujii, and I. Endo, Phys. Rev. Lett. **87**, 078102 (2001).
- [6] R. J. Field and R. M. Noyes, J. Chem. Phys. **60**, 1877 (1974).
- [7] J. Miyazaki, *Theoretical and Experimental Study on Coupled Oscillators by using Belousov-Zhabotinsky Reaction*, (Ph. D. thesis, 2006).
- [8] A. Timmermann, H. U. Voss, and R. Pasmanter, Am. Meteo. Soc. **31**, 1579 (2001).
- [9] M. V. L. Bennett and R. S. Zukin, Neuron **41**, 495 (2004).
- [10] K. Wiesenfeld, P. Colet, and S. H. Strogatz, Phys. Rev. E **57**, 1563 (1998).
- [11] B. Blasius, F. Beck, and U. Lüttge, J. Theor. Biol. **184**, 345 (1997).
- [12] M. C. Lagomarsino, P. Jona, and B. Bassetti, Phys. Rev. E **68**, 021908 (2003).
- [13] L. O. Chua, C. A. Desoer and E. S. Kuh, *Linear and Nonlinear Circuits* (McGraw-Hill, New York, 1987).
- [14] S. M. Botros and E. N. Bruce, Biol. Cybern. **63**, 143 (1990).
- [15] A. A. Andronov and C. C. Chaikin, *Theory of oscillations* (Princeton Univ. Press, Princeton, New Jersey, 1949); A. A. Andronov, A. A. Vitt and S. E. Khaikin, *Theory of oscillators* (Pergamon Press, Oxford, London, Edinburgh, New York, Toronto, Paris, Frankfurt, 1966).
- [16] N. Minorsky, *Nonlinear Oscillations* (Robert E.Krieger Publishing Compony, Huntington, NY, 1974).
- [17] Lord Rayleigh (J. W. Strutt), *The theory of sound* (Dover Publishers, New York, 1945).
- [18] B. van der Pol, Radio Rev. **1**, 701 (1920).
- [19] B. van der Pol, Phil. Mag. S. 7, **2**, 978 (1926).
- [20] B. van der Pol and J. van der Mark, Nature, **120** 363 (1927).

- [21] B. van der Pol, *Phil. Mag. S. 7*, **3**, 65 (1927).
- [22] B. van der Pol and J. van der Mark, *Phil. Mag. S. 7*, **6**, 763 (1928).
- [23] H. Poincare, *Lés méthodes nouvelles de la mécanique céleste*, Kris, Gauthier-villars (1892-1899).
- [24] S. C. Manrubia, A. S. Mikhailov, and D. H. Zanette, *Emergence of Dynamical order: Synchronization Phenomena in Complex Systems* (World Scientific, Singapore, 2004).
- [25] Y. Kuramoto, *Chemical Oscillations, Waves, and Turbulence* (Springer-Verlag, Berlin, 1984).
- [26] E. Kaempfer, *The History of Japan (With a Description of the Kingdom of Siam)*. Sloane, London, 1727. Posthumous translation; or reprint by McLehose, Glasgow, 1906.
- [27] E. Klavins and D. E. Koditschek, *Int. J. Rob. Res.* **21**, 257 (2002).
- [28] I. Kiss, C. G. Rusin, H. Kori, J. L. Hudson, *Science* **316**, 1886 (2007).
- [29] P. A. Tass, *Phase Resetting in Medicine and Biology: Stochastic Modelling and Data Analysis* (Springer Verlag Berlin, 1999).
- [30] Y. W. Hong and A. Scaglione, *IEEE J. Sel. Area. Comm.* **23**, 1085 (2005).
- [31] S. Martin, *Geophys. Fluid Dyn.* **1**, 143 (1970).
- [32] K. Yoshikawa and H. Kawakami, *Oyo Suri* **4**, 238 (1994) (in Japanese).
- [33] K. Yoshikawa and K. Fukunaga, *Chem. Phys. Lett.* **174**, 203 (1990).
- [34] K. Yoshikawa, S. Maeda, and H. Kawakami, *Ferroelectrics* **86**, 281 (1988).
- [35] M. Okamura and K. Yoshikawa, *Phys. Rev. E* **61**, 2445 (2000).
- [36] S. Nakata, T. Miyata, N. Ojima, and K. Yoshikawa, *Physica D* **115**, 313 (1998).
- [37] K. Miyakawa and K. Yamada, *Physica D* **151**, 217 (2001).
- [38] K. Miyakawa and K. Yamada, *Physica D* **127**, 177 (1999).
- [39] K. Yoshikawa, N. Oyama, M. Shoji, and S. Nakata, *Am. J. Phys.* **59**, 137 (1991).
- [40] O. Steinbock, A. Lange, and I. Rehberg, *Phys. Rev. Lett.* **81**, 798 (1998).
- [41] M. Ueno, F. Uehara, Y. Narahara, and Y. Watanabe, *Jp. J. Appl. Phys.* **45**, 8928 (2006).
- [42] K. Aoki, *Physica D* **147**, 187 (2000).
- [43] P. H. Alfredsson and T. Lagerstedt, *Phys. Fluids* **24**, 10 (1981).
- [44] R. M. Noyes, *J. Chem. Edu.* **66**, 207 (1989)
- [45] K. Yoshikawa and S. Nakata, *React. Kinet. Catal. Lett.* **42**, 333 (1990).
- [46] A. K. Das and R. C. Srivastava, *J. Chem. Soc. Faraday Trans.* **89**, 905 (1993).
- [47] R. C. Srivastava, *Pure & Appl. Chem.* **66**, 455 (1994).
- [48] R. C. Srivastava, V. Agarwala, A. K. Das and S. Upadhyay, *Indian J. Chem*, **33A**, 978 (1994).
- [49] L. Adamciková, *React. Kinet. Catal. Lett.* **48**, 649 (1992).

- [50] S. Upadhyay, A. K. Das, V. Agarwala, and R. C. Srivastava, *Langmuir* **8**, 2567 (1992).
- [51] R. P. Rastogi, R. C. Srivastava and S. Kumar, *J. Col. Inter. Sci.* **283**, 139 (2005).
- [52] R. Cervellati and R. Solda, *Am. J. Phys.* **69**, 543 (2001).
- [53] K. Yoshikawa, S. Nakata, M. Yamakata and T. Waki, *J. Chem. Edu.* **66**, 205 (1989).
- [54] J. A. M. Villarreyes, H. J. B. da Costa, F. Kokubun, L. C. Schmitz, and J. A. Castro, *Comp. Chem. Eng.* **24**, 1753 (2000).
- [55] H. Schlichting, *Boundary Layer Theory* (McGraw-Hill, 1960).
- [56] M. Silber, L. Fabiny, and K. Wiesenfeld, *J. Opt. Soc. Am. B* **10**, 1121 (1993).
- [57] S. Nichols and K. Wiesenfeld, *Phys. Rev. A* **45**, 8430 (1992).
- [58] G. I. Taylor, *Proc. R. Soc. London Ser. A* **201**, 192 (1950).
- [59] P. G. Saffman and G. I. Taylor, *Proc. R. Soc. London Ser. A* **245**, 312 (1958).
- [60] R. Menikoff, R. C. Mjosness, D. H. Sharp, and C. Zemach, *Phys. Fluids* **20**, 2000 (1977).
- [61] F. Hayashi, S. K. Coles, and D. R. McCrimmon, *J. Neuroscience*, **16**, 6526 (1996).
- [62] A. Hodgkin and A. Huxley, *J. Physiol.* **117**, 500 (1952).
- [63] C. G. D. Behn, E. N. Brown, T. E. Scammell and N. J. Koppell, *J. Neurophysiol.* **97**, 3828 (2007).
- [64] D. J. Dijk, Z. Boulos, C. I. Eastman, A. J. Lewy, S. S. Campbell, and M. Terman, **10**, 113 (1995).
- [65] K. Wiesenfeld and P. Hadley, *Phys. Rev. Lett.* **62** 1335 (1989).
- [66] K. Otsuka, *Phys. Rev. Lett.* **67**, 1090 (1991).
- [67] A. S. Mikhailov and K. Schowalter, *Phys. Reports* **425**, 79 (2006).
- [68] M. Rosenblum and A. Pikovsky, *Phys. Rev. E* **70**, 041904 (2004); M. Rosenblum and A. Pikovsky, *Phys. Rev. Lett.* **92**, 114102 (2004).

Acknowledgements

I would like to express my sincere appreciation to Professor Shuichi Kinoshita of Osaka University (Graduate school of Frontier biosciences) for his offer of worthwhile research environment and thoughtful advices throughout the course of this work. I wish to thank to Dr. Junji Watanabe of Osaka University (Graduate school of Frontier biosciences) for his pointed advices. I would like to thank to Dr. Shinya Yoshioka of Osaka University (Graduate school of Frontier biosciences) for his valuable suggestions. I am grateful to Dr. Jun Miyazaki (Graduate school of Frontier biosciences) for his helpful discussions. My thanks are also due to a number of my colleagues in Kinoshita laboratory.

Finally, I also renders thanks to Dr. Chihiro Hamaguchi and my parents who gave me an opportunity to change my career from a physician to a physicist.

List of publications and Presentations

Original Papers

1. T. Kano and S. Kinoshita
“Viscosity-dependent flow reversal in a density oscillator”, Phys. Rev. E, **76**, 046208 (2007).
2. T. Kano and S. Kinoshita
“Modeling of flow-reversal process in a density oscillator”, J. Korean Phys. Soc., submitted.

International Conference

1. T. Kano
“Flow reversal in a density oscillator”, 9th Tamura Symposium “Frontiers in Dynamics: Physical and Biological Systems”, Tokyo, Japan, (May 22-24, 2006).
2. T. Kano and S. Kinoshita
“Flow instability in density oscillator”, Gordon Research Conferences “Oscillations & Dynamic Instabilities in Chemical Systems”, Oxford, UK, (July 30-August 4, 2006).
3. T. Kano and S. Kinoshita
“Modeling of dynamical behaviors in a density oscillator”, Gordon Research Conferences “Nonlinear Science”, Waterville, USA, (June 23-29, 2007).
4. T. Kano and S. Kinoshita
“Modeling of flow-reversal process in a density oscillator”, The 10 th Asia Pacific Physics Conference, Pohang, Korea (Aug. 21-24, 2007).